
E S A
1896

Chapter 1: Overview

1.1 General Introduction

An atom is about 1 Å, or 10^{-10} meters. The study of atoms and molecules is in the conventional field of chemistry as was studied in the late 19th and 20th centuries. A nanometer (nm), or 10^{-9} meters, represent a collection of a few atoms or molecules. Properties of bulk substances of micrometer sizes or larger have been studied for years by solid state physicists and material scientists and are currently well understood. Materials on the 1–100 nm scale were not studied by either group in the past. It was just recently shown that on this size scale the properties of a material become dependent on its size and shape. Thus, the nanometer scale incorporates collections of atoms or molecules, whose properties are neither those of the individual constituents nor those of the bulk. On this scale, many of the atoms are still located on the surface, or one layer removed from the surface, as opposed to the interior. New properties are observed on this scale because the interface that is not observed in the bulk or individual atoms. Since the properties depend on the size of the structure, instead of the nature of the material, reliable and continual change can be achieved using a single material.[1,2]

The topic of "nano" was touched upon by "*There's Plenty of Room at the Bottom*" a talk given by physicist Richard Feynman at an American Physical Society meeting at Caltech on December 29, 1959. Over 50 years ago, Feynman imagined a new physical world of ultra-small volumes and highlighted some difficulties that researchers might encounter when visiting it. His talk provided a vision for engineers and scientists to establish a new field, which-with subsequent developments in novel equipment and manufacturing skills-is known as "nanotechnology".

Nanotechnology has become one of the most important and exciting forefront field in physics, chemistry, engineering, and biology which the characteristic dimensions are below ca. 100 nm.[3,4,5] It shows great promise for providing us in the near future with many breakthroughs that will change the direction of technological advances in a wide range of applications. With nanotechnology, a large set of materials and improved products rely on a change in the physical properties when the feature sizes are shrunk. The major publications in this area have appeared in the *Journal of Physical Chemistry B*, *Journal of the American Chemical Society* (*JACS*) and *Langmuir*. *Nano Letters*, *Nature Nanotechnology* and *ACS nano* have also published a large number of letters in this field since its conception in 2001, 2006 and 2007, respectively. The number of patent applications and symposium articles for the Materials Research Society (MRS), the American Chemical Society (ACS), the Royal Society Chemistry (RSC), and Advanced Materials (Wiley Publications) also represent a large number of the publications every year on noble nanomaterials.

1.2 Nanobiotechnology

Three main disciplines, in Figure 1.1, including chemistry, materials science and biotechnology are presented.[6] Merging these subjects will allow us to take advantage of the improved evolutionary biological components to generate new smart materials and to apply today's advanced materials and physicochemical techniques to solve biological problems.[1,2] Both biotechnology and materials science meet at the same length scale (See Figure 1.2). On the one hand, biomolecular components have typical size dimensions in the range of about 5 to 200 nm. On the other hand, commercial requirements to produce increasingly miniaturized microelectronic devices strongly motivate the elaboration of nanoscale systems. Today's nanotechnology research puts

a great emphasis on the development of bottom-up strategies, which concern the self-assembly of (macro) molecular and colloidal building blocks to create larger, functional devices.[7]

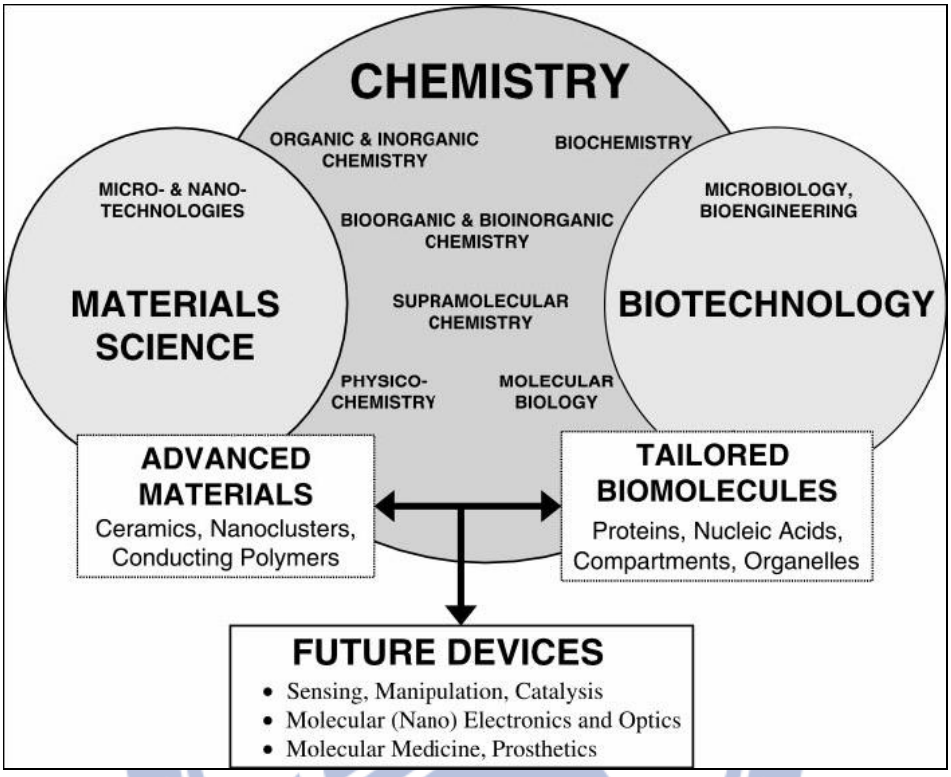

Figure 1.1 Chemistry is the central science for the development of applied disciplines such as materials research and biotechnology. Materials science, which is based on classic chemical research fields and engineering technologies, has led to enormous advances in tailoring advanced modern materials.[6]

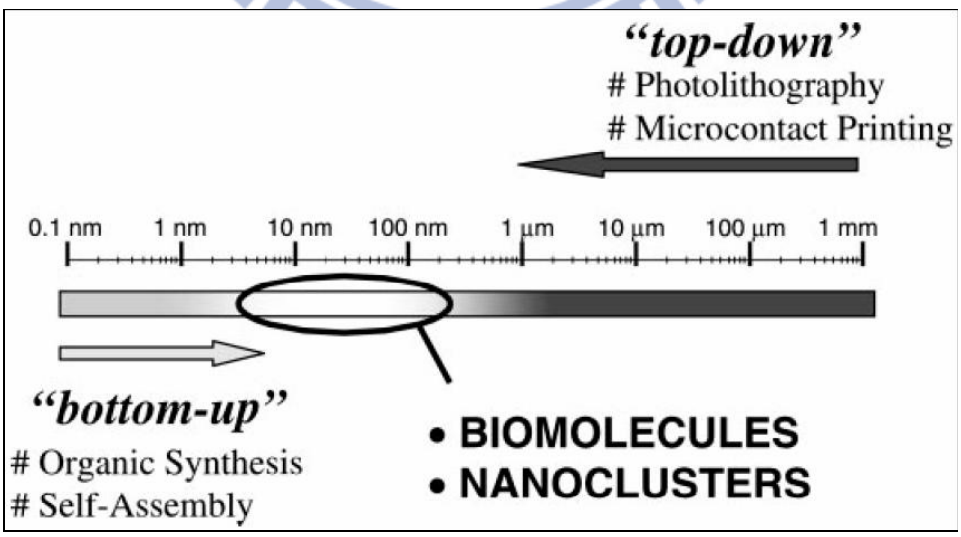

Figure 1.2 A gap currently exists in the engineering of small-scale devices. Whereas conventional top-down processes hardly allow the production of structures smaller than about 100–200 nm, the limits of regular bottom-up processes are in the range of about 2–5 nm.[6]

The convergence of biotechnology and nanotechnology has led to the development of hybrid nanomaterials that incorporate the highly selective catalytic and recognition properties of biomaterials, such as proteins/enzymes and DNA, with the unique electronic, photonic, and catalytic features. Novel nanomaterials for use in bioassay applications represent a rapidly advancing field. Various nanostructures have been investigated to determine their properties and possible applications in biotechnology. These structures include nanoparticles (NPs), nanowires, nanotubes, and thin films. Functional NPs (electronic, optical and magnetic) bound to biological molecules have been developed for use in biosensors to detect and amplify various signals.[8,9,10] The interdisciplinary cooperation of various techniques can solve the human-related diseases. The conjugation of NPs and other nanoobjects (e.g. nanorods and carbon nanotubes) with biomolecules is an attractive area of research within nanobiotechnology.[11,12,13,14] Biomolecules are fascinating macromolecular structures in terms of their unique recognition, transport, and catalytic properties. The conjugation of nanomaterials with biomolecules could provide electronic or optical transduction of biological phenomena in the development of novel biosensors.[15] Enzymes, antigens and antibodies, and biomolecular receptors have dimensions in the range of 2–20 nm, similar to those of nanostructures, thus the two classes of materials are structurally compatible.

The size of nanomaterials can be an advantage over a bulk structure, simply because a target binding event involving the nanomaterials can have a significant effect on its physical and chemical properties. In this regard, the use of nanomaterials in biology has a long history as nanoparticles have been used in bioconjugation and as cellular labeling agents for the past four decades. However, new synthesis, fabrication, and characterization methods for nanomaterials have evolved to the point that deliberate modulation of their size, shape, and composition is possible (See Figure

1.3), thereby allowing exquisite control of their properties.[1] Additionally, tools and techniques for surface modification and patterning have advanced to a point that now allows generation of nanoscale arrays of biomacromolecules and small molecules on surfaces.[16,17,18] Along with synthetic advances for varying the size, shape, and composition of nanostructured materials has come the ability to tailor their binding affinities for various biomolecules through surface modification and engineering.[19,20]

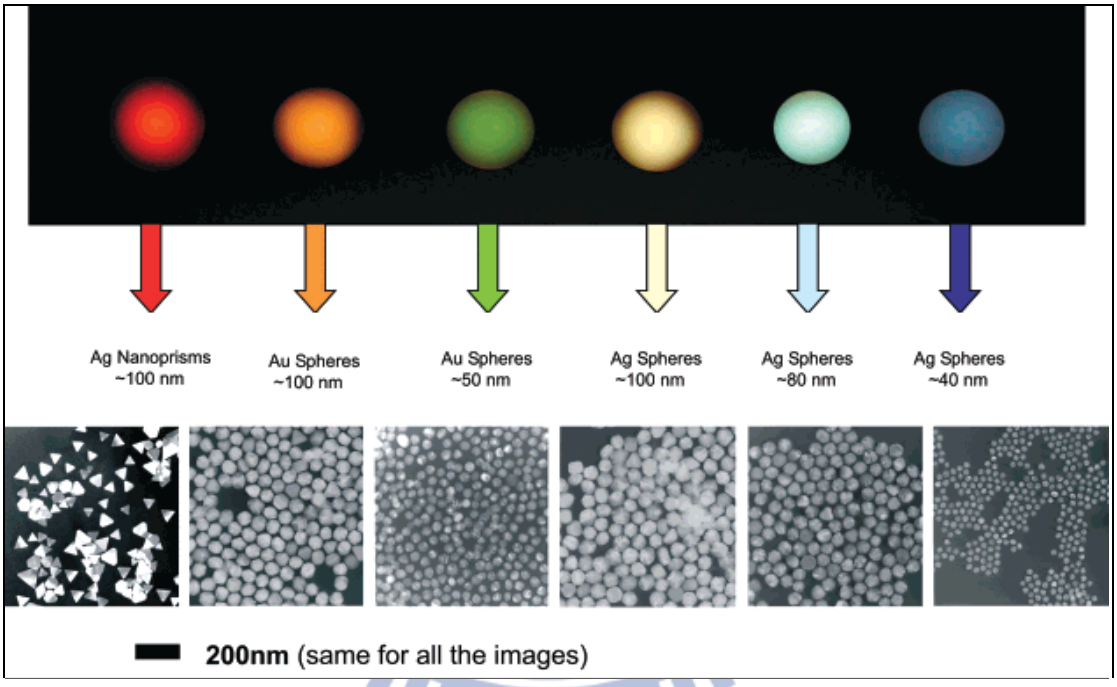

Figure 1.3 Sizes, shapes, and compositions of metal nanoparticles can be systematically varied to produce novel materials with distinct light-scattering properties.[1]

1.3 Applications of Nanoparticles in Biology

In the last few years, NPs has received much attention.[5,21] Nanometer (nm)-sized particles have attracted a great deal of attention due to their fascinating properties and potential applications in nanotechnology and biotechnology. NPs, i.e. particles with structures approximately 1–100 nm in size, have significant impact in many scientific fields, including chemistry, material sciences, biology, medicine, and electronics (See

Figure 1.4).[6,22] They provide a particularly useful platform, demonstrating unique properties with potentially wide-ranging therapeutic applications.[15,23] The physical, material, and chemical properties of NPs are directly related to their intrinsic compositions, apparent sizes, and extrinsic surface structures;[24,25] therefore, the design, synthesis, characterization, and applications of nanostructures are critical aspects for the emerging field of nanomaterials. One of the hottest areas for NPs use is in biological systems, owing to their potential application in medicine. Since structures can be accurately designed on the nanometer scale they can be incorporated into biological systems, due to the similar size scales.[21] Biological systems are complex, with synthesis, structure, and function all rarely understood in detail. The ability to rationally design structures on the same size as biological molecules generates the ability to probe and modify biological systems. Furthermore, biological systems are used to build up nanomaterials of specific shape and function. Nanostructures are being used as drug delivery agents, labeling agents, sensors, and to enhance electromagnetic fields. The field of nanotechnology has received increasing attention over the last 20 years, and the number of publications of NPs has grown exponentially. The field of NPs in biology is certainly a burgeoning one, with the estimated number of papers in the area (based on Web of Science) rising from 11 in 1991 to over 10000 in 2010. This increase in the available NPs generates an increase in the number of applications, driving the potential for great advances in everyday life due to nanobiotechnology.[26]

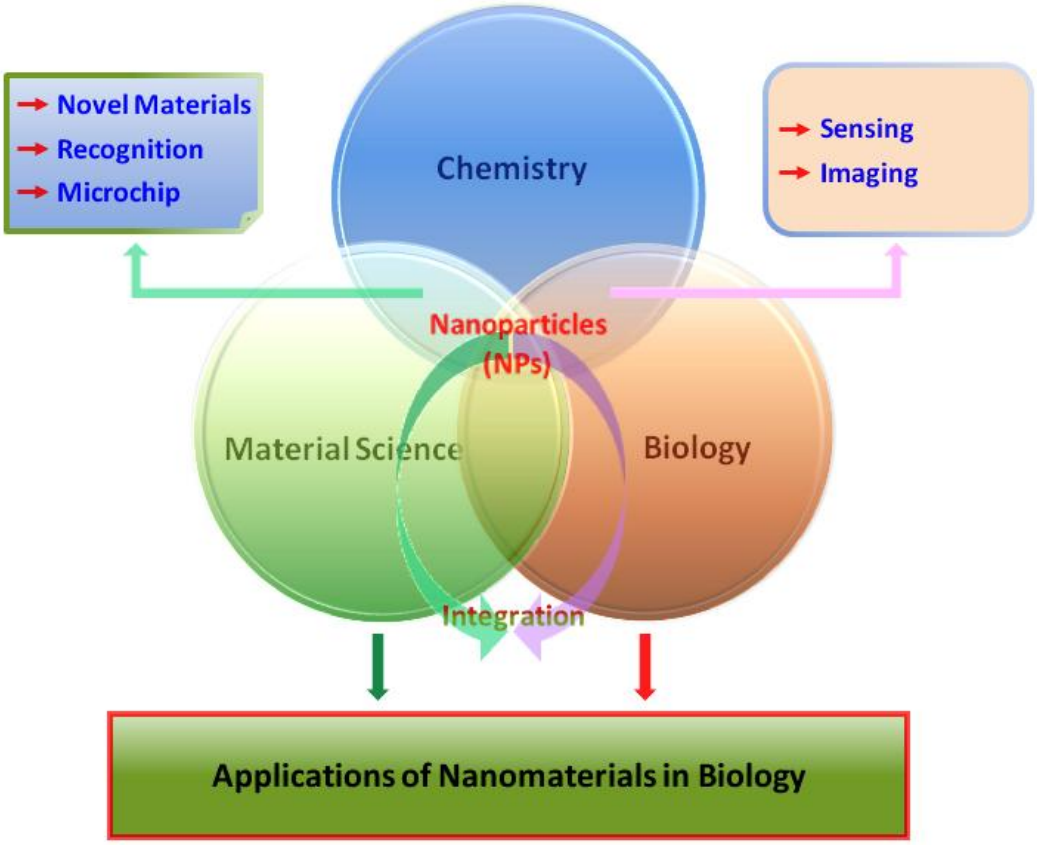

Figure 1.4 Chemistry is the central science for the development of applied disciplines such as materials research and biotechnology. Nanoparticles, which is based on classic chemical research fields and engineering technologies, has led to enormous advances in tailoring advanced nanobiotechnology.

Because of several fundamental features,[1] biomaterials are important future building blocks for NP architectures: 1) Biomaterials display specific and strong complementary recognition interactions, for example, antigen–antibody, nucleic acid–DNA, and hormone–receptor interactions. The functionalization of NPs with biomolecules could lead to biomolecule–nanoparticle recognition interactions and thus to self-assembly. 2) Various biomolecules contain several binding sites, for example, antibodies exhibit two Fab (antigen-binding fragment) sites, whereas streptavidin or concanavalin A each display four binding domains. This allows the multidirectional growth of NP structures. 3) Proteins may be genetically engineered and modified with specific anchoring groups. This facilitates their aligned binding to NPs or the site-specific linkage of the biomaterial to surfaces. Consequently, the

directional growth of NP structures may be dictated. Furthermore, other biomaterials, such as double-stranded DNA, may be synthetically prepared in complexrigidified structures that act as templates for the assembly of nanoparticles by intercalation, electrostatic binding to phosphate groups, or association to functionalities tethered to the DNA. 4) Enzymes are catalytic tools for the manipulation of biomaterials. For example, the ligation or the endonuclease scission processes of nucleic acids provide effective tools for controlling the shape and structure of biomolecule–NP hybrid systems. In this context, it is important to note that Mother Nature has developed unique biocatalytic replication processes. The use of biocatalysts for the replication of biomolecule–NP conjugates may provide an effective system for the formation of nanostructures of predesigned shapes and compositions.[22,24]

NPs possess several distinctive physical and chemical attributes that make them promising synthetic scaffold for the creation of novel chemical and biological systems. The unique properties and utility of NPs arise from a variety of attributes, including the similar size of NPs and biomolecules such as proteins and polynucleic acids. Additionally, NPs can be fashioned with a wide range of metal and semiconductor core materials that impart useful properties such as fluorescence and magnetic behavior.[27,28] The use of biocatalysts for the replication of biomolecule–NP conjugates may provide an effective system for the formation of nanostructures of predesigned shapes and compositions. These properties of NPs have been harnessed by a number of groups to provide effective binding of proteins and DNA along with a control over structure and function.[26,29] The current studies featuring the interactions of NPs with biological molecules can provide a stepping stone to a host of biomedical applications. The applicable properties of some well-known core materials and corresponding possible ligands used for surface functionalization with their possible applications are summarized in Table 1.1.

Table 1.1 Characteristics, ligands and representative applications for various metal and semiconductor materials

Core	Characteristics	Ligand(s)	Applications
Au	Optical absorption, fluorescence and fluorescence quenching,	Thiol, disulfide, phosphine, amine	Biomolecular recognition, delivery, catalysis, sensing
Ag	Surface-enhanced fluorescence	Thiol	Sensing
Pt	Catalytic property	Thiol, phosphine, amine,	Bio-catalyst, sensing
CdSe	Luminescence, photostability	Thiol, phosphine, pyridine	Imaging, sensing
Fe_2O_3	Magnetic property	Diol, dopamine derivative, amine	MRI and biomolecule purification
SiO_2	Biocompatibility	Alkoxysilane	Biocompatible by surface coating

NPs are attracting substantial interest in the rapidly developing area of nanobiotechnology.[30,31] Biomolecule-functionalized NPs could be exploited for numerous applications in biomolecular electronics,[32,33] biosensors,[15,34,35] immunoassays,[26,36] and medicine,[5,37] namely in photodynamic anticancer therapy, targeted delivery of radioisotopes, drug delivery, electronic DNA sequencing, nanotechnology of gene-delivery systems, and gene therapy in Figure 1.5.[24,38] Novel fascinating areas of technologies are feasible with the use of bionanomaterials. A combination of the unique properties of nanoobjects and biomaterials provides a unique opportunity for physicists, chemists, biologists, and material scientists to mold the new area of nanobiotechnology.[25,39] Based on recent advances in the field, exciting new science and novel systems can be anticipated from this interdisciplinary effort. Future advances will require continued innovations by nanotechnology in close collaboration with experts in medical and biological fields.

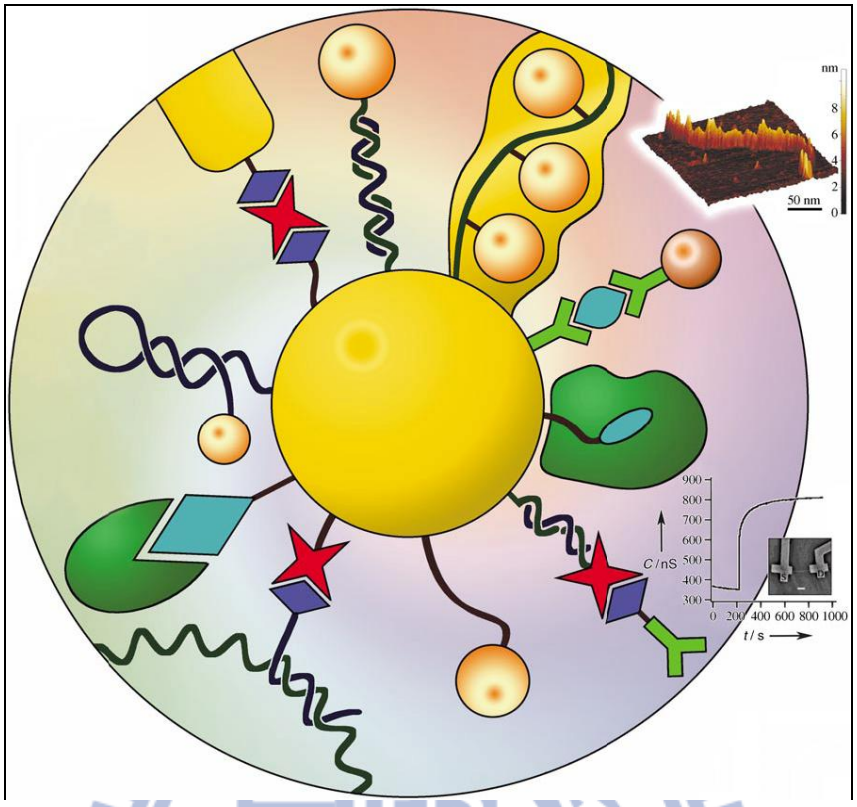

Figure 1.5 Integrated nanoparticle–biomolecule hybrid systems.[24]

1.4 Nanoparticle–Biomolecule Interactions

Biomolecule surface recognition by NPs as artificial receptors provides a potential tool for controlling cellular and extracellular processes for numerous biological applications such as transcription regulation, enzymatic inhibition, delivery, and sensing.[1,5,26] The size of nanoparticle cores can be tuned from 1.5 nm to more than 10 nm depending on the core material, providing a suitable platform for the interaction of NPs with proteins and other biomolecules.[40] The conjugation of NPs with proteins/enzymes can be done by using two different approaches, direct covalent linkage and non-covalent interactions between the particle and biomolecules.[6] The most direct approach to the creation of integrated biomolecule–NP conjugates is through covalent attachment. This conjugation can be achieved either through chemisorptions of the biomolecule to the particle surface or through the use of

heterobifunctional linkers. Chemisorption of proteins onto the surface of NPs (usually containing a core of Au, ZnS, CdS, and CdSe/ZnS) can be done through cysteine residues that are present in the protein surface (See Table 1.2).[27,41] By using the heterobifunctional linkers, biomolecules are often covalently linked to ligands on the NP surface *via* traditional coupling strategies such as carbodiimide-mediated amidation and esterification.

Table 1.2 Strategies for labeling a specific residue that involve direct linkage to the NP core

Labeled residue–NP material	Examples of labeled protein	Molecular weight
Cys–Au	Cytochrome *c*	12.6 kDa
	Ribonuclease *S*	13.7 kDa
	70 s ribosome	2.5 MDa
	Single chain Fv antibody	25 kDa
	Chaperonin	60 kDa
Cys–CdSe/ZnS	Human serum albumin	67 kDa
	α-chymotrypsin	21.6 kDa
	Chaperonin	60 kDa

Interactions between biomolecules form the basis for a number of cellular processes such as protein–protein interactions, protein–nucleic acid interactions, enzyme activity, and cell surface recognition.[41] Modulation of these interactions through creation of efficient receptors designed to recognize biomolecules such as proteins and nucleic acids paves the way for alternative approaches to therapeutic agents, as well as diagnostic biosensors for rapid monitoring of imbalances and illnesses.[42] The regulation of the protein activity plays an important role in modulating cellular processes such as signal transduction, DNA replication, and metabolism. Protein dysfunction is related to human diseases and disorders, and the ability to regulate enzyme functions and protein–protein interactions provides a promising strategy for therapy.[26] NPs have some advantages over small organic

molecules. First, NPs have large specific surface areas for adequate protein binding and biological interactions. Second, NP can enter cells easily, in contrast to some small molecules and biological molecules. Third, there has been considerable progress in the synthesis of NPs with well controlled dimensions, geometry, and surface properties, to complement the structural complexity of proteins. Recent developments in nano materials offer a new pathway for controlling protein behavior through surface interactions. The field of NP labeling of proteins is relatively new and rapidly developing.

1.5 Surface Interaction of Biomolecules with Gold Nanoparticles

NPs of various dimensions, compositions, and surface modifications have been studied on their interactions with biomolecules.[41,43] The main challenge often lies in understanding the interface between biological and non-biological materials on the nano-scale. The development of new tools for the controlled manipulation of such materials is clearly of great importance.[13,14] Recently, some research efforts have been conducted to investigate the effects of gold NPs (AuNPs) on the modulation of enzyme activity through surface interactions.[26] Although gold is the subject of one of the most ancient themes of investigation in science, its renaissance now leads to an exponentially increasing number of publications, especially in the context of emerging nanoscience and nanotechnology with NPs.[42,44] AuNPs also called gold colloids, and they present fascinating aspects such as their assembly of multiple types involving materials science, the behavior of the individual particles, size-related electronic, magnetic and optical properties (quantum size effect), and their applications to catalysis and biology (See Table 1.1).[5,14,29]

For further developing AuNPs-based assays, attaching the molecular recognition motifs of interest to the NPs has to be readily achieved, and, most importantly, the functional AuNPs (AuNP probes) should not cross-talk with each other or with anything else present in the system under investigation. Stabilization and functionalization of AuNP probes has been extensively studies.[45,46,47] To improve the selectivity and accuracy, various stabilizer/ligands and modified methods have been developed to enhance the stability and dispersity of AuNPs because keeping monodispersity of AuNPs in the reaction medium is the key issue in biological applications. Electrostatic interaction, covalent coupling (Au−S covalent etc.), and specific recognition (antibody−antigen, biotin−avidin, DNA hybridization etc.) are three kinds of widely used methods for the synthesis of AuNP probes to meet the application requirements (See Figure 1.6).[6] Electrostatic interaction or physical adsorption immobilization of ligands for AuNP probes is a simple process with the benefits of time saving and reduced complexity of ligand preparation.[45] However, the binding is not strong enough to yield stable surfaces capable of withstanding the necessary washing steps and incubation conditions in biological studies on subsequent reaction. Thiol chemistry has been widely used for the modification on gold surfaces, the functionality of thiolate-modified AuNPs (Au−S covalent coupling) *in vivo* is limited to only a few days because of the limited oxidative stability of thiolate species,[48,49] as well as exchange reactions with thiolated compounds inside the body. Thiolate-modified surfaces are also damaged by exposure to light, high temperature and oxygen.[50] The stability of thiol–Au bond is not sufficiently long-lasting, especially *in vivo*.

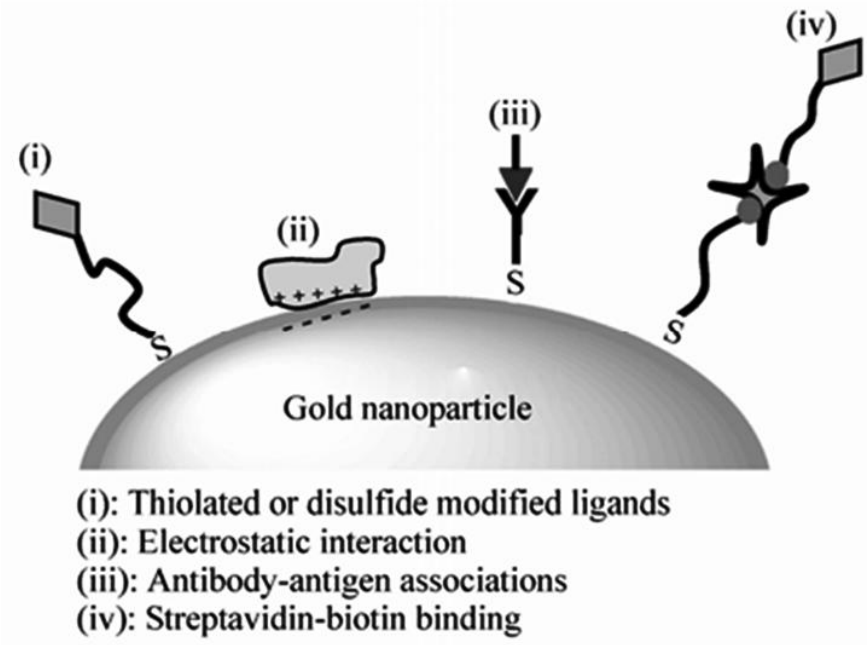

Figure 1.6 Schematic representation of the formation of gold nanoparticle probes.[6]

AuNPs have some advantages for the immobilization of biomolecules. First, AuNPs have large specific surface areas for adequate biomolecules binding and biological interactions. Second, there has been considerable progress in the synthesis of AuNPs with well controlled dimensions, geometry, and surface properties, to complement the structural complexity of proteins. Third, AuNPs have a highly promising and reliable utilization due to their high surface-to-volume ratio, long-term stability, easy synthesis, and favorable chemical modification.[44] In the past few years, AuNPs have been widely investigated to understand their interactions with proteins. The hydrophobic interaction, π–π stacking and electrostatic interaction have been attributed to be major mechanisms of biomolecule–AuNP interactions.[26,41,51]

Chapter 2: Literatures Review

2.1 General Introduction: Applications of AuNPs in Nanobiotechnology

Colloidal gold was used to make ruby glass and for coloring ceramics and these applications are still continuing now. It is ruby red in transmitted light and green in reflected light, due to the presence of gold colloids. In the 20th century, various methods for the preparation of gold colloids were reported.[52,53,54] In the past decade, gold colloids have been the subject of a considerably increased number of books and reviews.[55,56,57,58] Gold nanoparticles (AuNPs), which have been known for 2500 years, are the subject of an exponentially increasing number of reports and biomedical applications in the 21st century, using the "bottom-up" approach with the hybrid organic-inorganic and biological-inorganic building blocks derived wherefrom. They are gradually attracting a great deal of attention for their use in technologies, including catalysis, optical material, electronic device, biosensor, drug carrier, and high contrast cell image.[42,44,59] AuNPs have widely been used in nanotechnology due to size-dependent electrical property, high electrocatalytic activity, and functional compatibility with molecules and polymers. They are the most stable metal NPs, which have high affinity for biomolecules, have been used as biosensors,[15,60] immunoassays[26,36] and vectors for drug delivery;[5,61] thus, the conjugation of AuNPs and biomolecules has become a major area of research for advancing the use of nanotechnology in biomedical applications.[46, 62 , 63] Recently, there are many applications that were combined with biomolecules and AuNPs. In the following section, we will review some important literatures in the field of nanobiotechnology with AuNPs.

2.1.1 Oligonucleotide-Modified AuNPs

AuNPs exhibits unique optical and electronic properties based on size and shape.[25] Spherical AuNPs show an intense absorption peak from 500 to 550 nm[64] arising from surface plasmon resonance (SPR). The SPR band is sensitive to the surrounding environment, signaling changes in solvent and binding. A particularly useful output is the red-shift (to ca. 650 nm) and broadening of the plasmon band due to the NP aggregation.[2] This phenomenon leads to the popular and widely applicable colorimetric sensing.

An early indication of the potential of nanomaterials as biodetection agents was reported in 1996 by Mirkin's group[65] (Prof. Chad A. Mirkin, Department of Chemistry and International Institute for Nanotechnology, Northwestern University) with the observation that oligonucleotide-modified nanoparticles and sequence-specific particle assembly events, induced by target DNA, could be used to generate materials with unusual optical and melting properties. Specifically, when 13-nm gold particles were used in the assay, the color of the solution changed from red to blue upon the analyte-directed aggregation of gold nanoparticles, a consequence of interacting particle surface plasmons and aggregate scattering properties. Further studies indicated that the melting profiles of the nanoparticle-labeled DNA aggregates were extraordinarily sharp, occurring over a temperature range much narrower than the transition for unlabeled or conventional fluorophore-labeled DNA (See Figure 2.1). These two observations, both consequences of the high surface area and unique optical activity of the AuNPs, created worldwide interest in exploring the potential for designer nanomaterials in biodiagnostic applications.

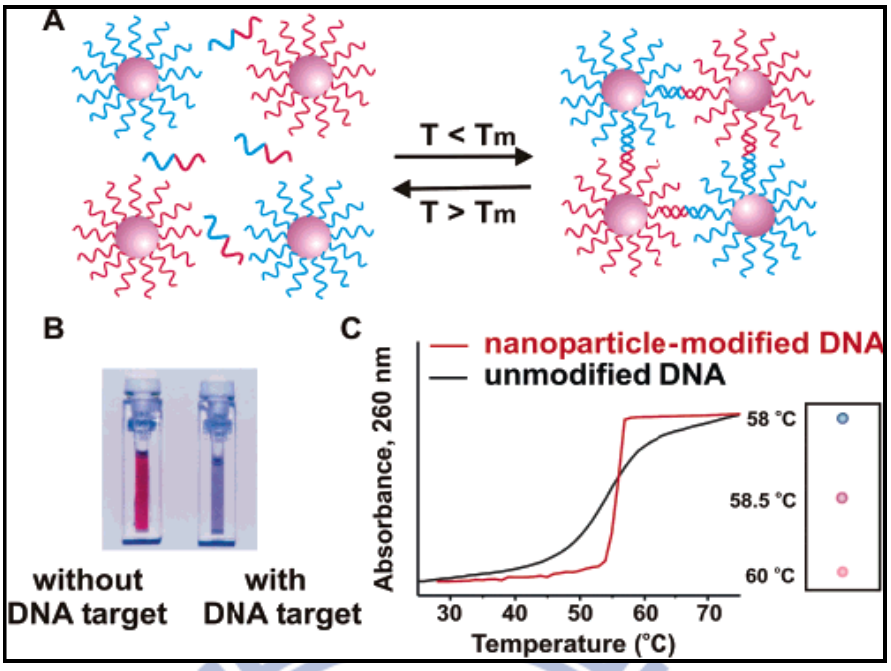

Figure 2.1 In the presence of complementary target DNA, oligonucleotide-functionalized gold nanoparticles will aggregate (A), resulting in a change of solution color from red to blue (B). The aggregation process can be monitored using UV–Vis spectroscopy or simply by spotting the solution on a silica support (C).[65]

After discovering this property, Mirkin's group have also quantitatively determined and compared the thermodynamic values of oligonucleotide functionalized AuNP probes and molecular fluorophore probes of the same sequence. Between 2000 to 2005,[66,67,68] they report a series of experiments and a theoretical model designed to systematically define and evaluate the relative importance of nanoparticle, oligonucleotide, and environmental variables that contribute to the observed sharp melting transitions associated with DNA-linked nanoparticle structures. These variables include the size of the NPs, the surface density of the oligonucleotides on the NPs, the dielectric constant of the surrounding medium, target concentration, and the position of the NPs with respect to one another within the aggregate (See Table 2.1 & 2.2).

Table 2.1 Melting temperatures and enthalpies for different sized nanoparticles in the solution aggregate system[67]

particle diameter (nm)	T_m (^oC)	$\triangle H_{ICT}$ (kcal/mol)
13	50.0	275.8
31	49.0	473.8
50	48.5	706.8

Table 2.2 Melting temperatures and enthalpies for different surface densities of probe oligonucleotides on the nanoparticles in the solution aggregate system[67]

surface density of probe oligonucleotides	T_m (^oC)	$\triangle H_{ICT}$ (kcal/mol)
33%	51.3	326.0
50%	52.5	415.0
100%	54.5	503.9

The modification of oligonucleotides onto the surfaces of AuNPs has attracted great interest because of the potential to employ the programmability of DNA base-pairing to organize nanocrystals in space, providing many approaches for the applications in biological system. The oligonucleotide-mediated AuNPs have been extensively used for the development of drug delivery and gene therapy. In 2006, Mirkin *et al.* describe the use of AuNP–oligonucleotide complexes as intracellular gene regulation agents for the control of protein expression in cells (Figure 2.2).[61] These oligonucleotide-modified NPs have affinity constants for complementary nucleic acids that are higher than their unmodified oligonucleotide counterparts, are less susceptible to degradation by nuclease activity, exhibit greater than 99% cellular uptake, can introduce oligonucleotides at a higher effective concentration than conventional transfection agents, and are nontoxic to the cells under the conditions studied. By chemically tailoring the density of DNA bound to the surface of AuNPs, they demonstrated a tunable gene knockdown (Figure 2.3), thus opening the door for new possibilities in the study of gene function and nanotherapies.

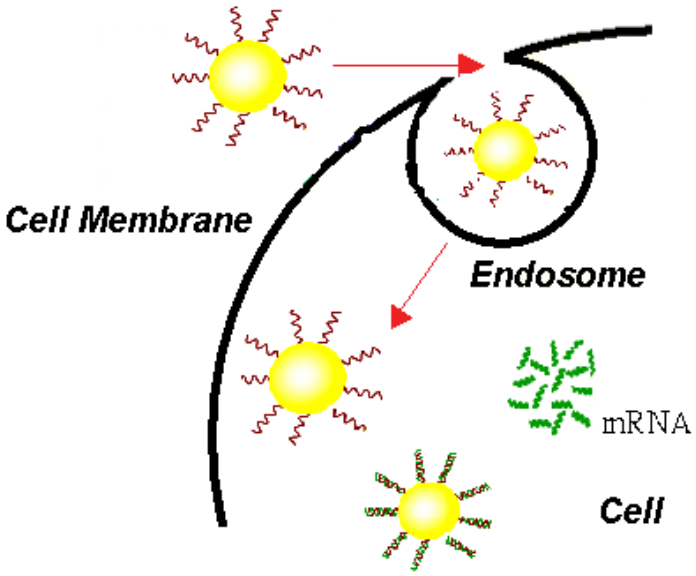

Figure 2.2 The diagram of using of AuNP–oligonucleotide complexes as intracellular gene regulation agents for the control of protein expression in cells.

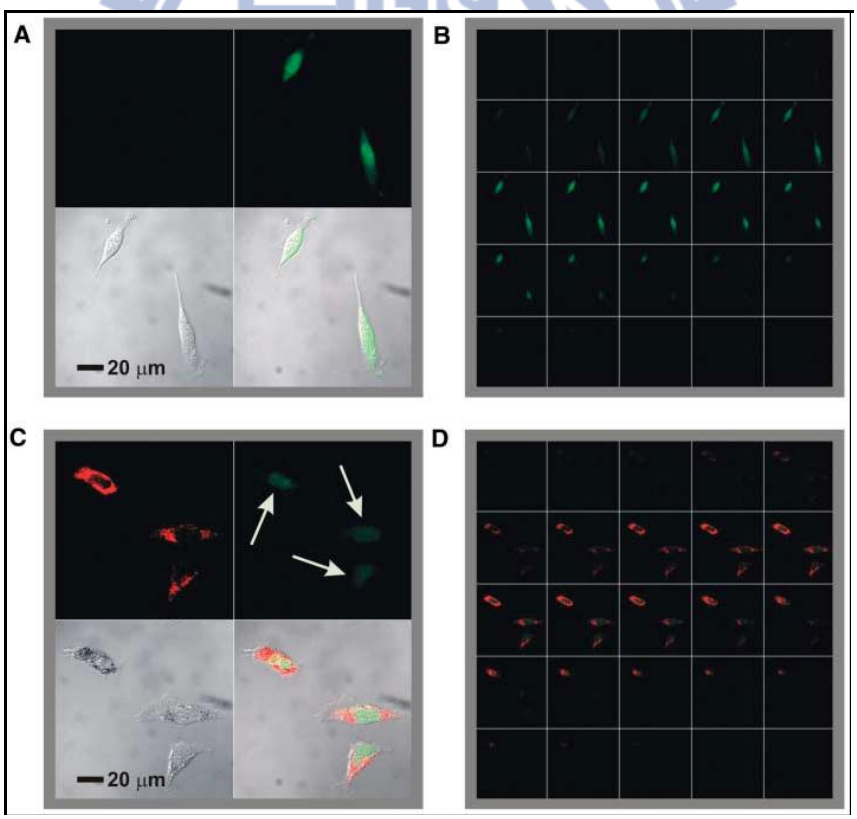

Figure 2.3 Confocal fluorescence microscopy images showing EGFP knockdown. (A) Untreated control cells (upper left, Cy5.5 emission, 706 to 717 nm; upper right, EGFP emission, 500 to 550 nm; lower left, transmission image of cells; lower right, composite overlay of all three channels) showed a significant amount of emission throughout the cell. (B) 1 mm sectioning images of control cells. (C and D) Cells treated with antisense particles showed a decrease in the amount of EGFP emission.[61]

In the following years, Mirkin's group has described a new class of intracellular probe termed nano-flares based on AuNP–oligonucleotide complexes.[69, 70] Nano-flares take advantage of the highly efficient fluorescence quenching properties of gold, cellular uptake of oligonucleotide NP conjugates without the use of transfection agents, and the enzymatic stability of such conjugates, thus overcoming many of the challenges to creating sensitive and effective intracellular probes.

In 2007,[69] the same group reported the design of nano-flares using 13 nm AuNPs since size particle is an efficient quencher, can be densely functionalized with oligonucleotides, and does not efficiently scatter visible light, which is important for designing optical probes with minimal interference. AuNPs were functionalized with thiolated oligonucleotides containing an 18-base recognition element to a specific RNA transcript sequence (See Figure 2.4c) *via* gold–thiol bond formation. Oligonucleotide-functionalized AuNPs were then allowed to hybridize with short cyanine (Cy5) dye-terminated reporter sequences capable of acting as "flares" when displaced by a longer target or target region (Figure 2.4a). In the bound state, the Cy5 fluorescence of the reporter strand is quenched due to proximity to the AuNP surface. In the presence of a target, the flare strand is displaced and liberated from the AuNP by forming the longer and more stable duplex between the target and the oligonucleotide-modified AuNP. Testing the nano-flare design using synthetic complementary targets demonstrates that the probes respond with a 3.8-fold increase in fluorescence signal upon target recognition and binding (Figure 2.4b). In contrast, the signal does not change in the presence of a noncomplementary target and is of comparable magnitude to background fluorescence. These results thus demonstrate that nano-flares are efficient at signaling the presence of a specific target.

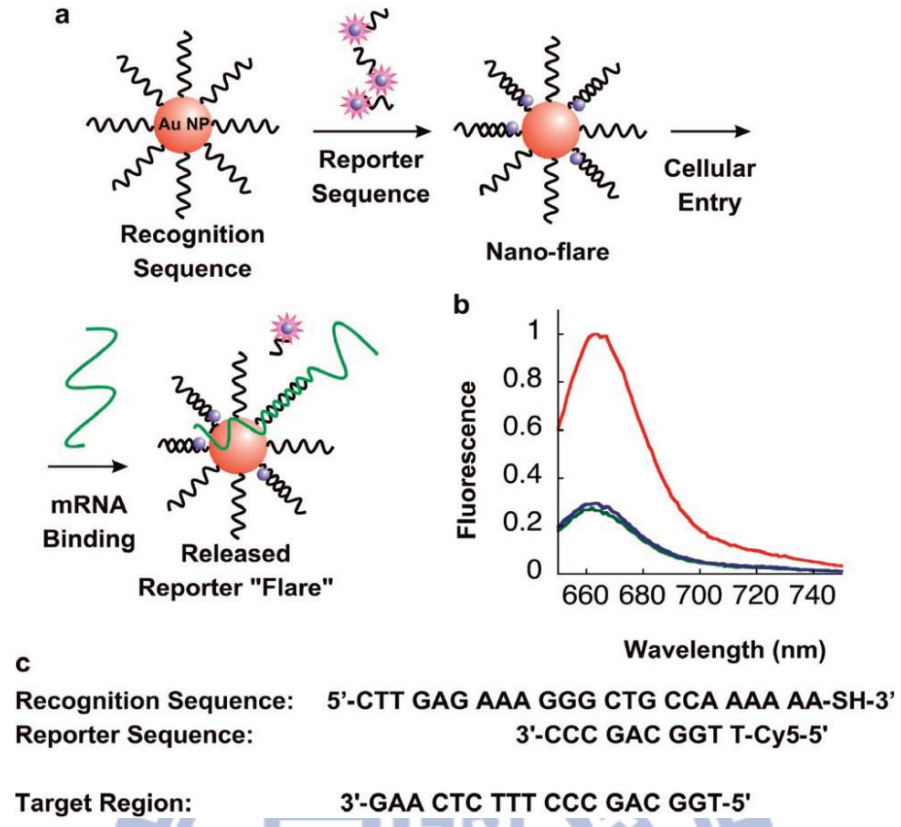

Figure 2.4 (a) Nanoparticles functionalized with a recognition sequenceare hybridized with a short complementary Cy5 labeled reporter strand, which is capable of being displaced by the target. (b) Fluorescence spectra of nano-flares alone (green), in the presence of target (red), and in the presence of noncomplementary sequence (blue). (c) Oligonucleotide sequences.[69]

In 2009,[70] based on the similar approach of nano-flares, the same group design a biosensor in the detection of adenosine triphosphate (ATP) and evaluate the ability to quantify the intracellular concentration of this target molecule. As illustrated schematically in Figure 2.5, nano-flares are designed so that the flare oligonucleotide binds to the aptamer that is attached to the surface of the AuNP. In the bound state, the fluorescence of the flare strand is quenched by the AuNPs. In the presence of the ATP target molecules, ATP binds to the aptamer causing a conformational change and resulting in a new folded secondary structure. This folded structure disrupts the Watson–Crick base-pairing between the aptamer and the flare, which causes flares to be liberated with an increase in fluorescence due to the greater distance of the flare from the gold surface.

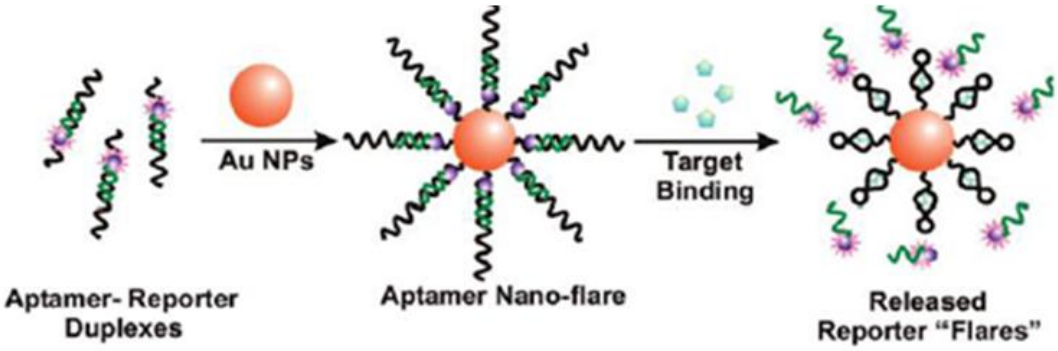

Figure 2.5 Aptamer nano-flares are gold nanoparticles functionalized with thiol-terminated aptamer sequences hybridized to a short complementary Cy5-labeled reporter strand. The reporter is capable of being displaced by a conformation change in the aptamer that is induced by the target molecule.[70]

In this new class of intracellular probe based on oligonucleotide-modified AuNPs, nano-flares are novel and potentially very useful since they are the only probe that combines cellular transfection, enzymatic protection, and RNA detection and quantification. Nano-flares will be of utility in other areas such as cell sorting, gene profiling, and real-time drug validation studies. Given the ability of these materials to also act as gene regulation agents, these probes may be easily adapted to simultaneously transfect, control, and visualize gene expression in real time.

2.1.2 Enzyme-Modified AuNPs

Enzymes, a class of proteins that exhibit high efficiency and specificity for catalyzing a myriad of reactions in complex cellular fluids, can be used to modify NP conjugates providing tools to detect enzyme activity, release drugs or control the formation of NP assemblies.[43,51] Pioneering work by Rotello's group (Prof. Vincent M. Rotello, Department of Chemistry, University of Massachusetts) has shown how the activity and substrate specificity of an AuNP–bound enzyme can be modulated by tuning the nanoparticle physicochemical properties.[26,41] In 2002,[71] Rotello *et al.* reported the mixed monolayer protected gold clusters (MMPCs) provide an effective scaffold for

biomolecular binding. MMPCs were synthesized using the Brust reduction and Murray place-displacement reaction to fabricate additional functionalized thiols ended with carboxylate groups and amino groups, respectively (MMPCs **1**, **2**, and **3** in Figure 2.6c featuring a 2-nm gold core, with an overall diameter of 6 nm as shown in Figure 2.6b). These NPs exhibited different effects on α-chymotrypsin (ChT) activity. The cationic MMPC **3** had no inhibition, while the anionic MMPC **1** and **2** were effective inhibitors of ChT because of the electrostatic complementarity between the carboxylate end groups and the hole of cationic residues (blue) located around the periphery of the active site, as shown in Figure 2.6a.

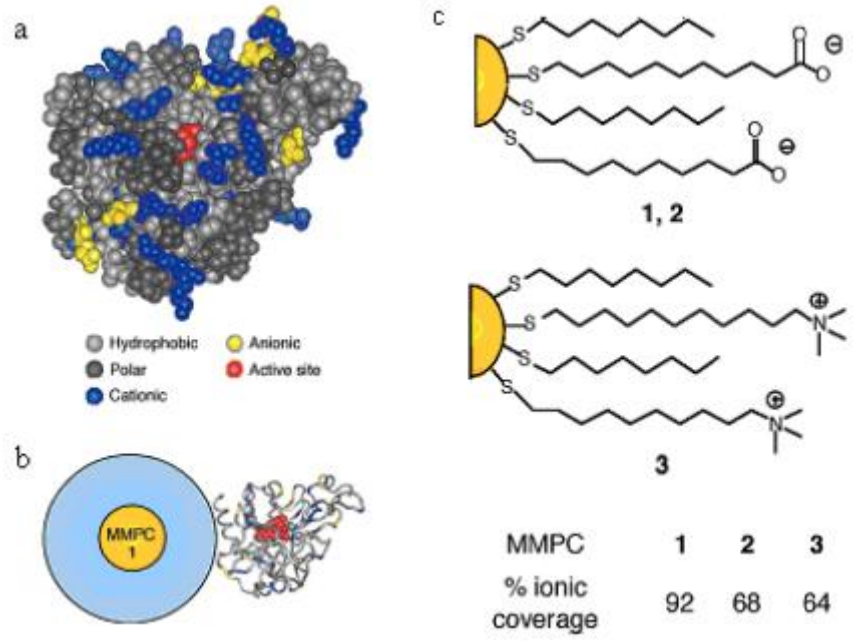

Figure 2.6 (a) Space-filling model of ChT. Surface binding of the proteins by anionic MMPCs focuses on the ring of cationic residues situated around the active site, functionally significant residues are noted. (b) Relative sizes of ChT and MMPC **1**. (c) Anionic MMPCs **1** and **2** and cationic control **3**.[71]

.

The inhibition displayed a two-step process featuring a fast reversible step due to complementary electrostatic binding followed by a slower irreversible process resulting in ChT denaturation on the nanoparticle surface. The binding ratio of the nanoparticle with the enzyme was found to be 1:5, which indicated a complete

saturation of the MMPC surface with the protein, given their relative surface areas. Circular dichroism (CD) measurements of the complex demonstrated an almost complete denaturation of the enzyme over time. Dynamic light scattering (DLS) studies confirmed that inhibition proceeded without substantial MMPC aggregation. The electrostatic nature of the engineered interactions provides a level of selectivity as elastase, β-galactosidase and cellular retinoic acid-binding protein displayed no significant interaction with MMPC.

In the following year (2003), Rotello *et al.* found that the "irreversible" inhibition of ChT can be reversed through modification of the anionic MMPC surface by the addition of cationic surfactants.[72] Four derivatives of trimethylamine-functionalized surfactants were used to modify the AuNPs with carboxylate groups (**4**, **5**, **6**, and **7** in Figure 2.7c, featuring a 2-nm gold core, with an overall diameter of 6 nm). Up to 50% of original ChT activity was rescued upon long-chain surfactant addition. DLS studies demonstrated that ChT released from the nanoparticle surface and the conformation characterization of the rescued ChT by fluorescence and fluorescence anisotropy indicated that ChT regained a high degree of native structure upon surfactant addition. The proposed mechanism of the ChT release: the MMPC **5** and MMPC **6** can elicit ChT release by interaction or partial displacement of the anionic monolayer. The MMPC **4**, a bilayer-type structure, can release ChT when it envelops the MMPC surface, as shown schematically in Figure 2.8. The non-covalent nature of the irreversible inhibition of ChT shows that the attenuation of the interactions the MMPC and protein could provide a means of enzyme activity modulation.

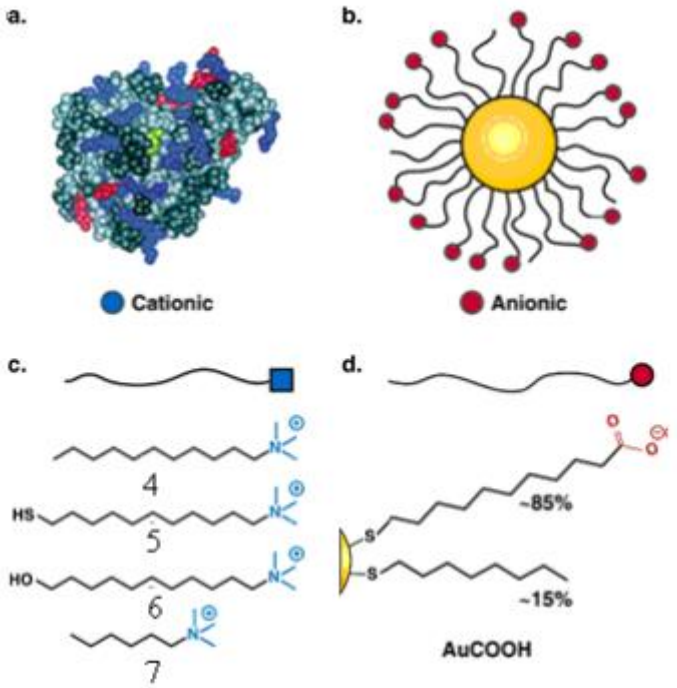

Figure 2.7 (a) Space-filling model of ChT. Active site (yellow) is surrounded by a ring of cationic residues (blue). (b) Amphiphilic MMPCs with anionic functional groups (carboxylate groups; red) in their terminals can interact with ChT *via* electrostatic complementarity. (c) Four derivatives of trimethylamine-functionalized surfactant used for surface modification of MMPC anionic monolayer. (d) Monolayer composition of AuCOOH as an effective inhibitor of ChT activity.[72]

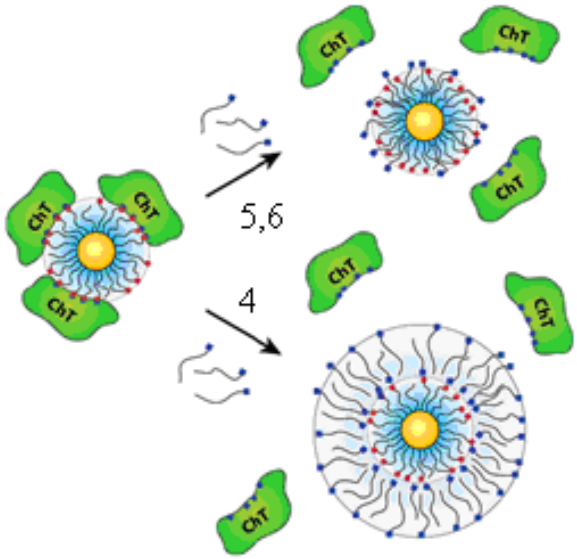

Figure 2.8 Proposed mechanism of ChT rescue. The surfactants with thiol MMPC **5** and alcohol MMPC **6** at their terminals have the ability to elict ChT release by interaction or partial displacement of the anionic monolayer. C_{11} alkane MMPC **4** forms a bilayer-like structure, causing release of the ChT (red = anionic; blue = cationic).[72]

In further investigations, Rotello's group have also studied the enzymatic kinetics of ChT upon binding to amino-acid-functionalized AuNPs toward different substrates and demonstrated that the complex formation provides a powerful tool to tune the enzyme specificity (*JACS* 2006).[73] As illustrated schematically in Figure 2.9, the association of ChT with anionic nanoparticles leads to the increase of specificity to the positively charged substrate and the decrease of specificity to the negatively charged substrate. Such enhanced substrate selectivity originates from the electrostatic interaction as well as the steric repulsion of the substrates with the NPs monolayer. This activity assay indicated that monolayer-functionalized NPs provide a potent scaffold for creation of an enzyme modulator based on surface recognition.

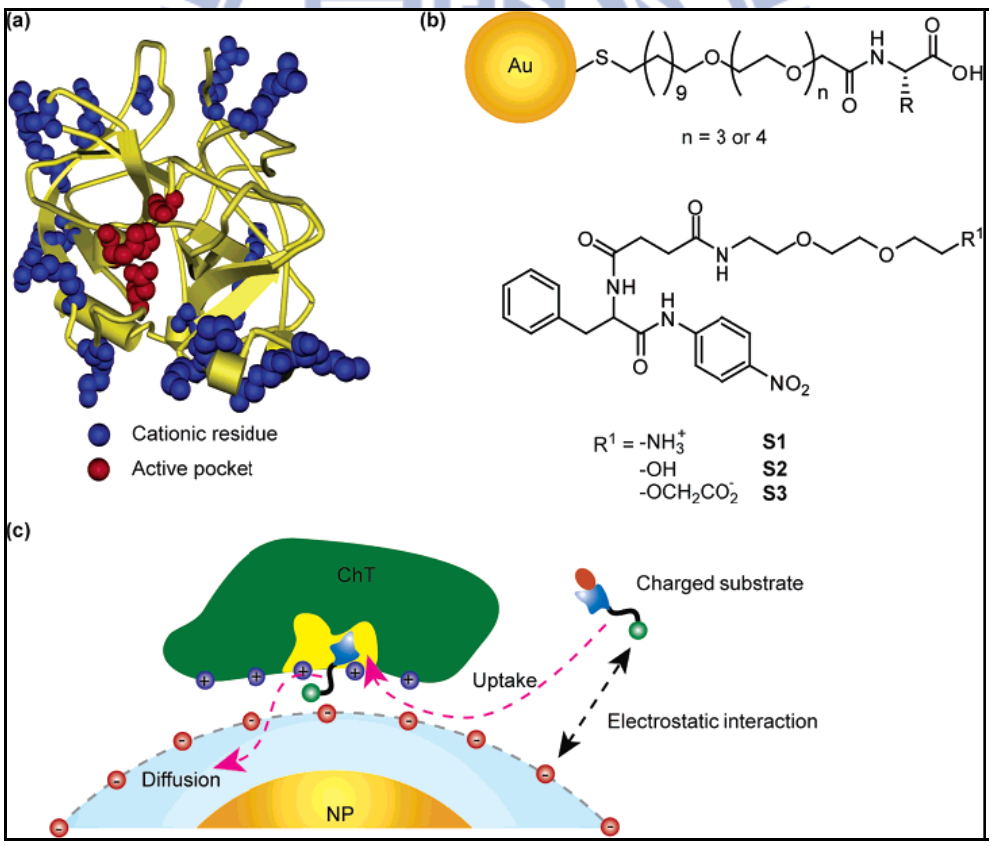

Figure 2.9 (a) Molecular structure of α-chymotrypsin (ChT). (b) Chemical structure of amino-acid-functionalized gold nanoparticles and substrates. (c) Schematic representation of monolayer-controlled diffusion of the substrate into and the product away from the active pocket of nanoparticles-bound ChT.[73]

In the following year (2007),[74] this group has also successfully designed a system whereby functionalized AuNPs promote the association and ligation of peptide fragments (E1 and E2). The Figure 2.10 demonstrated a clear increase in the rate of production with addition of cationic AuNPs as compared to the control reaction with no AuNPs. Increasing the amount of AuNPs induced a faster production rate, thereby demonstrating the ability of the cationic AuNPs to act as a template for ligation.

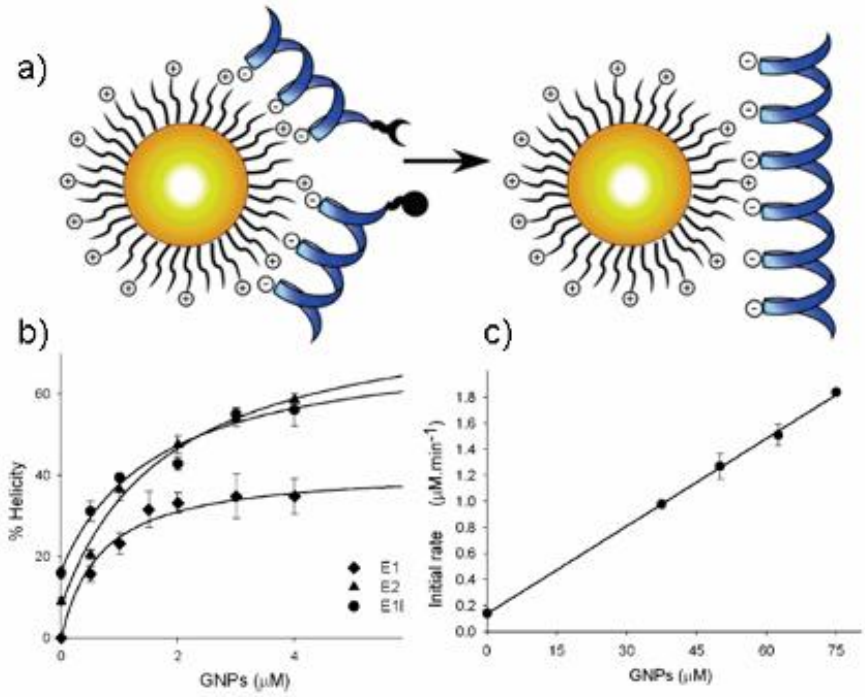

Figure 2.10 a) The design of functionalized, cationic AuNPs as a template for peptide ligation. b) Helicity of E1E2, E1, and E2 with added cationic AuNPs. c) Initial rate of E1E2 *versus* the concentration of AuNPs.[74]

2.1.3 Effect of Nanoparticle Size on Enzyme Activity

The size of NPs is also one of the key parameters that influence the interaction between protein and NPs. Dordick *et al.* performed a systematic study in which they investigate the structure of lysozyme adsorbed onto NPs that range in diameter from 4 nm to 100 nm.[75] Both structure and activity of the lysozyme are measured, by

circular dichroism (CD) spectroscopy and colorimetric activity assays, respectively. The particle size is found to strongly influence the protein–particle interactions and consequently the protein behavior. The lysozyme retains its structure when on the smaller NPs, and denaturation increases with increasing particle size. In addition, activity is highest on the smallest particles and lowest on the largest particles. These results indicate that the size of the NP, perhaps because of the contributions of surface curvature, influences adsorbed protein structure and function (Figure 2.11).

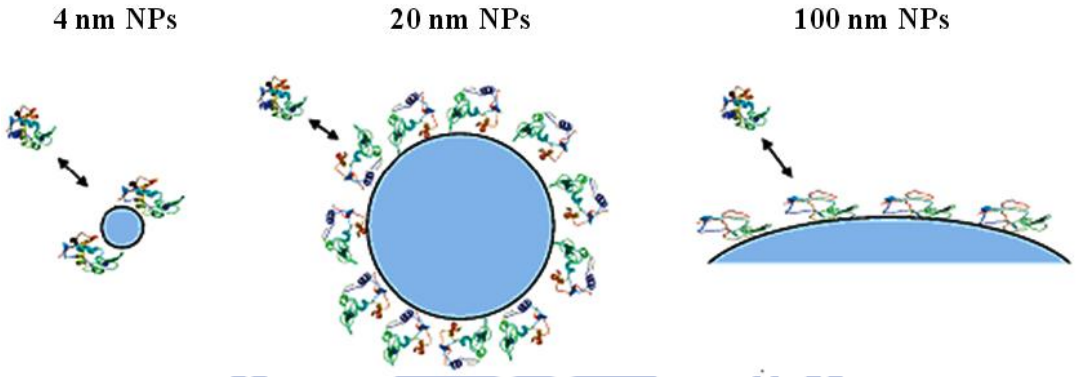

Figure 2.11 Schematic of lysozyme adsorption on nanoparticles with different sizes. Stronger protein particle interactions exist in the case of larger nanoparticles, resulting in more protein unfolding and less enzymatic activity.[75]

In 2010,[76] Das *et al.* reported the same phenomenon when lipase was absorbed onto AuNP surfaces with different sizes. Activity analyses showed that the improved activity because of enhancement in the substrate selectivity and increased flexibility in the enzyme conformation. The extent of the activation is greater in the case of the larger-sized AuNPs. A correlation has been established between the activity of lipase and its secondary structure by using CD and FTIR spectroscopic analysis. Therefore, NP size is most likely a general effect, which is probably present in conjugates for proteins on NPs. These studies demonstrate that NP size can be used to modulate protein activity, which can form the basis of a number of biological applications.

2.1.4 Summary

Gold nanoparticles present a versatile scaffold for recognition of biomolecular surfaces. The NP size can be tuned for optimally scaled systems for biomolecules, their surfaces can undergo divergent functionalization and importantly, the nanoparticle surface can be templated to the guest surface providing an environmentally responsive receptor for biomolecules. The surface and core properties of these systems can be engineered for individual and multimodal applications, including biomolecular recognition and biosensing as discussed in this section. These properties of AuNPs have been harnessed by a number of groups to provide effective binding of proteins and DNA along with a control over structure and function. The current studies featuring the interactions of nanoparticles with biological molecules can provide a stepping stone to a host of biomedical applications.

AuNPs present a highly attractive platform for a diverse array of biological applications. The ability of functionalized NPs in mediating biomolecular recognition can be extended to development of novel hybrid materials composed of enzymes and NPs. The interaction between them is governed by the key properties of NPs, such as structure, size, surface chemistry, charge and surface shape. NPs can be selected to specifically bind enzymes and control their functions after surface modifications. Such NP–enzyme interactions can be fine-tuned to the regulation of enzyme activity provides a potent means to gain control over cellular processes such as signal transduction, DNA replication and metabolism in biological system.

2.2 Lipases

Lipases are used industrially as detergent enzymes, in paper and food technology, in the preparation of specialty fats, and as biocatalysts for the synthesis of organic intermediates, and in various clinical studies and drug delivery.[77,78,79] The kinetic model of lipases is based on the so-called ping–pong mechanism, which also applies to many other enzymes, such as glucose oxidase, horseradish peroxidase, and alkaline phosphatase. As a representative esterase, lipase is an excellent model for studying the enhanced activity of AuNP-bound enzymes because of its well-defined structure, properties, and applications. In this section, we will review some literatures to introduce lipases with the applications in the biocatalysts, structure, and reaction mechanism.

2.2.1 Interfacial Enzymes with Attractive Applications

Lipids are key elements in the chemistry of life. Most organisms use the supramolecular chemistry inherent to phospholipids to form their exterior and compartmental membranes. Many plants and animals store chemical energy in the form of triglycerides, which are sparingly soluble in water. For the metabolic turnover of these and other biochemicals, they produce esterases, enzymes which can hydrolyze bonds of water-soluble esters. Esterases which can hydrolyze triglycerides at the water/oil boundary are termed lipases and those which attack phospholipids are termed phospholipases.[77] Both types of enzymes have recently received considerable attention. Whereas phospholipases are involved in key metabolic events such as membrane turnover and signal transduction, lipases have diverse functions in the degradation of food and fat; they have qualified as valuable drugs against digestive disorders and diseases of the pancreas. They also find applications in biotechnology

and as catalysts for the manufacture of specialty chemicals and for organic synthesis. Furthermore, lipases play an important physiological role in the digestion of fat by mammals and humans, and lipase inhibitors may have a potential as antiobesity drugs.

2.2.2 Structure and Reaction Mechanism of Esterase

The protein structure underlying these observations remained a mystery until a few years ago. Only in 1990 were the first two lipase structures solved by X-ray crystallography. They revealed a unique mechanism, unlike that of any other enzyme: Their three-dimensional structures suggested that interfacial activation might be due to the presence of an amphiphilic peptide loop covering the active site of the enzyme in solution, just like a lid or flap.[80,81] From the X-ray structure of cocrystals between lipases and substrate analogues, there is strong indirect evidence that, when contact occurs with a lipid/water interface,[82] this lid undergoes a conformational rearrangement which renders the active site accessible to the substrate (Figure 2.12).

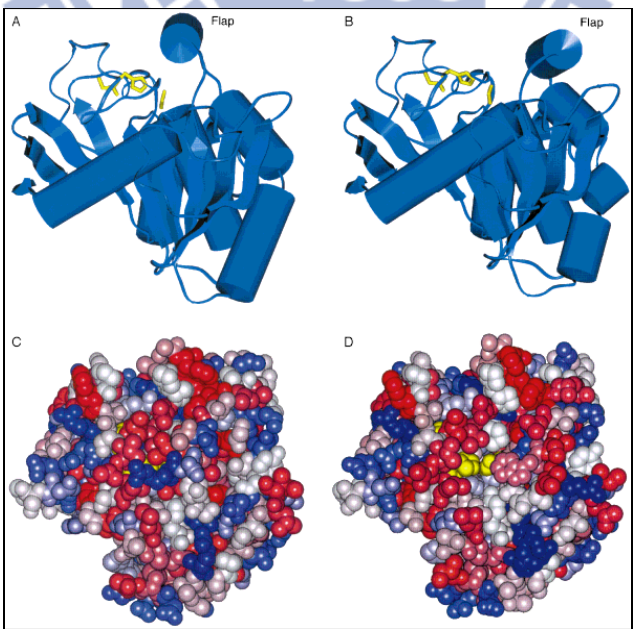

Figure 2.12 Structure of lipase in closed (A, C) and open form (B, D). A and B (side view): the catalytic triad (yellow) and secondary structure elements showing the α/β-hydrolase fold common to all lipases. Upon opening of the lid, the catalytic triad (yellow) becomes accessible (D).[77]

All lipases whose structure has hitherto been elucidated are members of the "α/β-hydrolase fold" family with a common architecture composed of a specific sequence of α helices and β strands.[83,84] They hydrolyze ester bonds by means of a "catalytic triad", composed of a nucleophilic serine residue activated by a hydrogen bond in relay with histidine and aspartate or glutamate (Figure 2.13).

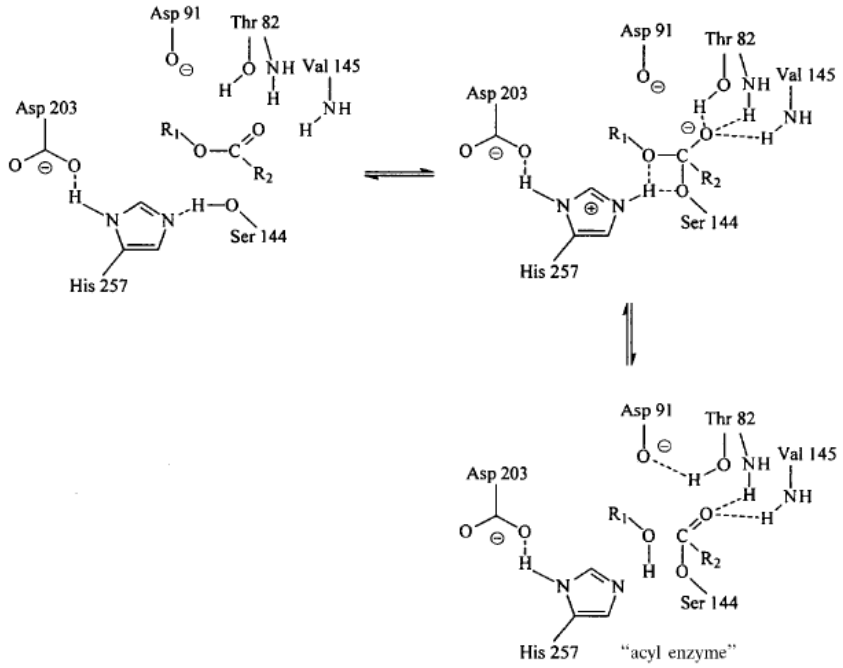

Figure 2.13 Catalytic mechanism of lipases based on a "catalytic triad" of serine (nucleophile), histidine, and aspartate or glutamate.[77]

As pointed out already, a unique structural feature common to most lipases is a lid or flap composed of an amphiphili α helix peptide sequence, which in its closed conformation prevents access of the substrate to the catalytic triad. After the lid has opened, a large hydrophobic surface is created to which the hydrophobic supersubstrate binds. This presumed mechanism is supported by the X-ray structures of lipases covalently complexed with hydrophobic inhibitors such as alkyl phosphonates, cycloalkyl phosphonates, or alkyl sulfonates.[85]

Chapter 3: Experiments

3.1 General Introduction

All the experiments were preceded at National Chiao Tung University (NCTU). All the equipments were also conducted in our laboratories at NCTU. The reagents were purchased commercially and used by following with the directions unless specially mentioned. These reagents were listed alphabetically in the form of "Name {abbreviation; chemical formula; purity; manufacturer}". Some information will be omitted if not available or not necessary. The following text will use the abbreviation of the reagents.

3.1.1 General Chemicals

Deionized and distilled water {DI water, ddH_2O}

The water we used was purified with filters, reverse osmosis, and deionized system until the resistance was more than 18 MΩ·cm. DI water was used to clean, wash, and be a solvent.

Hydrogen chloride {HCl; ≥99% purity; Sigma}

1 M hydrogen chloride (HCl) in DI water was used for pH adjustment.

Sodium hydroxide {NaOH; 95%; Showa}

1 N sodium hydroxide (NaOH) in DI water was used for pH adjustment.

Phosphate buffered saline tablets {PBS; 99.18%; Sigma}

PBS, a biological buffer solution, was used for all kinetic assay reaction. One tablet was dissolved in 200 mL DI water to yield 10 mM phosphate buffer, pH 7.4, 140 mM NaCl, 3 mM KCl.

Sodium chloride {NaCl; ≥ 99.5%; TCI (Tokyo Chemical Industry Co.)}

Sodium chloride (NaCl) was used to prepare salt solution or other biological buffer.

3.1.2 Synthesis of Colloidal AuNPs

Chloroauric acid trihydrate {$HAuCl_4 \cdot 3H_2O$; 99.9% purity; Sigma–Aldrich}

Chloroauric acid ($HAuCl_4$) is the main compound for the synthesis of gold nanoparticles (AuNPs).

Trisodium citrate dihydrate {$Na_3C_6H_5O_7 \cdot 2H_2O$; 98% purity; Showa}

For the preparation of colloidal AuNPs, trisodium citrate ($Na_3C_6H_5O_7$) was mixed into $HAuCl_4$ solution as a reductive reagent to reduce Au^{3+} to Au^0.

3.1.3 Immobilization of AuNPs on Silicon Wafer

Hydrogen peroxide {H_2O_2; ≥30% purity; Merck}

Hydrogen peroxide was mixed with sulfuric acid to form piranha solution which cleaned the silicon wafer surface.

Sulfuric acid {H_2SO_4; 98% purity; Merck}

Sulfuric acid was mixed with hydrogen peroxide (H_2O_2) in a 3:1 volume ratio to remove impurities on the surface of the oxidized silicon wafer. It should be noted that the cleaning solution is very corrosive and dangerous. We must handle it with carefulness and patience.

Dimethyl sulfoxide {DMSO; TCI}

It was a solvent for dissolving many hydrophobic organic compounds like 3-mercaptopropyltrimethoxysilane (MPTMS) in the experiment of the immobilization of AuNPs on a silicon wafer.

3-Mercaptopropyltrimethoxysilane {MPTMS; 99%; Sigma}

MPTMS solution in DMSO was used to create a thiol functional surface of the silicon wafer for the immobilization of AuNPs on it.

3.1.4 Activity Assay of Enzyme–AuNP Conjugated System

Lipase (EC 3.1.1.3) from *Candida rugosa* {CRL; Sigma}

CRL was immobilized on the surfaces of AuNPs, without any surface modification,

provided colloidal stability that allowed us to determine the coverage of enzyme onto the AuNPs and perform the kinetic experiments of the catalytic reaction.

Propan-2-ol {IPA; 99.8%; TCI}

It is an organic solvent for dissolving our substrate *p*-nitrophenyl palmitate (*p*NPP).

***p*-Nitrophenyl palmitate {*p*NPP; Sigma}**

Using UV–Vis spectrophotometry, we detected the activities of the enzyme-catalyzed reaction by measuring the absorbance of *p*-nitrophenol (*p*NP), a hydrolysis product from *p*NPP, at 405 nm. Prior to using this reagent for the activity assay, the powder was dissolved in the propan-2-ol (IPA) solvent.

Potassium cyanide {KCN; Showa}

To quantify the enzyme loading on the AuNPs, KCN was used to oxidize the CRL–AuNP conjugates in order to liberate bound enzyme from the surfaces.

3.2 Instruments

Scanning Electron Microscopy (SEM; JEOL, JSM-6700)

SEM is a very useful tool for observing surface morphology of specimen. SEM has secondary electrons or backscattered electrons detectors passing the signal to computer and forming image. In this study, AuNPs absorbed by certain functional groups modified on Si substrate were all characterized by a field-emission SEM operating at 20 kV accelerating voltage.

UV–Vis Spectroscopy (HITACHI, U-3310)

UV–Vis uses light in the range of near UV, visible and near infrared. The absorption in the light range is due to the optical properties of the chemicals involved. We determine the size of AuNPs and degree of AuNPs aggregation in the visible range of

400–800 nm. In protein quantification, it is necessary to observe the sulfonic acid derivative in the 300–500 nm by UV–Vis spectrometer.

X-ray Photoelectron Spectroscopy (XPS) & Fourier Transform Infrared Spectroscopy (FTIR)

To ensure that lipase can bind to the AuNPs, X-ray photoelectron spectroscopy (XPS) and fourier transform infrared spectroscopy (FTIR) were used to verify the attachment of the enzymes onto the surfaces of the AuNPs.

3.3 Experimental Methods

3.3.1 Synthesis and Characterization of Colloidal AuNPs

Citrate-stabilized AuNPs in a variety of diameters were synthesized using the classical Turkevich/Frens procedure.[86,87] Briefly, AuNPs of various sizes were prepared through the citrate-mediated reduction of chloroauric acid (See Figure 3.1). In this method, 40 mM $HAuCl_4 \cdot 3H_2O$ (250 μL) was added to DI water (9.75 mL) and brought to a boil. Next, trisodium citrate dihydrate (38.8, 25.9, 16.9, 15.5, or 13.9 mM; 1 mL) was added to the solution to produce differently sized AuNPs. Heating of the solution under reflux was continued until the color of the boiling solution changed from dark purple to purplish-red. After cooling to room temperature, colloidal AuNPs were formed in the solution, and filtered before use through a 0.45 μm syringe filter (Millipore).[88] To determine the concentration of each AuNP samples using UV–Vis spectroscopy, the molar extinction coefficients (ε) of the AuNPs having mean diameters of 13.1, 25.2, 37.5, 50.8, and 69.6 nm were 2.47×10^8 M^{-1} cm^{-1} at λ_{518}, 1.22×10^9 M^{-1} cm^{-1} at λ_{522}, 6.50×10^9 M^{-1} cm^{-1} at λ_{527}, 1.63×10^{10} M^{-1} cm^{-1} at λ_{531}, and 4.20×10^{10} M^{-1} cm^{-1} at λ_{536}, respectively. Absorption spectra and scanning electron microscopy (SEM) images confirmed the sizes and shapes of these AuNPs.

During the synthesis process we had to put much emphasize on the experimental environment, including container cleaning process, adding reducing agent as soon as possible, and continuously stirring during the synthesis step to prevent aggregation and prevent changing the size uniformity.

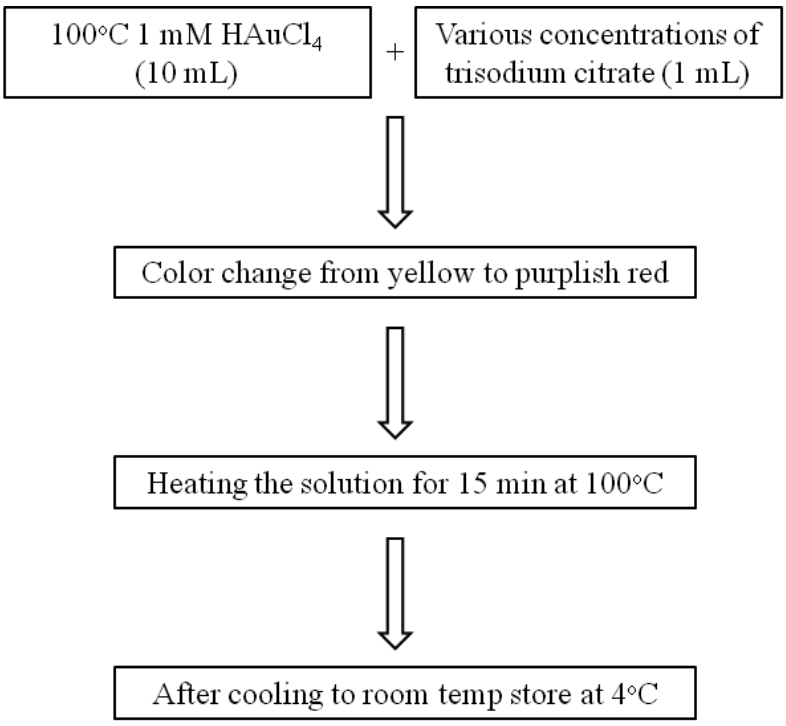

Figure 3.1 Schematic steps for the synthesis of differently sized gold nanoparticles.

3.3.2 Immobilization and Observation of AuNPs on Silicon Wafer

The corresponding process flow for the immobilization of AuNPs on silicon wafer was briefly illustrated in Figure 3.2. Prior to immobilization, the piece of oxidized silicon wafer was carefully cleaned in the piranha solution, H_2SO_4 and H_2O_2 (volume ratio is 3:1), twice, each time at above 85℃ for 30 min. It should be noted that the cleaning solution is very corrosive and dangerous. After rinsing with DI water and drying, the sample was immersed into a 2% MPTMS solution in DMSO to proceed the silanization reaction for 40 min at room temperature to create a thiol functional

surface. Following the MPTMS treatment, the silicon wafer was washed with DMSO for several times and rinsed with DI water thoroughly. Then, the treated silicon wafer was baked at 120℃ for 30 min to complete the Si–O bond formation. Each sample for SEM analysis was prepared by placing a few drops of the AuNP solution onto a silicon wafer modified with the MPTMS linker. The sample was rinsed with DI water for 10 min and then dried prior to viewing under the electron microscope. The SEM image was recorded using a JEOL JSM-6700F electron microscope operated at 20 kV. Particle size distribution of the AuNPs present in the SEM image, analyzed using a personal computer and Image-Pro Plus (IPP) software.

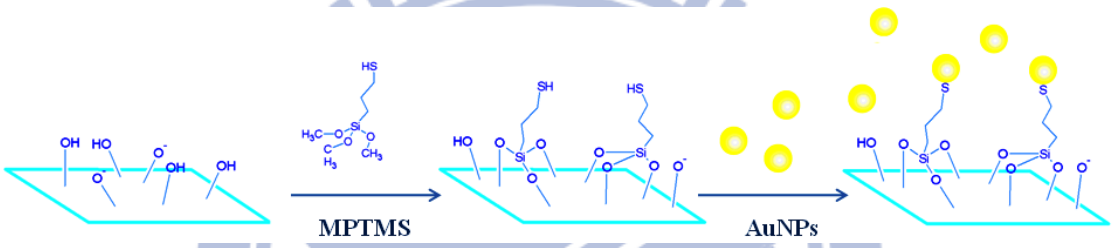

Figure 3.2 Self-assembly steps for the immobilization of gold nanoparticles onto silicon oxide surface.

3.3.3 Preparation of CRL–AuNP Conjugates

Prior to labeling the AuNPs with the enzyme (CRL), all the Au colloids were purified through centrifugation (13,000 rpm, 20 min) and re-dispersion in DI water. To avoid salt-induced Au aggregation, the CRL solution was desalted using Vivaspin 500 centrifugal concentrators, and then its concentration was determined by comparing the obtained absorbance (at 280 nm) with that of a standard curve prepared using known concentrations of CRL (ε = 3.7 × 10^4 M^{-1} cm^{-1} at 280 nm).[89] In the experiment of determining the enzyme coverage, the different concentrations of desalted CRL was added to the solutions incorporating AuNPs of various sizes and then the mixtures were incubated for 10 min. After the addition of salt solution, we displayed the plots of changes in the time-dependent absorption ratio in the presence of varying concentration of CRL.

3.3.4 Activity Assay of Free and AuNP-Bound CRL Systems

The reaction solution was prepared by mixing PBS solution (140 mM NaCl, 2.7 mM KCl, and 10 mM phosphate buffer; pH 7.4; 30℃; 1.3 mL), 0.5 mM *p*NPP in IPA (0.1 mL), and various concentrations of the free or AuNP-bound CRL (0.1 mL).[90] After mixing the catalytic substance with the reactants, the initial product release at the onset of the reaction was measured using a personal computer and a Hitachi UV–Vis-3310 enzyme reaction measurement system (a UV–Vis spectrophotometer possessing a temperature-controlled thermostatted cell holder; Hitachi, Tokyo, Japan). In the activity assays, the initial reaction of the change in absorbance at 405 nm was recorded (in real-time). The initial rate of the absorption change against the reaction time was converted to enzyme activity using a molar absorption coefficient of 14,100 M^{-1} cm^{-1} for the product of *p*-nitrophenol (*p*NP). Figure 3.3 describes the hydrolysis reaction of *p*NPP catalyzed by CRL.

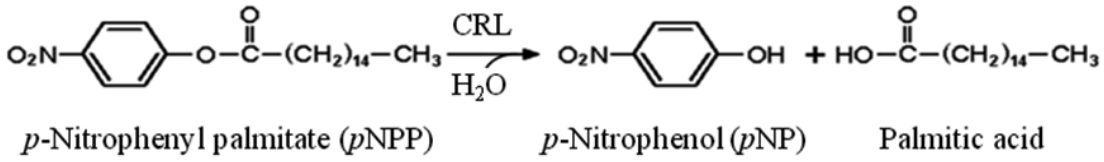

Figure 3.3 CRL-catalyzed hydrolysis of *p*NPP. The product, *p*NP, which provided strong absorption at 405 nm in the reaction solution, served as the reporter molecule for the progress of the enzyme-catalyzed reaction.

3.3.5 Michaelis–Menten Kinetics

In the experiment of kinetic analysis, various concentrations of the substrate (5.55, 8.33, 11.11, 16.67, 22.22, 33.33, 44.45, 66.67, 88.89, and 133.33 μM) were dissolved in the reaction solutions. The free or AuNP-immobilized enzyme was added to the various concentrations of the substrate in the assay buffer as described above. The plot of the initial velocity of the production of *p*NP *versus* the *p*NPP concentration was fitted to a hyperbolic curve. The values of K_m and V_{max} were obtained through nonlinear regression analysis using SigmaPlot 2001 (v. 7.0) and Enzyme Kinetics Module (v. 1.1, SPSS, Chicago, IL USA) software.[91] The assays were obtained in triplicate; average values were reported. All activity assay experiments were carried out at 30℃.

Chapter 4: An Enzymatic Kinetics Investigation into the Significantly Enhanced Activity through the Linker-Free Gold Nanoparticle Pathway

4.1 Background

Recent developments in nanomaterials offer a new pathway for controlling protein behavior through surface interactions.[41,51,92] The field of nanoparticles (NPs) labeling of biomolecules is relatively new and rapidly developing.[5,26,60] Gold nanoparticles (AuNPs), which have high affinity for biomolecules, have been used as biosensors,[42,60] immunoassays,[36] therapeutic agents,[5] and gene and drug delivery agents;[61] thus, the conjugation of AuNPs and biomolecules has become a major area of research for advancing the use of nanotechnology in biomedical applications.[6,25,93] Indeed, proteins, enzymes, DNA, and oligonucleotides have all been immobilized on AuNPs; the physicochemical characteristics of these functionalized AuNPs have been investigated in a variety of academic studies.[64–74,94] Several techniques have been used to immobilize enzymes on variety nanostructures in attempts to improve the enzymatic activity and stability.[71–76,95,96]

In previous reports, catalytic activity of enzyme-functionalized AuNPs has been investigated with the surface modification of linkers.[89,95,97] However, most of these kinetic investigations need steps such as modified biomolecules onto the AuNPs surface and separating the modified AuNPs from the unmodified AuNPs or surplus molecules. These steps, firstly, led to complication and relatively high cost of the experiments. In addition, long-time course (covalent bond) also led to activation lost of enzyme. What's more, the target binding sites and conformational changes of the

enzyme after binding were not all known precisely, so labeling sites were not only difficult to design, but also could weaken the affinity between the reactant and the enzyme. Although some enzyme-functionalized AuNPs with modified linkers exhibit enhanced catalytic activity, which has been supposed to favorable conformational changes and electrostatic interactions,[71–74] there have been no detailed studies aimed at quantifying the differences between the rate constants of AuNP-immobilized and free enzymes. Therefore, developing linker-free AuNPs kinetic assays to simplify the detection process would be important and attractive. To gain insight into the mechanisms of enzyme reaction in the presence of functionalized AuNPs, we have to perform suitable analytical methods and obtain kinetic data for the explanation of the catalytic behaviors. In this work, we have systematically investigated the interactions between the nanoparticle monolayer and the affected substrates by quantifying the kinetic parameters to understand the enhanced catalytic action of the enzyme-functionalized AuNPs without modified linkers (See Figure 4.1). We think that such fundamental research will be beneficial for the development of new nanobiotechnological applications.

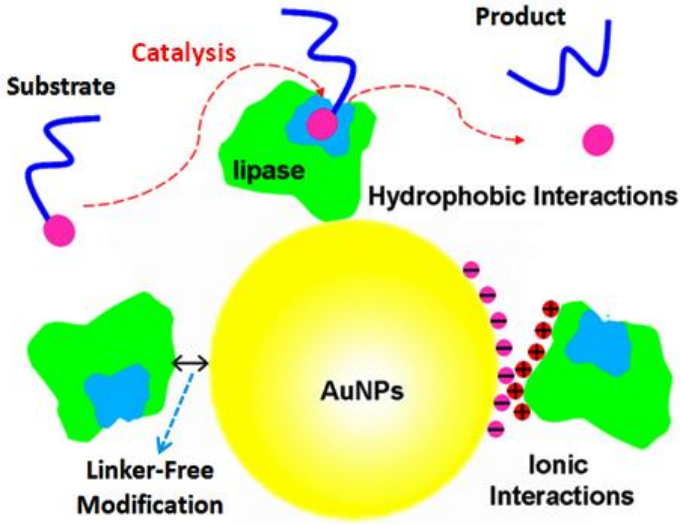

Figure 4.1 Schematic representation of the mechanism of catalysis of enzyme-functionalized AuNPs. Color scheme: AuNPs, gold; enzyme, green; first product, pink; second product, blue.

4.2 Results and Discussion

4.2.1 Mechanism of the Catalytic Reaction by the AuNP-Bound Lipase

Lipases are used industrially as detergent enzymes, in paper and food technology, in the preparation of specialty fats, and as biocatalysts for the synthesis of organic intermediates, and in various clinical studies and drug delivery. The kinetic model of lipases is based on the so-called ping–pong mechanism, which also applies to many other enzymes, such as glucose oxidase, horseradish peroxidase, and alkaline phosphatase.[77] As a representative esterase, lipase is an excellent model for studying the enhanced activity of the AuNPs-bound enzymes because of its well-defined structure, properties, and applications.

A linker-free AuNP-bound lipase was developed to study the kinetics of the immobilized enzyme. Our kinetic and structural studies led us to propose the mechanism depicted in Figure 4.2. There are four independent rate constants (k_1, k_2, k_3, and k_4) in this system.[98] Initially, the substrate (S) is bound to the active site of the enzyme (E) with a rate constant k_1, forming an intermediate complex (ES). Passing through the transition state, the ES complex is converted into the acyl enzyme (E^*) with a rate constant k_3, releasing the product (P), in this case *p*NP. The acyl bond is then cleaved, with a rate constant k_4, upon nucleophilic attack, returning the enzyme to its initial state.

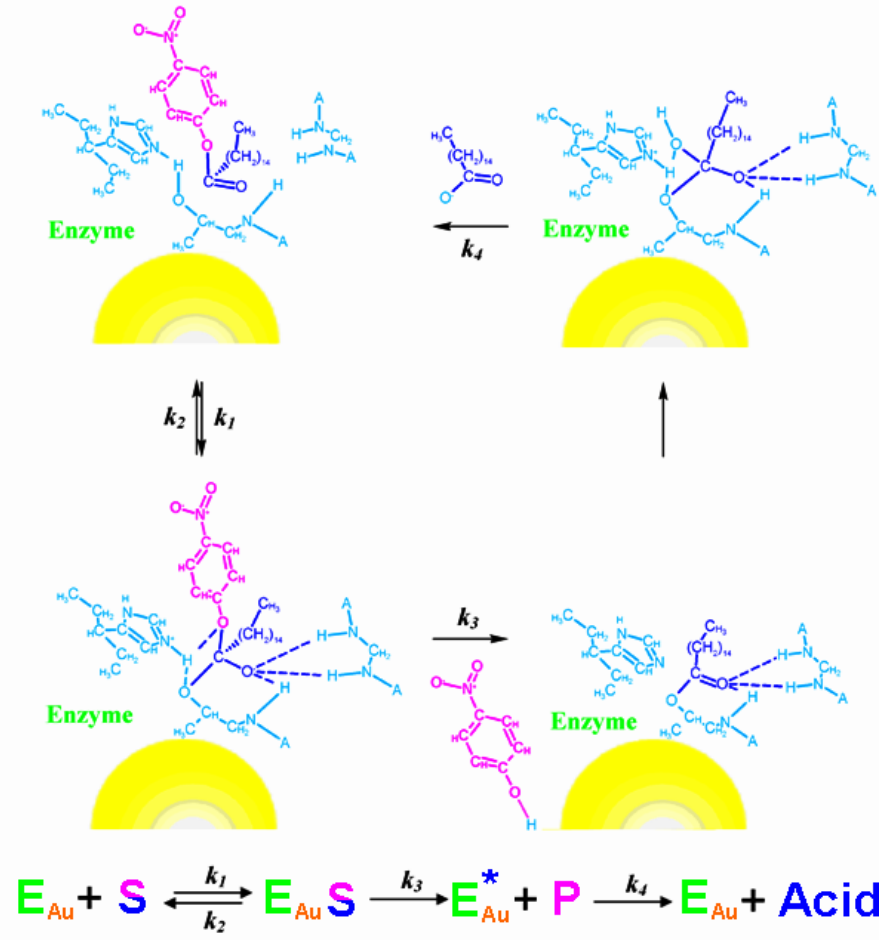

Figure 4.2 Mechanism of the catalytic reaction mediated by the enzyme-functionalized AuNPs.

$[E_0]$ is the total enzyme concentration; the kinetic parameters k_{cat} (turnover number), K_m (apparent dissociation constant), and k_{cat}/K_m (apparent specificity constant) are defined as follows:

$$k_{cat} = \frac{k_3 k_4}{k_3 + k_4}$$

$$K_m = \frac{k_2 + k_3}{k_1} \frac{k_4}{k_3 + k_4}$$

$$\frac{k_{cat}}{K_m} = \frac{k_1 k_3}{k_2 + k_3}$$

The rate constants in Figure 4.2 are related to the experimental values of K_m and k_{cat} through the following equations:

$$v = \frac{k_{cat}[E_0][S]}{K_m + [S]}$$

$$V_{max} = k_{cat}[E_0]$$

The value of K_m for the kinetic studies represents the affinity of the enzyme toward the substrate; the rate-limiting step (k_{cat}), which occurred prior to formation of the acyl enzyme intermediate, was determined by monitoring the product's release.[99]

4.2.2 Observation of AuNPs on Silicon Wafer

The SEM image was recorded using a JEOL JSM-6700F electron microscope operated at 20 kV. The sample for SEM analysis was prepared by placing a few drops of the AuNPs solution onto a silicon wafer modified with the MPTMS linker as described in Section 3.3.2 (page 37 and 38). The sample was rinsed with DI water for 10 min and then dried prior to viewing under the electron microscope. Figure 4.3a showed that the AuNPs were immobilized perfectly on the silicon oxide surface. The uniformity and the size distribution of AuNPs were both great. The average size of AuNPs was 13 ± 1 nm. Figure 4.3b was analyzed by the software named Image-Pro Plus (IPP), and the analysis region was the full SEM image.

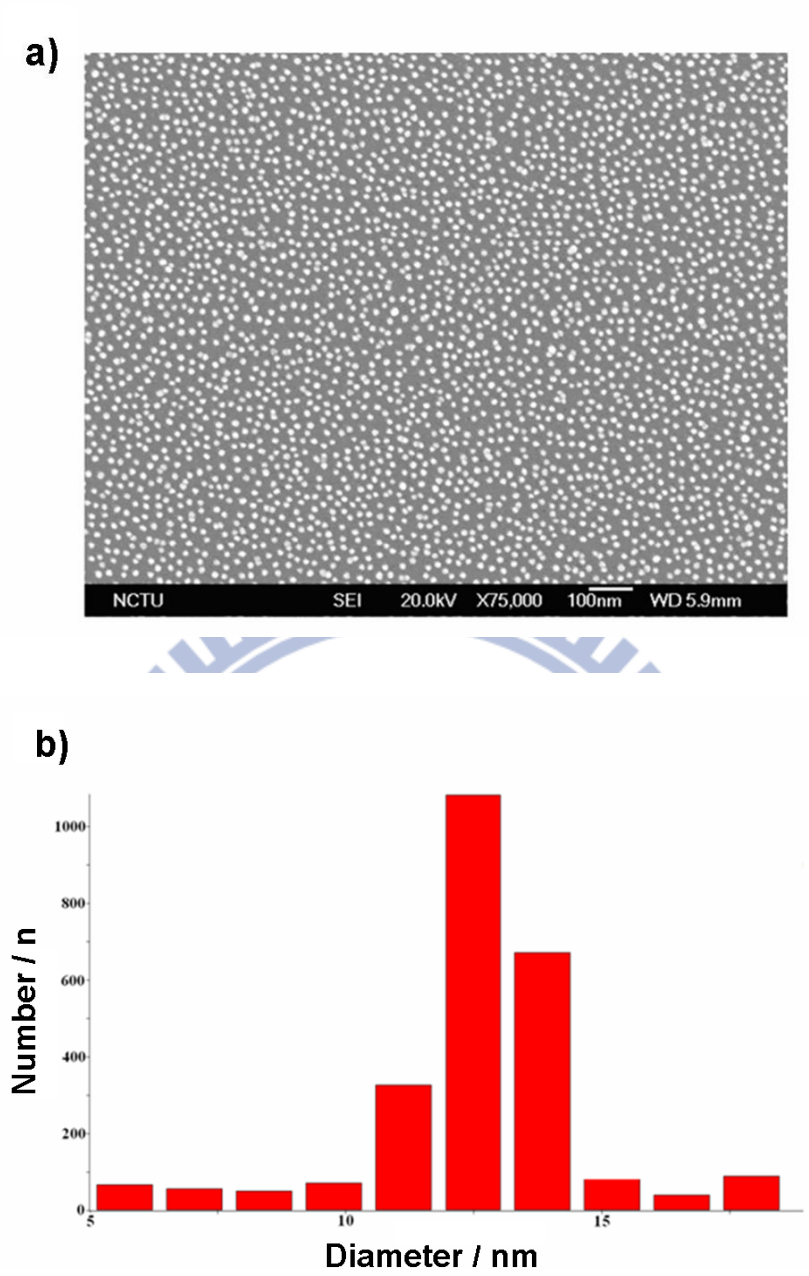

Figure 4.3 a) SEM image of AuNPs immobilized onto a silicon dioxide surface through an MPTMS linker. b) Particle size distribution of the AuNPs present in the SEM image, analyzed using a personal computer and Image-Pro Plus software.

4.2.3 Determining the Immobilization of Enzyme Capped AuNPs on Silicon Wafer

In this experiment, we dropped a few drops of the lipase solution onto a silicon wafer modified with the AuNPs (See Figure 4.4). Then, we washed the wafer with DI water and followed by nitrogen purge. Next, self-assembled monolayers (SAMs) of enzyme-functionalized AuNPs onto silicon wafer were characterized by X-ray photoelectron spectroscopy (XPS; VG Scientific Microlab F310) and fourier transform infrared spectroscopy (FTIR) spectra.

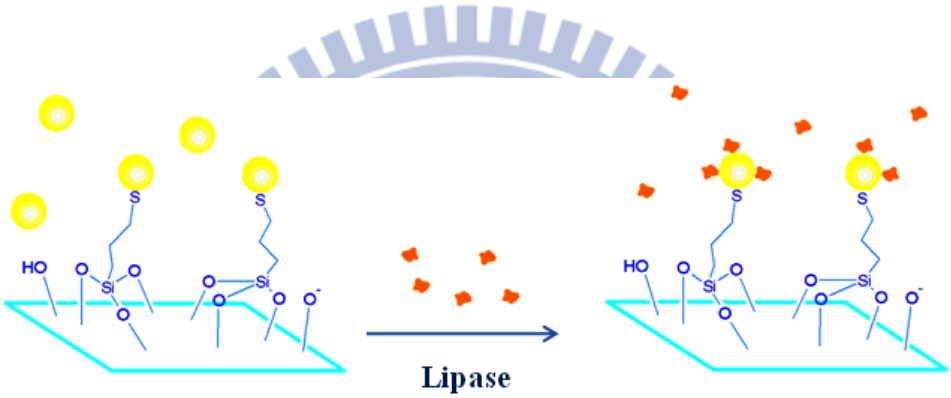

Figure 4.4 Self-assembly steps for enzyme-functionalized capped gold nanoparticles onto silicon oxide surface.

The XPS was used to verify the attachment of the enzymes onto the surfaces of the AuNPs. For the AuNPs modified with lipase, the marked peak indicates the presence of NH_2 groups (N_{1s} binding energy = 399.6 eV)[100] under X-ray irradiation initiated by the photoelectrons and secondary electrons emitted from the surface (See Figure 4.5). The result is in agreement with the existing literature for proteins and enzymes bound to the surface of AuNPs without surface modification. The FTIR was also used to verify the attachment of proteins on the surface of the AuNPs. For AuNPs modified with lipase, the peaks at 1550 cm^{-1} indicate the presence of the primary amine on the nanoparticles surface[101] (As shown in Figure 4.6). Broad band 3300 cm^{-1} was an indication of the bonded NH or NH_2 groups on the surface. These data

suggested that the surface of the gold nanoparticles was modified by nonspecific adsorption of proteins. The addition of a protein to gold colloid resulted in spontaneous adsorption on the surface of the NPs as a result of electrostatic, hydrophobic, and van der Waals interactions.

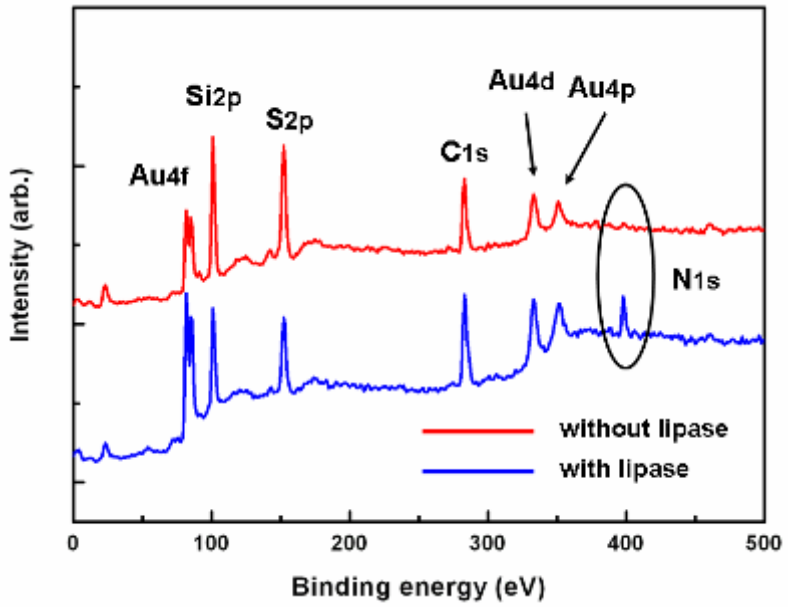

Figure 4.5 XPS spectra of AuNPs measured in the presence (blue) and absence (red) of the enzyme on the silicon dioxide surface.

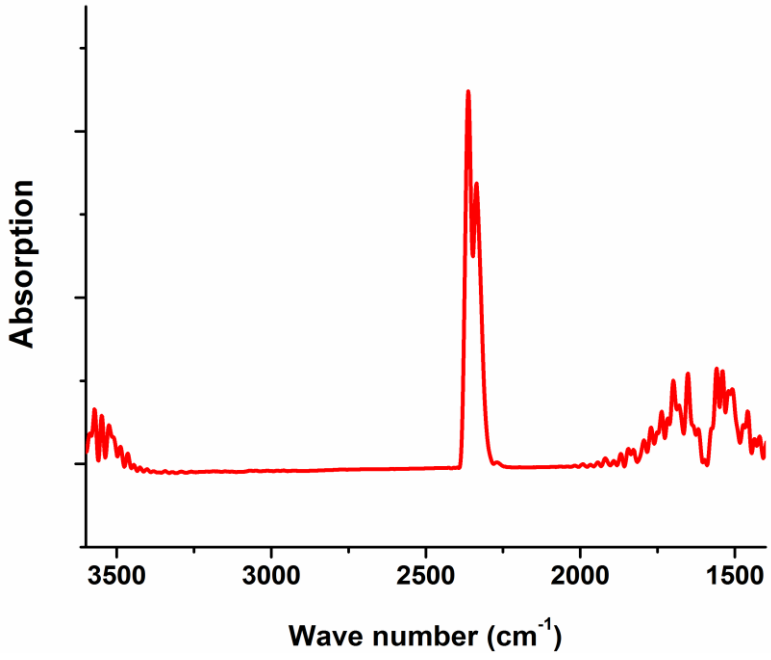

Figure 4.6 FTIR spectra of enzyme capped gold nanoparticles on the silicon wafer.

4.2.4 Determining the Enzyme Coverage of AuNPs with Lipase

As for any conjugation procedure, determining the enzyme coverage on the surface of the AuNPs and the optimal ratio of AuNPs to enzyme are important for activity assays. There is a simple method to discriminate between the aggregated and the nonaggregated AuNPs in aqueous solution, based on distinguishable color changes from red to blue upon aggregation.[2] As shown in Figure 4.7a, the UV–Vis absorption spectrum of the AuNP solution (black trace) exhibited a strong surface plasmon resonance (SPR) at ca. 520 nm; adsorption of the enzyme onto the AuNPs caused a slight shift (green trace) in the SPR peak; previous studies showed proteins adsorbed onto AuNPs could cause similar shifts in the SPR.[102] The gold colloids aggregated at a high concentration of electrolytes (salt) in the absence of a protecting coating layer (red trace; without enzyme). After adding salt solution (NaCl) to the enzyme-capped AuNPs, the absorption signal remained sharp (blue trace) and the solution retained the color of the enzyme-capped AuNPs (See Figure 4.7b).

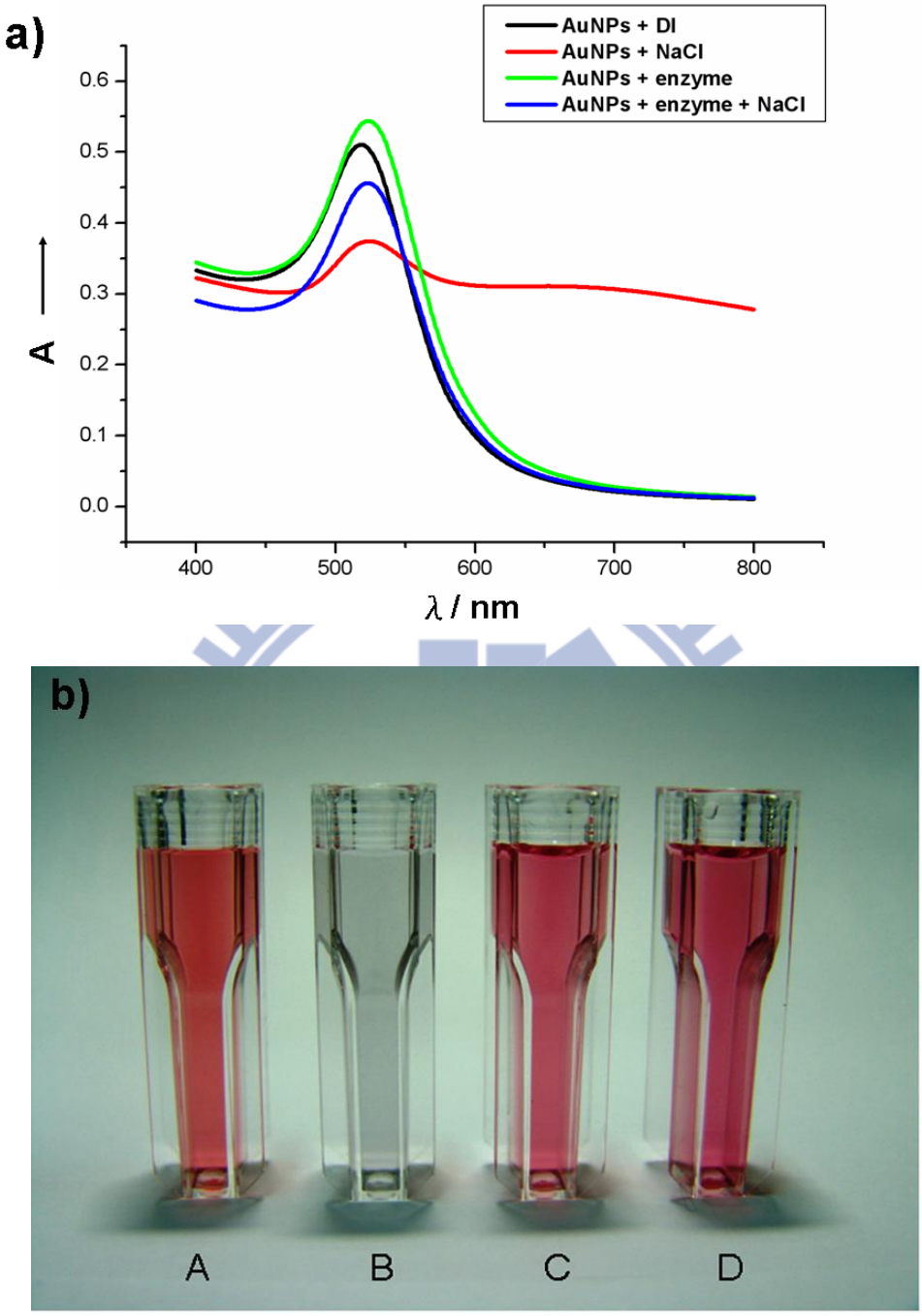

Figure 4.7 a) Determining the degree of enzyme immobilization on non-aggregated AuNPs. UV–Vis absorption spectra of AuNPs in DI water (black), AuNPs in NaCl solution (red), enzyme-capped AuNPs in DI water (green), and enzyme-capped AuNPs after adding NaCl solution (blue). b) Photographic image of solutions of (A) AuNPs in DI water, (B) AuNPs in NaCl solution, (C) AuNPs capped with lipase in DI water, and (D) AuNP-bound lipase in DI water after adding NaCl solution. The variation in color allowed discrimination between the aggregated and non-aggregated AuNPs in aqueous solution; i.e., a distinguishable color change from red (A, C, and D) to blue (B) occurred upon aggregation.

As shown in Figure 4.8, by exploiting interactions between the AuNPs and lipase, color changes of the AuNPs could sensitively differentiate the concentration used of enzyme after titrating with the salt solution. We monitored the stability of the AuNPs solution by its color or by the absorbance spectra. If the enzyme did not cap the gold nanoparticles completely, we obtained spectra exhibiting aggregation of AuNPs. As long as the colloid continued to turn blue, and thus formed gold aggregates, with addition of electrolyte, the amount of enzyme added is not sufficient to stabilize the suspension (A, B, C, and D traces). When the concentration of enzyme added was enough to stabilize the colloid, the solution no longer changed color and the absorbance spectra exhibited a strong surface plasmon resonance (SPR) at ca. 520 nm (E and F traces).[101,103]

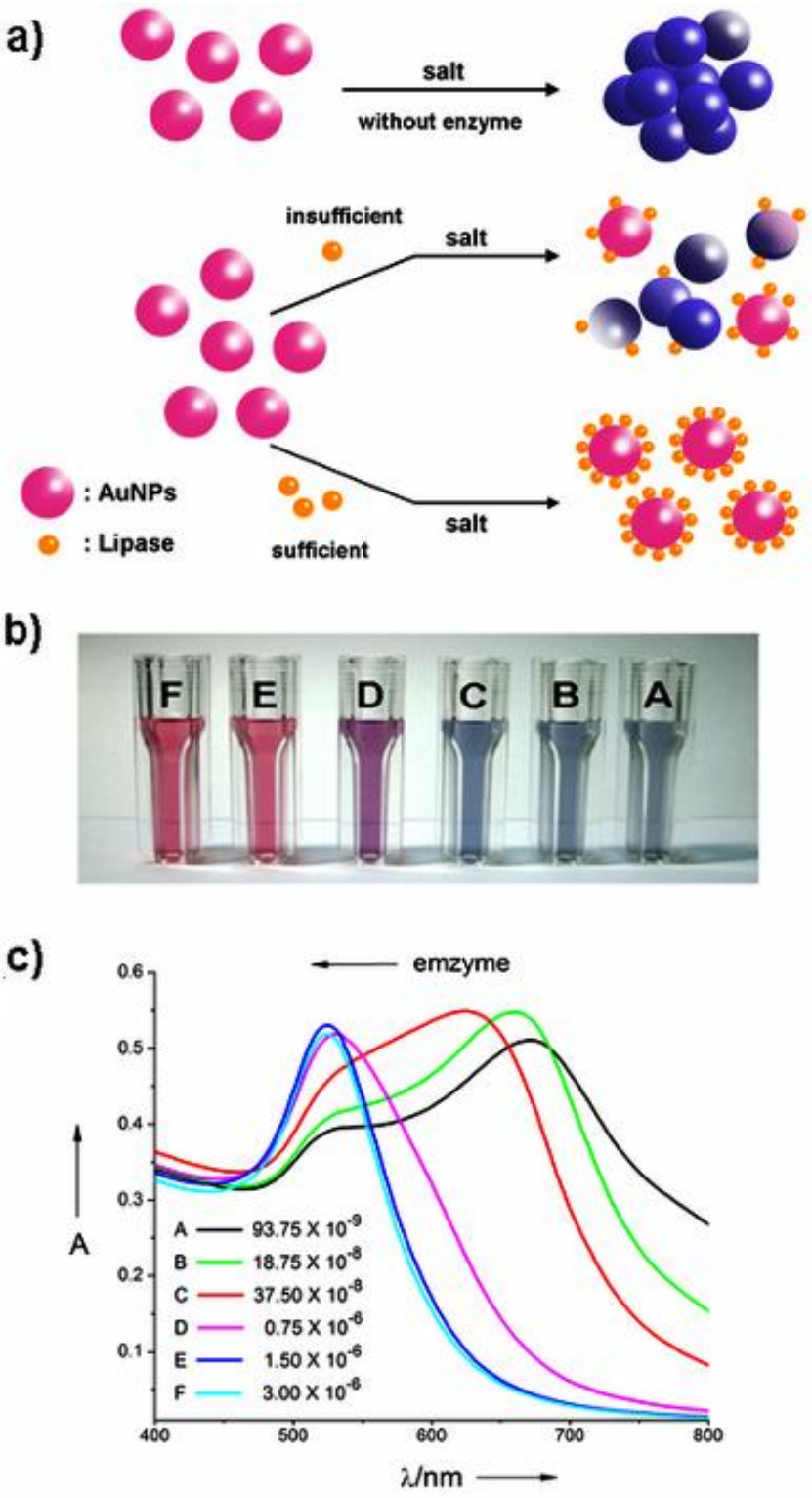

Figure 4.8 a) The diagram of determining the optimal immobilization of lipase-functionalized on gold nanoparticles. Variation in b) photographic image and c) UV–Vis absorbance spectra of the AuNPs (2.2 nM) at different concentrations of enzyme after adding NaCl solution.

As shown in Figure 4.9, once the salt was added, the time-dependent absorption ratio (A620/A520) values of solutions with insufficient enzyme displayed an increasing, which illustrated that the AuNPs/lipase system gradually lost the stability protected by enzyme. On the other hand, the sufficient enzyme could stabilize the gold nanoparticles in the presence of a given high concentration of salt. The destabilization trend was directly related to the amount of lipase present in this assay; that is, the absorbance ratio of the AuNP solutions increased in the presence of lesser amounts of enzyme, revealing that the system of suspended AuNPs gradually lost its stability without protection by lipase. We just made use of this property to determine the coverage of the particles with the enzyme and the optimal ratio of AuNPs to enzyme.[104,105]

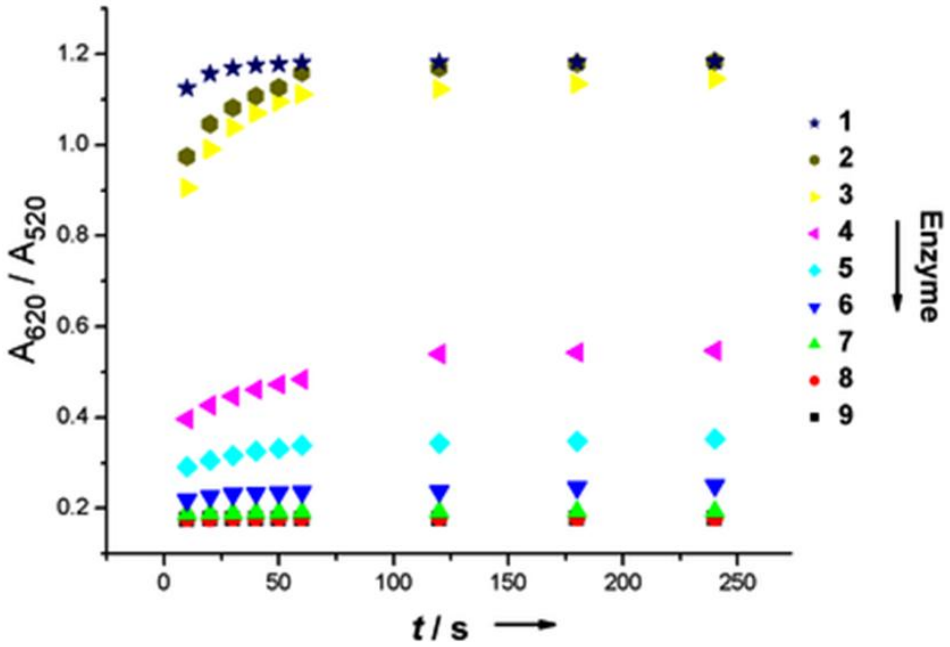

Figure 4.9 Plots of changes in the time-dependent absorption ratio (A620/A520) in the presence of varying concentration of lipase 1) 93.75 x 10^{-9} M, 2) 18.75 x 10^{-8} M, 3) 22.5 x 10^{-8} M, 4) 30 x 10^{-8} M, 5) 37.5 x 10^{-8} M, 6) 0.45 x 10^{-6} M, 7) 0.75 x 10^{-6} M, 8) 1.5 x 10^{-6} M, 9) 2.4 x 10^{-6} M after the addition of salt solution.

For the determination of enzyme coverage on AuNPs, lipase was added to a solution of 13 ± 1 nm AuNPs. After the addition of salt solution, we displayed the plots of changes in the time-dependent absorption ratio (A620/A520) in the presence of varying concentration of lipase. Figure 4.10 displayed a plot for the reciprocal of the ratio of 1.3 mL AuNPs stabilized by the different lipase concentrations after the addition of salt (0.1 mL 10% NaCl solution). When the concentration of lipase added was enough to provide the stability protected for the AuNPs/lipase system, the value of ratio kept constant with time and was almost the same as the nonaggregated AuNPs. On the contrary, there was a significant decrease in the value of ratio with addition of insufficient enzyme. This result suggested that the coverage of the AuNPs can be defined by the ratio which was dependent on the concentration of lipase.

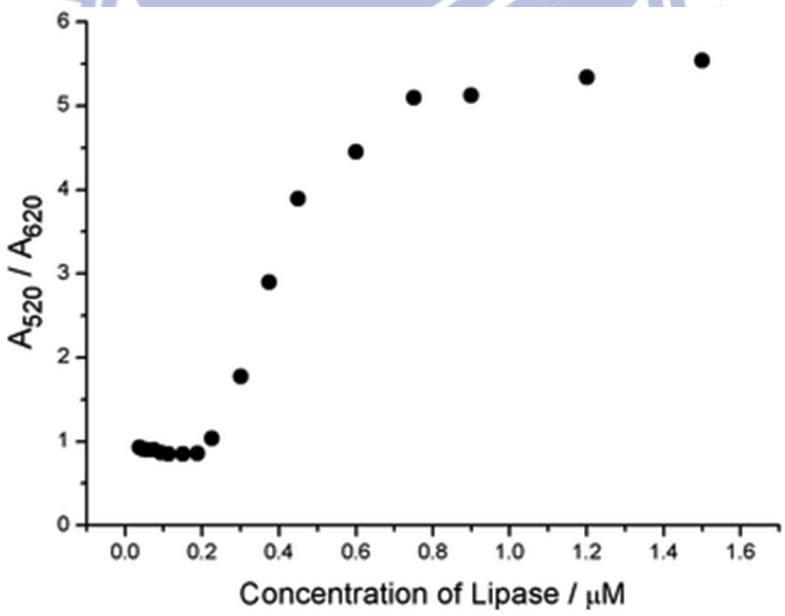

Figure 4.10 Plot of the absorption ratio (A520/A620) in equilibrium *versus* the lipase concentration.

In an enzyme–NP conjugated system, the association between the binding sites of the NP and the enzyme can be described using the simple equilibrium expression:

$$P + E \rightarrow PE$$

The reaction is characterized by an equilibrium constant, K_a:

$$K_a = \frac{[PE]}{[P][E]}$$

where

P: binding site of NP;

E: enzyme;

PE: enzyme–NP binding;

K_a: association constant;

K_d: dissociation constant;

Therefore, $K_d = 1/K_a$

We define Y to be the fractional occupancy of the AuNPs binding sites:

$$Y = \frac{\text{binding sites occupied}}{\text{total binding sites}} = \frac{[PE]}{[PE] + [P]} = \frac{[E]}{[E] + K_d}$$

At Y = 0.5 (50% coverage), $K_d = [E] = 0.37$ μM.

Y *versus* the concentration of enzyme [E] = enzyme dissociation curve:

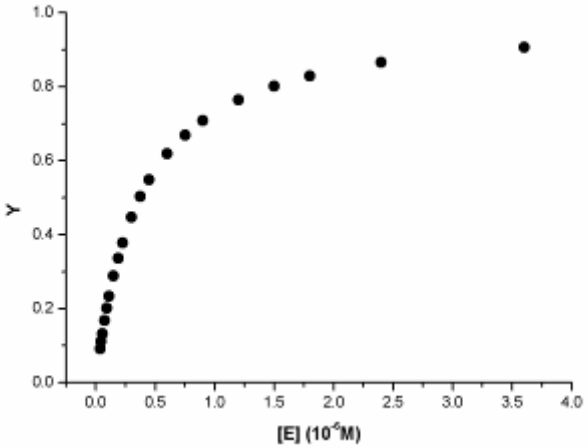

Therefore, the degree of coverage can be determined as this hyperbolic curve. According to the observation, we obtained the dissociation constant K_d and the concentration of lipase that we used for kinetic assays can be up to 80% coverage of enzyme onto the AuNPs. The concentration of enzyme [E] that we prepared for kinetic assays is 1.5 μM.

We used the system of the direct binding onto AuNPs without surface modification for avoiding the congregation issue and determining the enzyme coverage. This linker-free approach has not been reported previously. The formation of lipase–AuNP conjugates has been optimized with regard to its colloidal stability and retention of activity for the purpose of activity assays.

4.2.5 Activity Assays of the Free and AuNPs-Bound Lipase

In the activity assays, we dissolve *p*-nitrophenyl palmitate (*p*NPP) in isopropyl alcohol solution, and then mix the reactants in reaction buffer. We measured the activities of the free and immobilized enzymes by monitoring (at 405 nm; Figure 4.11a) the initial velocity of *p*-nitrophenol (*p*NP) production from *p*-nitrophenyl palmitate (*p*NPP) at various concentrations of the enzyme solutions in l-cm-pathlength cuvettes and the changes in absorbance were recorded as a function of the reaction time. In Figure 4.11b, we observed that the initial release of *p*NP was proportional to the concentrations of both the free and bound enzymes—with a significant increase in the catalytic activity of the enzyme-capped AuNPs. According to the enzyme kinetics equations, an enzyme assay must be designed so that the observed activity is directly proportional to the enzyme concentration; our results suggested that this catalytic assay and analytical method obeyed the basic rule.

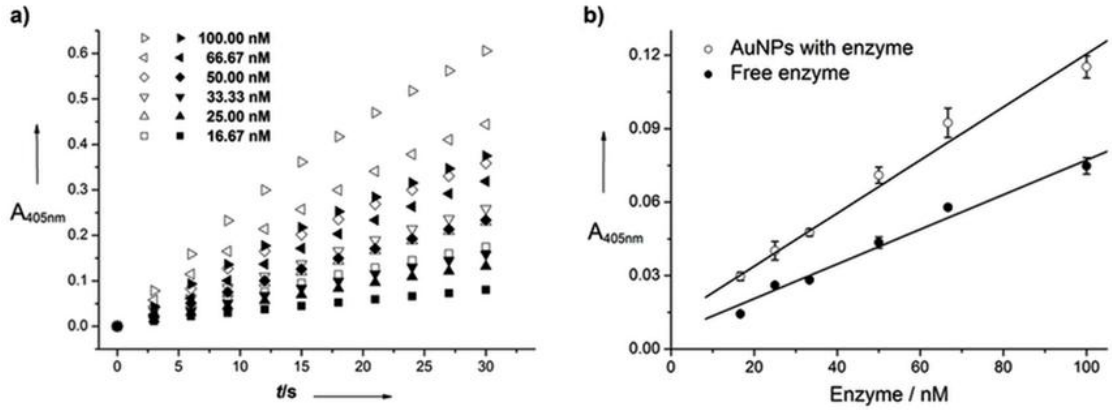

Figure 4.11 a) Product (*p*NP) formation over time in the catalytic reactions of various concentrations of AuNP-bound (solid) and free lipase (hollow) solutions monitored at 405 nm. b) Initial velocities of *p*NP from *p*NPP plotted as a function of the concentration of the free enzyme (●) and the enzyme-capped AuNPs (○).

4.2.6 Effect of AuNPs Concentration on Catalytic Activity

To optimize the supreme efficiency of enhanced catalytic activity, the ratios of AuNPs to enzyme were studies under fixed enzyme and substrate concentration. Figure 4.12 showed the quantitative relationship between the production rate change at 405 nm and the different concentrations of gold nanoparticles. The non-aggregated enzyme–AuNP complex mixed with assay buffer showed an increase in the absorbance. Moreover, the largest change in reaction rate, which was regarded as optimal condition from dispersed to fully aggregated nanoparticles, was observed when the concentration of AuNPs was approximately 2.2 nM in common with condition E in Figure 4.8c. It is noted that there was a significant increase in the rate of production with addition of AuNPs as compared to the control reaction with no AuNPs. Each increase in concentration of 25% resulted in an increase in reaction rate by about 0.14 μM s^{-1}, thereby demonstrating the ability of the AuNPs to act as a factor for enhancing activity. Over optimal condition, reaction rate decreased because the redundant AuNPs aggregated without sufficient coverage, and this phenomenon can be confirmed by the shifted peak of the absorbance spectra. Therefore, it was estimated that catalytic activity can be manipulated by the ratios of AuNPs to enzyme.

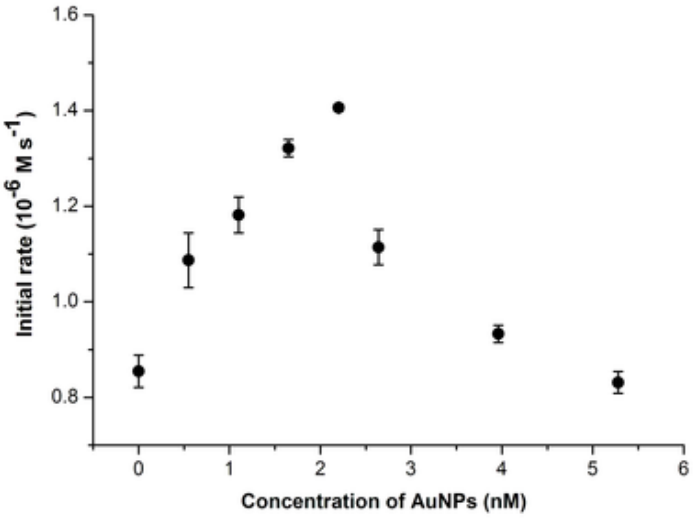

Figure 4.12 Initial rate of *p*NP production *versus* the concentration of AuNPs. Conditions : pH 7.4, 30℃, [enzyme] = 100 nM, [substrate] = 22.22 μM.

Since the surface modification of linkers protected the AuNPs from aggregation, it would be perplexed to determine the enzyme coverage and the optimal ratio of AuNPs to enzyme because less or much enzyme cannot be identified by salt titration. In our system, we use the same concentration of enzyme in the compared systems for ensuring that accurate parameters presented and then we can understand the mechanism of enhanced catalytic activity. However, we used this system (linker-free) of the direct binding onto AuNPs without surface modification for avoiding the congregation and determining the enzyme coverage with minimum unbound enzyme, allowing us to perform accurate analyses of the kinetics.

4.2.7 Kinetic and Thermodynamic Investigations of Enzyme-Functionalized AuNPs

We designed an accurate analysis of enzyme kinetics in order to understand the property of the significantly enhanced activity for enzyme-functionalized gold nanoparticles. Figure 4.13 displays Michaelis–Menten plots for the hydrolysis of *p*NPP (5.55–133.33 μM) by the free enzyme and enzyme-capped AuNPs at pH 7.4 and 30℃. The value of the maximum velocity (V_{max}) was the same in the absence and presence of the AuNPs, but the Michaelis constant (K_m) was obviously smaller when using the lipase-capped AuNPs. According to the Michaelis–Menten equation, the values of V_{max} can represent the values of k_{cat}, which indicated that the degrees of product formation and release from the active site were identical in both systems when the concentration of the enzyme was the same. Therefore, the value of k_{cat} of the bound enzyme was not significantly different from that of the free enzyme. We infer that the enzymes capped on the AuNPs retained their ability to perform nucleophilic attack *via* the formation of an acyl enzyme; i.e., the presence of the AuNPs had no influence on the release of product in the rate-limiting step. The values of the

Michaelis constant were 23.91 and 9.10 μM ($p < 0.05$) for the free and bound enzymes, respectively. A smaller value of K_m represented a higher affinity of an enzyme toward a substrate; i.e., the presence of the AuNPs enhanced the selectivity of lipase toward the substrate. Because the binding of lipase on the surface of the AuNPs affected only the value of K_m, the addition of the AuNPs was an efficacious means of tuning the enzyme–substrate association. The active site of an enzyme not only recognizes the substrate(s) to create an intermediate complex (ES) but also complemented and stabilized the transition state. The higher affinity of the substrate toward the enzyme-bound AuNPs resulted in a lower-energy transition state; indeed, the linear Arrhenius plots for the hydrolyses of *p*NPP mediated by the AuNP-bound and free enzymes at 25–50℃ (Figure 4.14) provided activation energies of 5.9 and 12.2 kJ mol^{-1}, respectively. Thus, the enzymes immobilized onto the surfaces of the AuNPs exhibited higher catalytic activity through more ready formation of the ES complex and reduction of the activation energy.

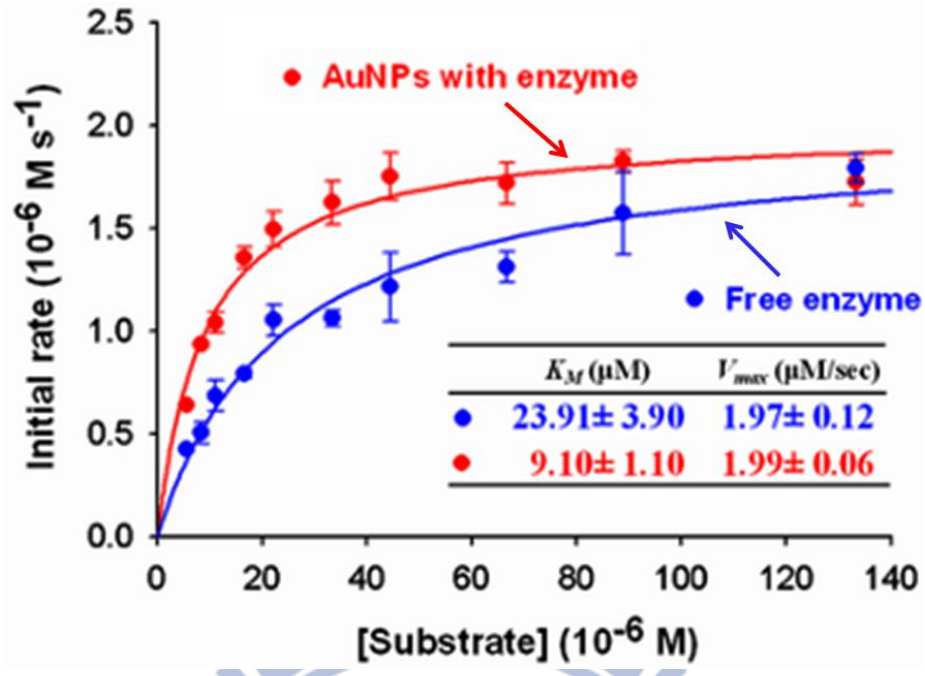

Figure 4.13 Michaelis–Menten plots for the hydrolyses of *p*NPP mediated by the free enzyme (blue) and enzyme-capped AuNPs (red).

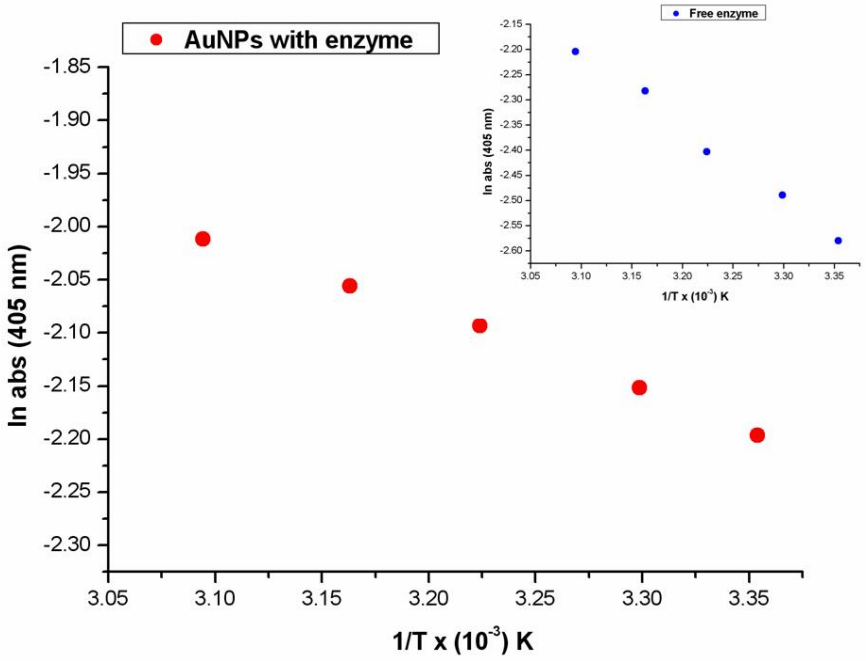

Figure 4.14 Arrhenius plots of ln(absorbance) *versus* the reciprocal of absolute temperature for the free (blue, inset) and AuNP-bound (red) lipase. The activity was measured for reaction mixtures containing 0.1 μM enzyme at pH 7.4.

4.3 Conclusions

In summary, we have investigated the kinetics of the significantly enhanced activity in the presence of enzyme-functionalized AuNPs. The immobilization of lipase onto the nanoparticles' surfaces, without any surface modification, provided colloidal stability that allowed us to determine the enzyme coverage on the surface of particles. Our analytical methodology involved defining the dissociation constant with respect to the appropriate conditions for conjugation; the lipase bound to the surface of NPs may lead to the formation of functionalized AuNPs under retention of enzymatic activity. Additionally, the efficiency of enhanced catalytic activity with colloidal stability has been optimized by regularizing the ratios of AuNPs to enzyme. The lipase capping the AuNPs catalyzed the hydrolysis of *p*NPP through the same kinetic model as that of the free enzyme, with the product's release being the rate-limiting step (k_{cat}), but with increased catalytic activity, as evidenced by lower values of the activation energy and K_m. We ascribe this behavior to the enhanced substrate selectivity of the enzyme–AuNPs complex, thereby decreasing the activation energy through enhancing the rate constants leading to the formation of the ES complex. In biological systems, regulation of enzyme activity plays a central role in governing cell behavior.[106] Our findings suggest that the ability of AuNPs to manipulate catalytic activity might become an important nanobiotechnological tool for optimizing clinical studies and improving drug delivery in the future.

Chapter 5: Size-Modulated Catalytic Activity of Enzyme–Nanoparticle Conjugates: A Combined Kinetic and Theoretical Study

5.1 Background

Many biomolecules, such as membrane proteins, perform their specific biorecognition or biocatalytic events while immobilized on the surfaces of cells or organelles.[107,108] Several artificial technologies (e.g., bioconversion, bioremediation, biosensing) also take advantage of immobilized biomolecules and bio-species.[109,110,111] In this regard, the modification and immobilization of enzymes has been studied widely for the generation of biocatalysts exhibiting modulated stability and selectivity.[43,112,113] Several synthetic scaffolds and supports, including gels,[114,115] planar surfaces,[116, 117] carbon nanotubes,[118,119] and nanocomposites,[95] have been used to immobilize enzymes. Among them, nanoparticles (NPs) provide an almost ideal mix of properties—minimum diffusional limitation, maximum surface area, and high effective enzyme loading—to optimize the performance of immobilized enzymes[41,120] while harnessing the fluorescent,[27,92] magnetic,[97,121] and interfacial[76,122] behavior of the resulting nanomaterials.[6,24–26,123]

NPs of various dimensions, compositions, and surface modifications have been studied on their interactions with biomolecules.[26,124,125,126] The main challenge often lies in understanding the interface between biological and non-biological materials on the nano-scale. The development of new tools for the controlled manipulation of such materials is clearly of great importance.[13,14,127] Recently, some research efforts have been conducted to investigate the effects of gold NPs (AuNPs) on the modulation of

enzyme activity through surface interactions.[51,71–74,123] In those studies, enzymes localized at the enhanced surface area exhibited improved activity because of the increased substrate concentration and also because they attained flexible conformations. AuNPs are excellent systems for modeling enzymes' surfaces because they can be readily fabricated on size scales comparable with those of their biomolecular targets. Therefore, we were curious to study whether varying the dimensions of the AuNPs would affect their catalytic reaction behavior—in particular, the effects on the kinetics of their enzyme–NP conjugates.

In the last chapter, we proposed an analytical scheme and demonstrated that adsorbing by means of linker-free assembly of lipase onto AuNPs significantly increased its enzymatic activity. This phenomenon may have great potential for development into a simple method for tuning the rate of enzymatic reactions by varying the conditions for forming enzyme–NP conjugates.[128] In further investigations, we observed that the size of the NPs affected the catalytic activity of this conjugated system; based on a diffusion–collision theory,[129,130] we have attempted to develop a length scale–dependent model to explain the catalytic behavior. In nature, controllable modulation of enzyme activity is a potent means of regulating several cellular processes (e.g., signal transduction, biosynthesis, metabolism);[106] in man-made systems, enhanced or altered enzyme activity finds potential application in a number of enzyme-related technologies: enzyme-coupled biosensing, lab-on-a-chip platforms, hybrid (biotic–abiotic) nanomaterials, and novel enzyme-based devices.[6,24–29,131,132,133] The modulating of biocatalytic behavior is an attractive feature for exploitation in the field of nanobiotechnology. For extended studies of biocatalysis, lipases are very suitable esterases because of their well-defined structures, properties, and applications. Lipases are used industrially in detergents, in paper and food technology, in the preparation of specialty fats, in various clinical studies, and

for drug delivery.[77] Notably, these hydrolytic enzymes are insensitive toward non-aqueous solvents, have a fairly broad tolerance of pH and temperature, and, most importantly, exhibit high chemoselectivity.[95,112] Therefore, in this study we selected *Candida rugosa* lipase (CRL, E.C. 3.1.1.3) to construct our enzyme–NP conjugates.

As illustrated schematically in Figure 5.1, from analysis of the effect of AuNP size on the modulated activity of CRL–AuNP conjugates, we have developed a shielding model that is consistent with the experimental results of kinetic investigation. This size-effect model provides physical meaning and reasonably explains the kinetic response of this enzyme–nanoparticle conjugate system, leading to the observed substrate specificities and catalytic constants. Understanding the fundamental origins of length scale–dependent catalytic behavior is of paramount importance because these properties directly influence the interactions of nanostructures with biological molecules—in particular, in nanoparticle-based platforms for biomolecular surface recognition.

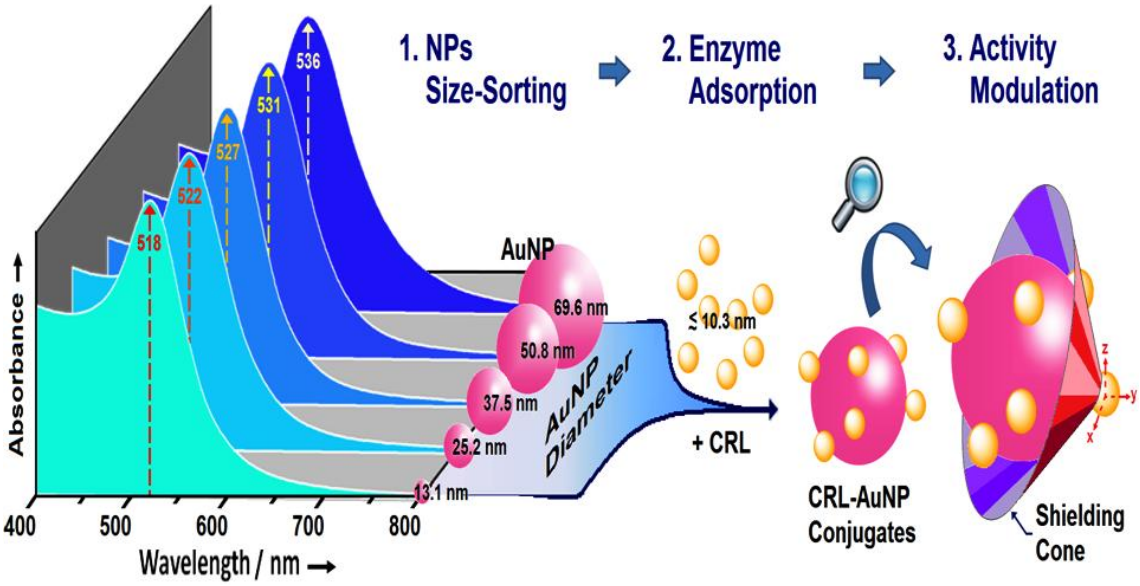

Figure 5.1 Schematic representation of the preparation of CRL–AuNP conjugates that modulate the activity of the enzyme, and a cartoon of the shielding model.

5.2 Results and Discussion

5.2.1 Particle Size Distribution and Mean Diameter of AuNPs

We selected AuNPs as the adsorption materials for enzyme (CRL) in this study because they can be synthesized in a variety of diameters (13–100 nm) and readily characterized using electron microscopy and UV–Vis spectrophotometry. We used the Turkevich/Frens process to synthesize AuNPs because of the aqueous phase reaction for environmental moderate and the ability of controlling AuNPs sizes by using different concentrations of trisodium citrate. In order to obtain differently sized AuNPs, we used five concentrations of trisodium citrate for AuNPs synthesis and the conditions were listed in Table 5.1. These AuNPs were free from aggregation as determined by scanning electron microscopy (SEM) and absorption spectra. Figure 5.2 showed the various AuNPs in UV−Vis absorption spectra. While the concentration of trisodium citrate decreased, the maximum absorbance of wavelength had shifted due to the different sizes of AuNPs. The function of trisodium citrate was not only a reduction but also a stabilized reagent in this reaction. Complete reduction of $HAuCl_4$ could not achieve because citrate ions stabilized AuNPs while the AuNPs formation at high concentration of trisodium citrate. Citrate ions prevented larger particles from formation with the increasing concentration of trisodium citrate. As a result, the smaller diameter of AuNPs was obtained under the higher concentration of trisodium citrate. The maximum absorbance of AuNPs was 518, 522, 527, 531 and 536 nm for the concentration of trisodium citrate from 38.8, 25.9, 16.9, 15.5 and 13.9 mM, respectively.

Table 5.1 Various concentrations of trisodium citrate (1 mL) added to $HAuCl_4$ solution (10 mL) and the maximum absorbance related with the differently sized AuNPs

AuNPs Diameter (nm)	Concentration of Trisodium Citrate (mM)	Maximum Absorbance of Uv−Vis (nm)
13.1	38.8	518
25.2	25.9	522
37.5	16.9	527
50.8	15.5	531
69.6	13.9	536

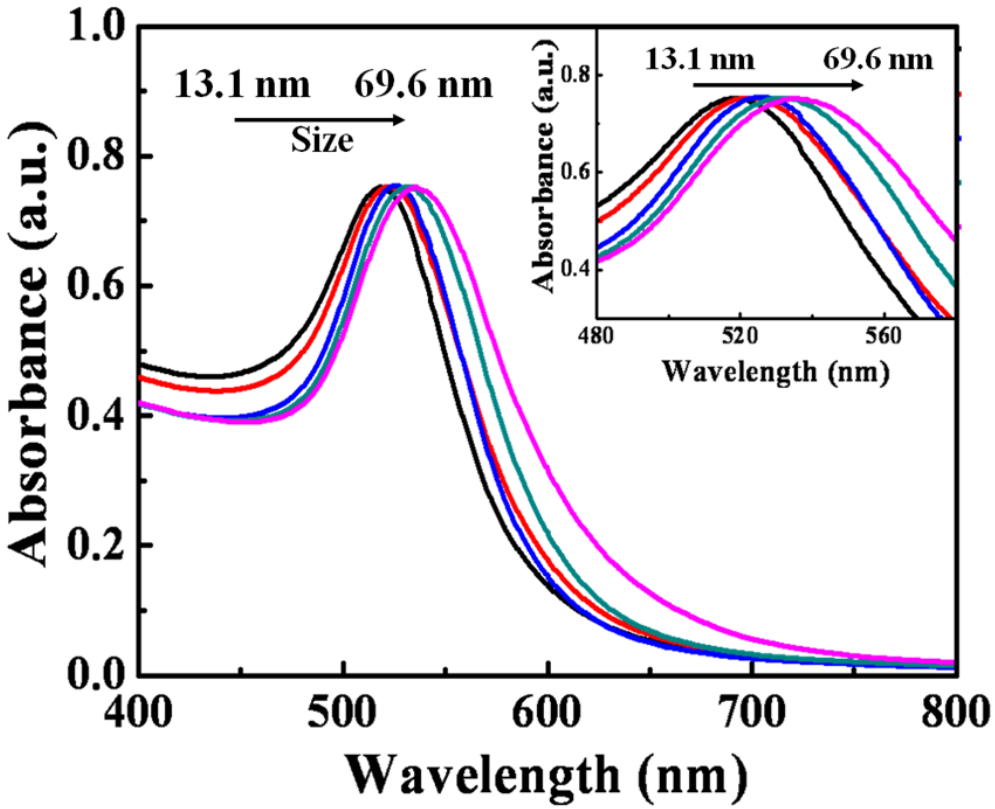

Figure 5.2 UV−Vis spectrum of aqueous AuNPs with the diameters of 13.1, 25.2, 37.5, 50.8 and 69.6 nm.

In Figure 5.3, AuNPs of various sizes were examined by using SEM. These SEM images were recorded using a JEOL JSM-6700F electron microscope operated at 20 kV. The samples were prepared by silicon substrates modified MPTMS which contained thiol group to modify AuNPs efficiently as described in Section 3.3.2 (page 37 and 38). The sample was rinsed with DI water for 10 min and then dried prior to viewing under the electron microscope. The particle size distributions of AuNPs were determined by analyzing the SEM images in Figure 5.3; the results of this analysis with AuNPs having mean diameters of 13.1, 25.2, 37.5, 50.8, and 69.6 nm were displayed in Figure 5.4.

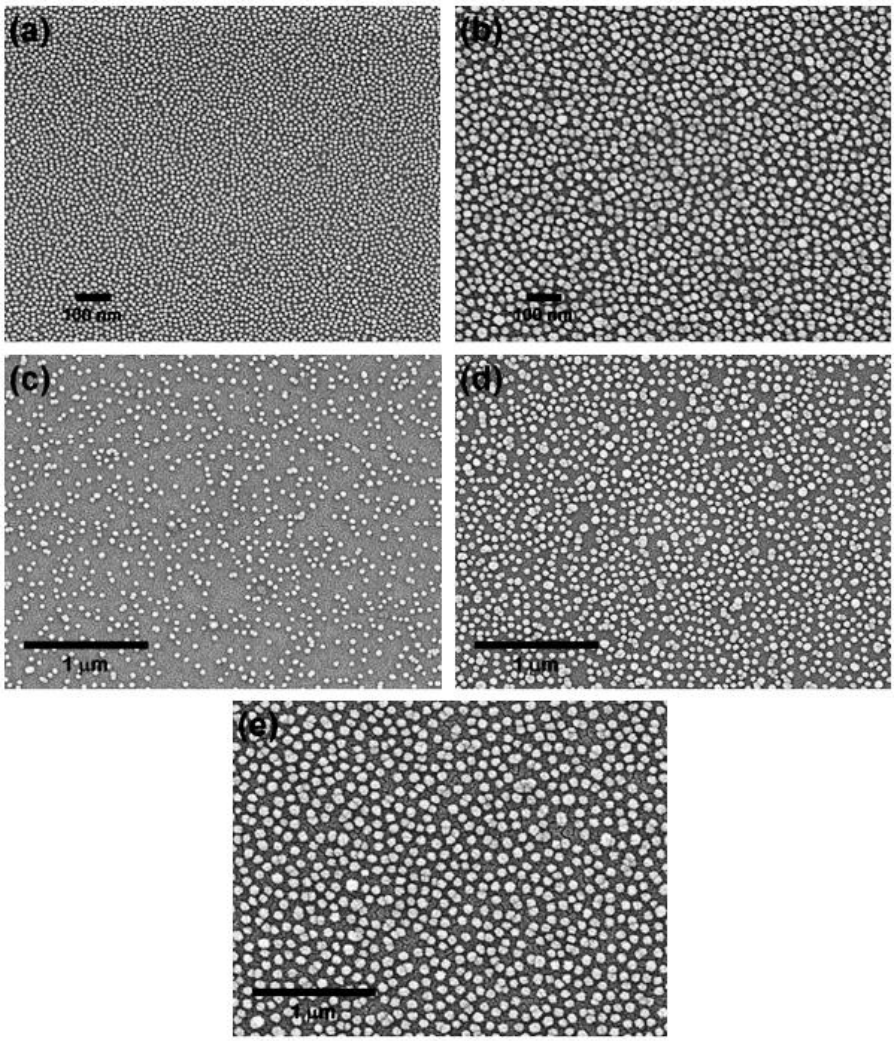

Figure 5.3 SEM images (JEOL JSM-6700F electron microscope operated at 20 kV) of AuNPs with mean diameters of (a) 13.1, (b) 25.2, (c) 37.5, (d) 50.8, and (e) 69.6 nm.

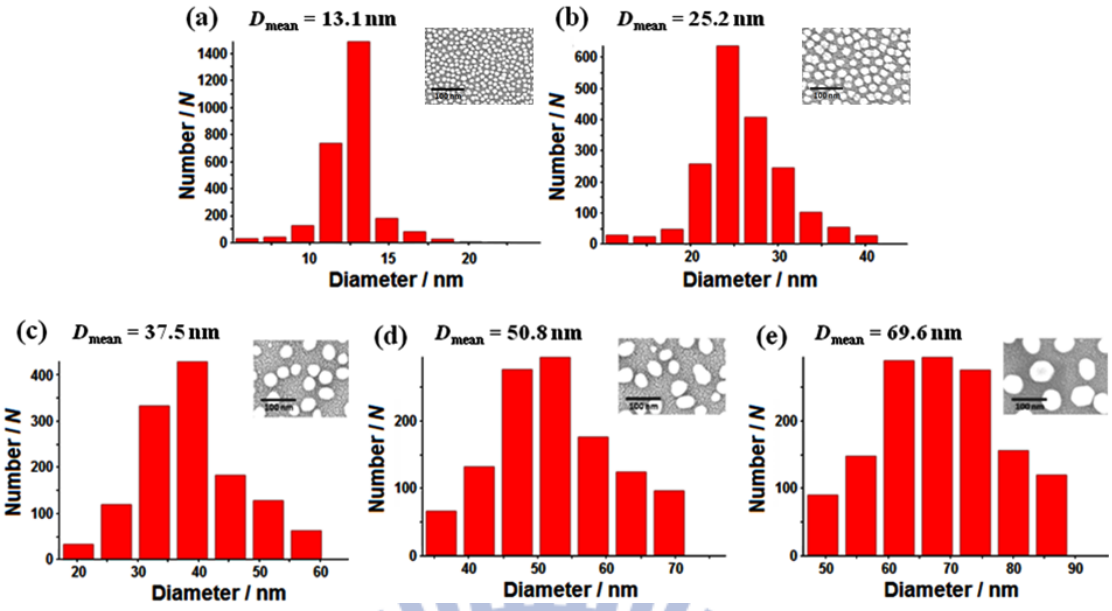

Figure 5.4 SEM images and particle size distributions of AuNPs with mean diameters (D_{mean}) of (a) 13.1, (b) 25.2, (c) 37.5, (d) 50.8, and (e) 69.6 nm. Scale bar: 100 nm.

5.2.2 Apparent Dissociation Constant and Enzyme Coverage—Analysis and Definition

For the preparation of enzyme-functionalized AuNPs with their colloidal stability, we performed the salt-induced colloidal tests to analyze the enzyme coverage and apparent dissociation constants (K^*_d; See Section 4.2.4; page 49–56), determined by measuring the ratios of the absorbance at 620 nm (A_{620}) to those of the absorption signals (A_{peak}) of the differently sized AuNPs; Figure 5.5 displays these progress plots. For the experiment to determine the apparent association constant (K^*_d), various concentrations of CRL were added into the colloidal Au solutions[105] (1.2 OD of each set of AuNPs; the concentrations were 48.67, 9.81, 1.85, 0.74, and 0.29 × 10^{-10} M for AuNPs having mean sizes of 13.1, 25.2, 37.5, 50.8, and 69.6 nm, respectively). After addition of salt solution (0.1 mL of 10% NaCl into 1.2 mL of the sample solution), the changes in the time-dependent absorption ratio (A_{620}/A_{peak}) of the absorbance at 620 nm with respect to the absorption signal of the AuNPs were plotted in the presence of varying concentrations of CRL. As long as the colloid continued to turn blue, and thus

formed salt-induced Au aggregates with a higher ratio (A_{620}/A_{peak}), the amount of enzyme added was insufficient to stabilize the suspension. When the concentration of enzyme added was sufficient to stabilize the colloid, the solution no longer changed color and the ratio remained constant over time.

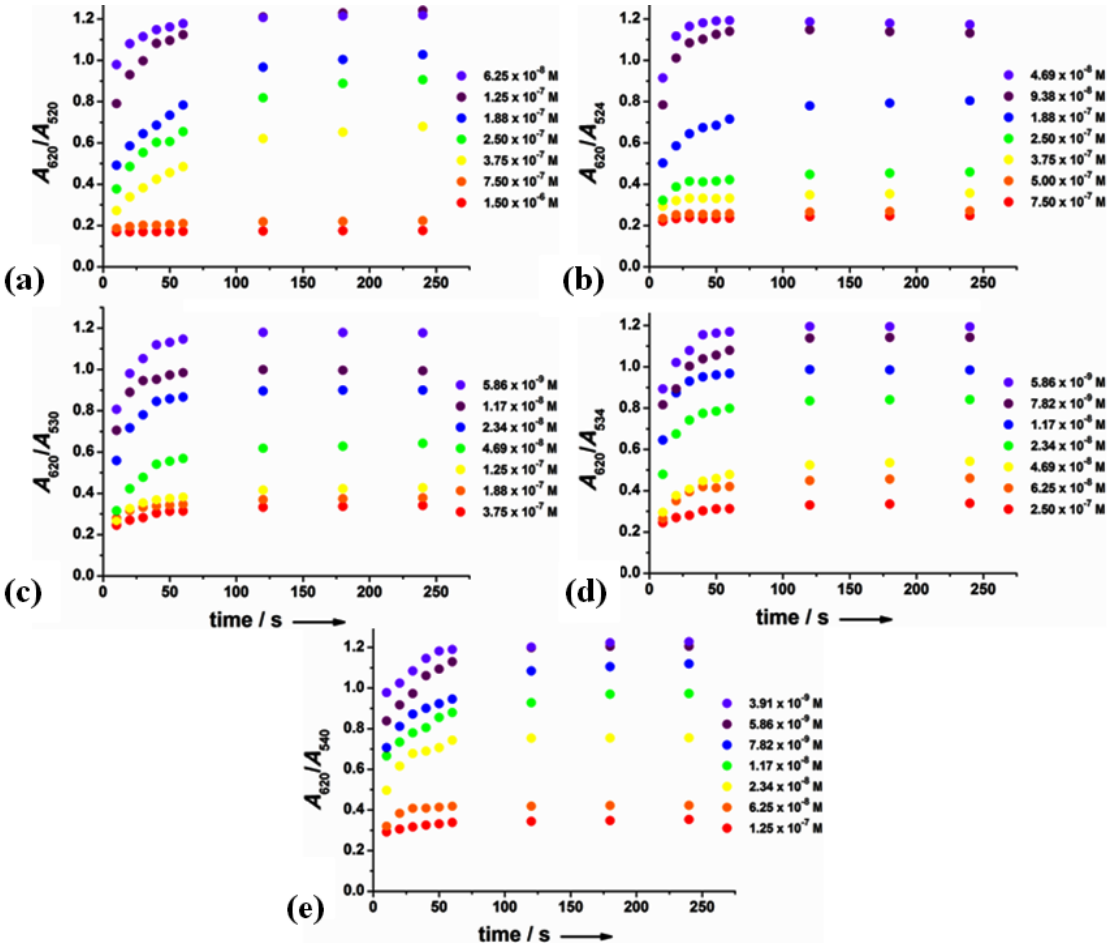

Figure 5.5 Progress curves of the changes in absorption ratios A_{620}/A_{peak}, plotted with respect to time in the presence of various concentrations of CRL, after titrating with salt solution. The values of A_{peak} of the CRL–AuNP conjugates (UV–Vis spectroscopy) incorporating AuNPs having mean diameters of a) 13.1, b) 25.2, c) 37.5, d) 50.8, and e) 69.6 nm were 520, 524, 530, 534, and 540 nm, respectively.

To analyze the enzyme coverage, we define R as the ratio A_{peak}/A_{620}. When the enzyme concentration was sufficient to cap the AuNPs completely, R remained constant over time (i.e., no aggregation). In contrast, significant decreases in R occurred (i.e., aggregation) when the enzyme content was insufficient. We define the coverage as the ratio $(R - R_{min})/(R_{max} - R_{min})$, where R_{max} and R_{min} are the ratios (A_{peak}/A_{620}) in the presence of sufficient enzyme to provide colloidal stability and in the absence of enzyme (i.e., fully aggregated), respectively. Figure 5.6 reveals the quantitative relationship between the percentage coverage of the gold nanoparticles of various sizes and the CRL concentration; the values of K^*_d are determined at 50% coverage.

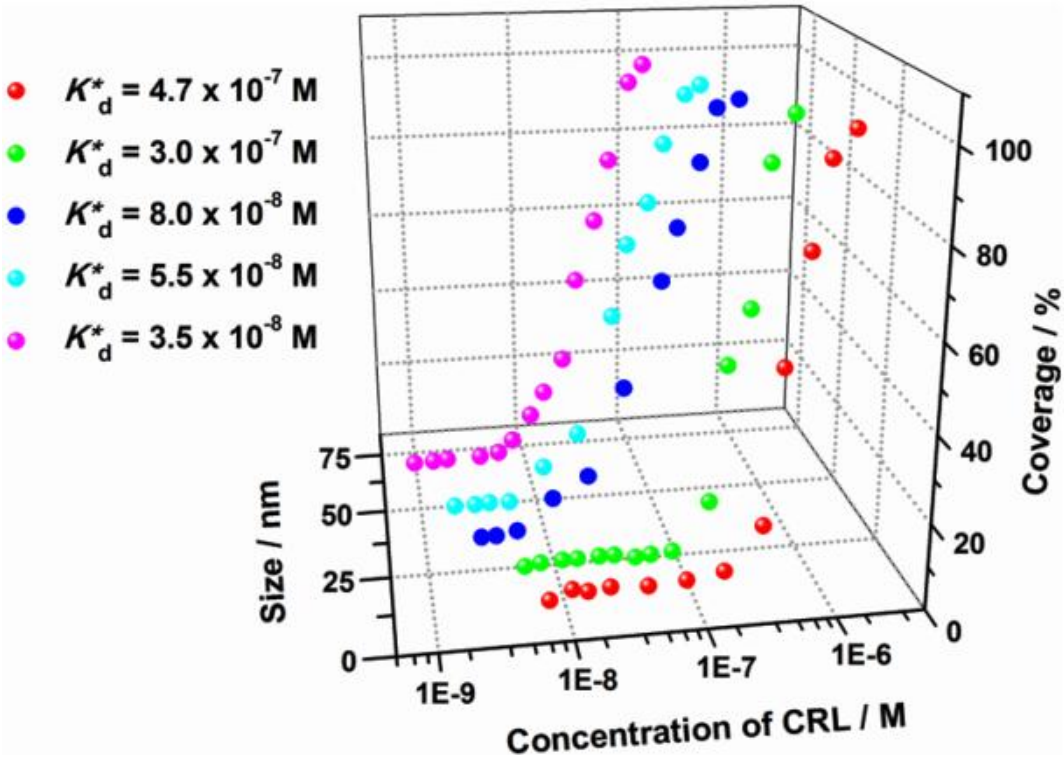

Figure 5.6 Coverages of the differently sized AuNPs plotted with respect to the CRL concentration. Color scheme: red, green, blue, light blue, and pink represent AuNPs having mean diameters of 13.1, 25.2, 37.5, 50.8, and 69.6 nm, respectively.

5.2.3 Preparation of CRL–AuNP Conjugates

For the preparation of CRL–AuNP conjugates, sufficient concentrations of CRL (10-fold K^*_d of each set of CRL–AuNP complexes; over 90% enzyme coverage) were mixed with the AuNP solutions of various sizes to ensure colloidal stability. To remove excess enzyme, the CRL–AuNP conjugates were washed repeatedly through centrifugation (20 min at 13,000 rpm), removal of supernatant and re-dispersion in PBS solution (140 mM NaCl, 2.7 mM KCl, and 10 mM phosphate buffer; pH 7.4). To assure that all unbound CRL was removed from the colloidal suspensions, activity tests were performed on the supernatants from the centrifugation/washing procedure (attachment assay). Table 5.2 shows the drop in activity to zero as the conjugates are repeatedly cleaned. This procedure was repeated six times until no activity was measured to ensure the absence of free CRL in the systems. Then, the CRL–AuNP conjugates of various sizes were stored in the buffer solution for the quantification and activity assay (See Figure 5.7 and Figure 5.8a–c).

Table 5.2 Supernatant activity tests[a] during removal of unbound CRL from AuNP samples (mean sizes: 13.1, 25.2, 37.5, 50.8, and 69.6 nm, respectively) using centrifugation

sample	activity ($\mu M\ s^{-1}$)[b]				
	13.1 nm	25.2 nm	37.5 nm	50.8 nm	69.6 nm
supernatant 1	2.0033 ± 0.0094	1.4827 ± 0.0070	0.5603 ± 0.0079	0.3466 ± 0.0054	0.1868 ± 0.0036
supernatant 2	0.6416 ± 0.0110	0.4775 ± 0.0092	0.1849 ± 0.0059	0.1177 ± 0.0051	0.0704 ± 0.0022
supernatant 3	0.1187 ± 0.0054	0.0861 ± 0.0030	0.0686 ± 0.0030	0.0374 ± 0.0022	0.0099 ± 0.0014
supernatant 4	0.0402 ± 0.0022	0.0161 ± 0.0016	0.0085 ± 0.0014	0.0000 ± 0.0000	0.0000 ± 0.0000
supernatant 5	0.0000 ± 0.0000	0.0000 ± 0.0000	0.0000 ± 0.0000	0.0000 ± 0.0000	0.0000 ± 0.0000
supernatant 6	0.0000 ± 0.0000	0.0000 ± 0.0000	0.0000 ± 0.0000	0.0000 ± 0.0000	0.0000 ± 0.0000
blank	0.0000 ± 0.0000	0.0000 ± 0.0000	0.0000 ± 0.0000	0.0000 ± 0.0000	0.0000 ± 0.0000

[a]Conditions: the reaction buffer was prepared by mixing PBS solution (140 mM NaCl, 2.7 mM KCl, and 10 mM phosphate buffer; pH 7.4; 1.3 mL), 2 mM substrate (*p*NPP) in IPA (0.1 mL), and supernatants (0.1 mL) from the centrifugation/washing procedure or DI water (0.1 mL) for blank. The activity assay experiments were carried out at 30°C.

[b]The initial rate of the change in absorbance at 405 nm is converted to activity ($\mu M\ s^{-1}$) using the molar absorption coefficient of 14,100 $M^{-1}\ cm^{-1}$ for the product of *p*-nitrophenol (*p*NP) in this assay.

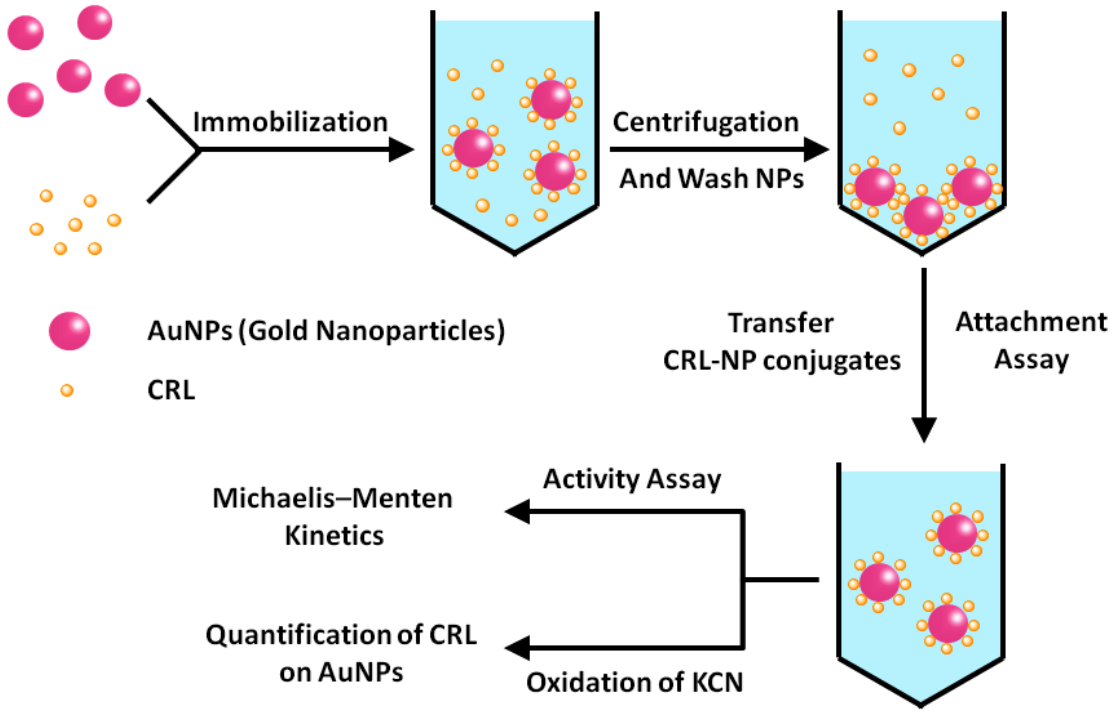

Figure 5.7 Schematic representation of the experimental process for the preparation of CRL–AuNP conjugates.

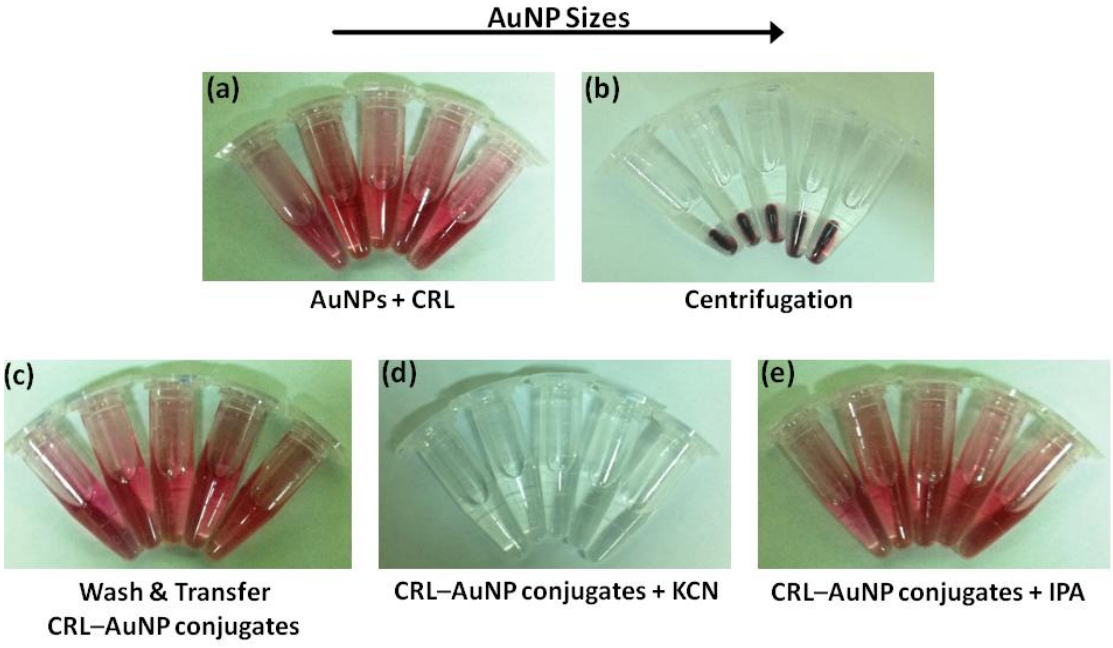

Figure 5.8 Photographic image of the preparation of CRL–AuNP conjugates featuring AuNP sizes varying from 13.1 to 69.6 nm (as shown from left to right in each image). AuNPs with CRL (a) before and (b) after centrifugation, (c) CRL–AuNP conjugates were washed repeatedly and re-dispersion in PBS solution, (d) CRL–AuNP conjugates with KCN, and (e) CRL–AuNP conjugates with IPA.

To detect the CRL loading on the AuNPs of various sizes, the CRL–AuNP conjugates were oxidized with 0.04 M potassium cyanide (KCN) for 60 min in order to liberate bound proteins from the surfaces[134,135] (See Figure 5.8d), and the free enzyme of the solutions were quantified. To remove the reaction buffer of KCN, these solutions were centrifuged at 12,000 rpm for 10 min using Vivaspin 500 centrifugal concentrators, and then their concentrations were determined by the measurement of absorbance at 280 nm with that of a standard curve prepared using known concentrations of CRL ($\varepsilon = 3.7 \times 10^4$ M^{-1} cm^{-1} at 280 nm). For AuNPs having mean sizes of 13.1, 25.2, 37.5, 50.8, and 69.6 nm, the enzyme concentrations were 104.3 ± 3.2, 61.7 ± 0.8, 16.5 ± 0.6, 11.0 ± 0.1, and 6.8 ± 0.1 nM, respectively. These values were reported for the activity assays of various CRL–AuNP conjugate systems.

The coverage of each particle size could be calculated by dividing the number of CRL per particle by the surface area (see the Table 5.3 as shown below). From these data, the number of proteins per particle for the larger AuNPs had higher values. When varying the AuNPs' dimensions, the values of coverage displayed a decreasing trend in the presence of larger AuNP size. This phenomenon was ascribed to the effect of surface curvature of the NPs. However, the most important issue was that these observations suggested the CRL can bind to the surface of NPs for the formation of CRL–AuNP conjugates after the centrifugation procedure.

Table 5.3 Average values for the number of proteins per particle and surface density (coverage) for each particle size

AuNP Size (nm)	proteins/particle	coverage (proteins/cm^2)
13.1	5	$9.9 \times 10^{11} \pm 3.1 \times 10^{10}$
25.2	15	$7.9 \times 10^{11} \pm 1.0 \times 10^{10}$
37.5	22	$5.1 \times 10^{11} \pm 1.8 \times 10^{10}$
50.8	37	$4.6 \times 10^{11} \pm 0.4 \times 10^{10}$
69.6	59	$3.9 \times 10^{11} \pm 0.6 \times 10^{10}$

5.2.4 Activity Assay of CRL–AuNP Conjugated Systems

Based on the specific behavior of lipases as interfacial catalysts, our preliminary experiments for only 13 ± 1 nm AuNPs revealed that the catalytic activity of CRL could be enhanced when used in the form of CRL–AuNPs. In this work, to examine how the apparent enzymatic activity of CRL changed with respect to the AuNP sizes, we performed assays with the CRL–AuNP conjugates prepared using five differently sized sets of AuNPs. We performed the experiments by mixing a solution of substrate *p*-nitrophenyl palmitate (*p*NPP) in propan-2-ol (IPA) with the other reactants in the reaction buffer.[90] To ensure the stability of AuNPs in IPA for the activity assays, we monitored the colloid solution in terms of its color and examine the absorbance spectra (See Figure 5.9). The red line in the spectrum demonstrated that the condition of AuNPs in IPA still retained the colloidal stability. After the addition of NaCl solution, the Au colloids aggregated (blue line). These observations suggested that this condition (AuNPs in IPA) did not induce the aggregation of AuNPs (with colloidal stability). These observations suggested that this condition did not induce the aggregation of AuNPs (with colloidal stability), allowing us to perform the activity analyses.

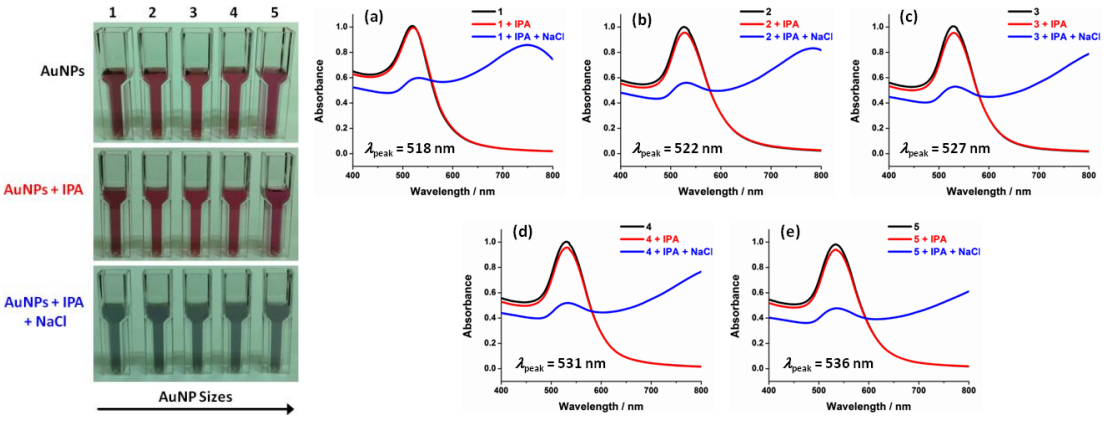

Figure 5.9 Photographic images and absorbance spectra of AuNP solutions in different conditions. The AuNP sizes varying from 1 to 5 had the values of absorption peak (λ_{peak}) of (a) 518, (b) 522, (c) 527, (d) 531, and (e) 536 nm, respectively.

Using UV–Vis spectrophotometry, we detected the activities of the CRL–AuNP conjugates by measuring the absorbance of *p*-nitrophenol (*p*NP), a hydrolysis product from *p*NPP, at 405 nm. The formation of *p*NP was linearly dependent on the reaction time during the monitoring period. The initial reaction rate was, therefore, calculated from the slope of the absorption change against the reaction time, where the absorbance was converted to the corresponding concentration scale by using a molar absorption coefficient of 14,100 M^{-1} cm^{-1} for *p*NP. In Figure 5.10, we observed that the initial release of *p*NP (per enzyme concentration) was proportional to the reaction time of various CRL–AuNP conjugated systems; in the insert of relative activity, there was a significant increase in the catalytic activity in the system featuring the smaller NPs, revealing that the size of the AuNPs was an important factor for the modulation of enzyme activity.

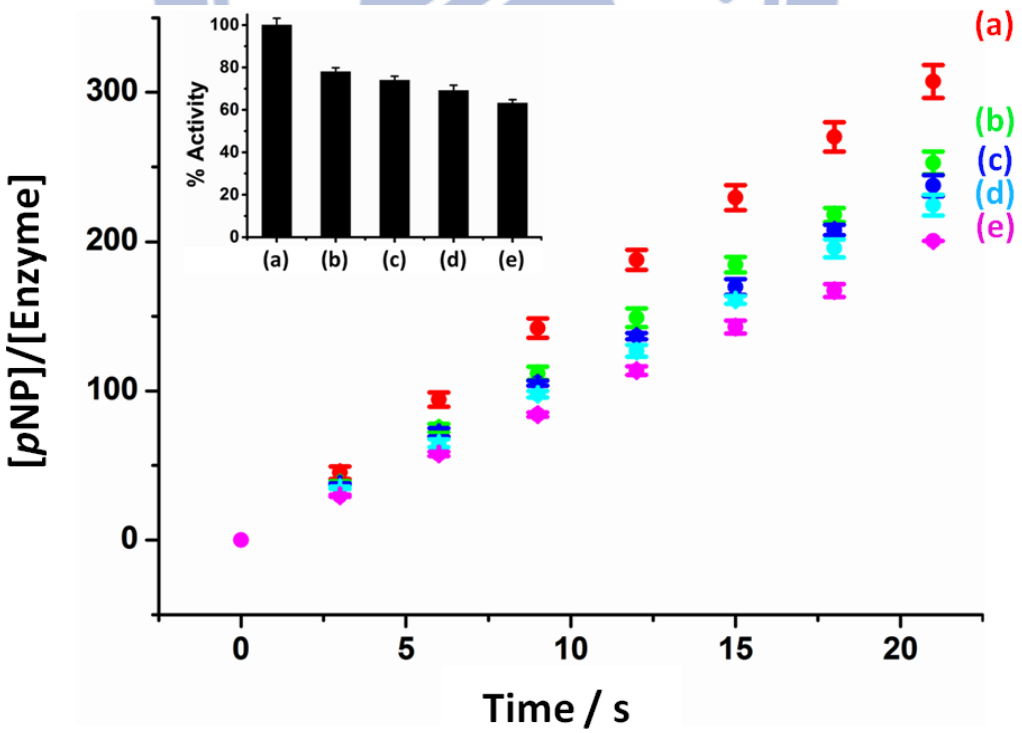

Figure 5.10 Initial release of *p*NP from *p*NPP, plotted as a function of the reaction time of various CRL–AuNP conjugated systems. Inset: Relative activity. Mean diameters of AuNPs: (a) 13.1, (b) 25.2, (c) 37.5, (d) 50.8, and (e) 69.6 nm.

5.2.5 Kinetic Investigation of CRL–AuNP Conjugates

Activity assays were performed for the AuNPs of various sizes to verify the possibility of modulation to enzymatic activity. In the enzymatic kinetics experiment, Figure 5.11 provides the Michaelis–Menten plots for the hydrolysis of *p*NPP (5.55–133.33 μM) catalyzed by the CRL–AuNP conjugates incorporating AuNPs of various average sizes. Although the turnover numbers k_{cat} for the various-sized AuNPs were similar (in Figure 5.12, each curve converges to 18.6 ± 0.39 s^{-1}), the Michaelis constants K_m for the smaller AuNPs had lower values (See Table 5.4 as listed all catalytic parameters).

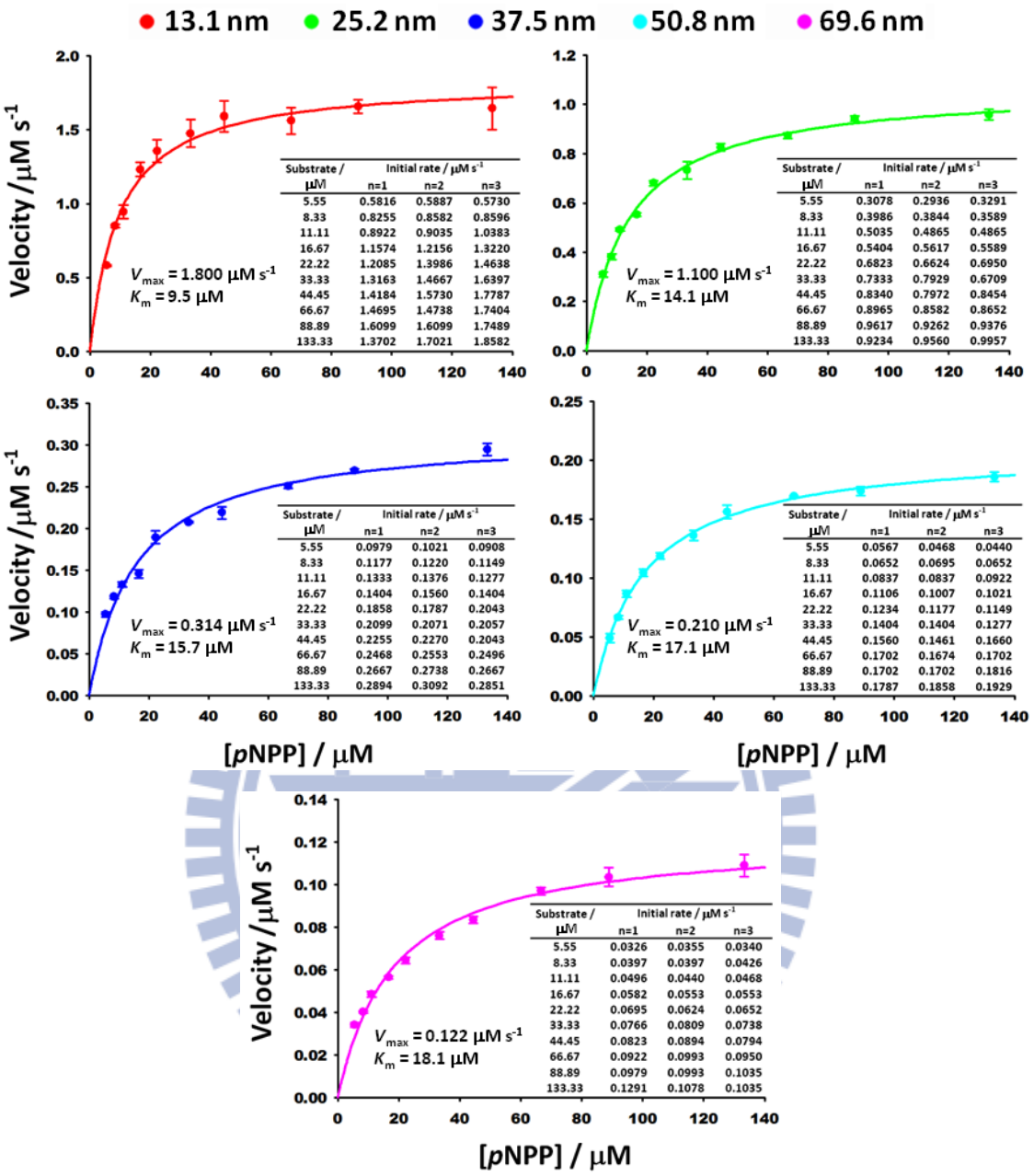

Substrate / μM	Initial rate / μM s^{-1} n=1	n=2	n=3
5.55	0.5816	0.5887	0.5730
8.33	0.8255	0.8582	0.8596
11.11	0.8922	0.9035	1.0383
16.67	1.1574	1.2156	1.3220
22.22	1.2085	1.3986	1.4638
33.33	1.3163	1.4667	1.6397
44.45	1.4184	1.5730	1.7787
66.67	1.4695	1.4738	1.7404
88.89	1.6099	1.6099	1.7489
133.33	1.3702	1.7021	1.8582

Substrate / μM	Initial rate / μM s^{-1} n=1	n=2	n=3
5.55	0.3078	0.2936	0.3291
8.33	0.3986	0.3844	0.3589
11.11	0.5035	0.4865	0.4865
16.67	0.5404	0.5617	0.5589
22.22	0.6823	0.6624	0.6950
33.33	0.7333	0.7929	0.6709
44.45	0.8340	0.7972	0.8454
66.67	0.8965	0.8582	0.8652
88.89	0.9617	0.9262	0.9376
133.33	0.9234	0.9560	0.9957

Substrate / μM	Initial rate / μM s^{-1} n=1	n=2	n=3
5.55	0.0979	0.1021	0.0908
8.33	0.1177	0.1220	0.1149
11.11	0.1333	0.1376	0.1277
16.67	0.1404	0.1560	0.1404
22.22	0.1858	0.1787	0.2043
33.33	0.2099	0.2071	0.2057
44.45	0.2255	0.2270	0.2043
66.67	0.2468	0.2553	0.2496
88.89	0.2667	0.2738	0.2667
133.33	0.2894	0.3092	0.2851

Substrate / μM	Initial rate / μM s^{-1} n=1	n=2	n=3
5.55	0.0567	0.0468	0.0440
8.33	0.0652	0.0695	0.0652
11.11	0.0837	0.0837	0.0922
16.67	0.1106	0.1007	0.1021
22.22	0.1234	0.1177	0.1149
33.33	0.1404	0.1404	0.1277
44.45	0.1560	0.1461	0.1660
66.67	0.1702	0.1674	0.1702
88.89	0.1702	0.1702	0.1816
133.33	0.1787	0.1858	0.1929

Substrate / μM	Initial rate / μM s^{-1} n=1	n=2	n=3
5.55	0.0326	0.0355	0.0340
8.33	0.0397	0.0397	0.0426
11.11	0.0496	0.0440	0.0468
16.67	0.0582	0.0553	0.0553
22.22	0.0695	0.0624	0.0652
33.33	0.0766	0.0809	0.0738
44.45	0.0823	0.0894	0.0794
66.67	0.0922	0.0993	0.0950
88.89	0.0979	0.0993	0.1035
133.33	0.1291	0.1078	0.1035

Figure 5.11 Michaelis–Menten plots for the hydrolyses of *p*NPP mediated by the various functionalized AuNPs. Insets: Initial rates (μM s^{-1}) listed with respect to the substrate concentration and the kinetic parameters ($p < 0.05$).

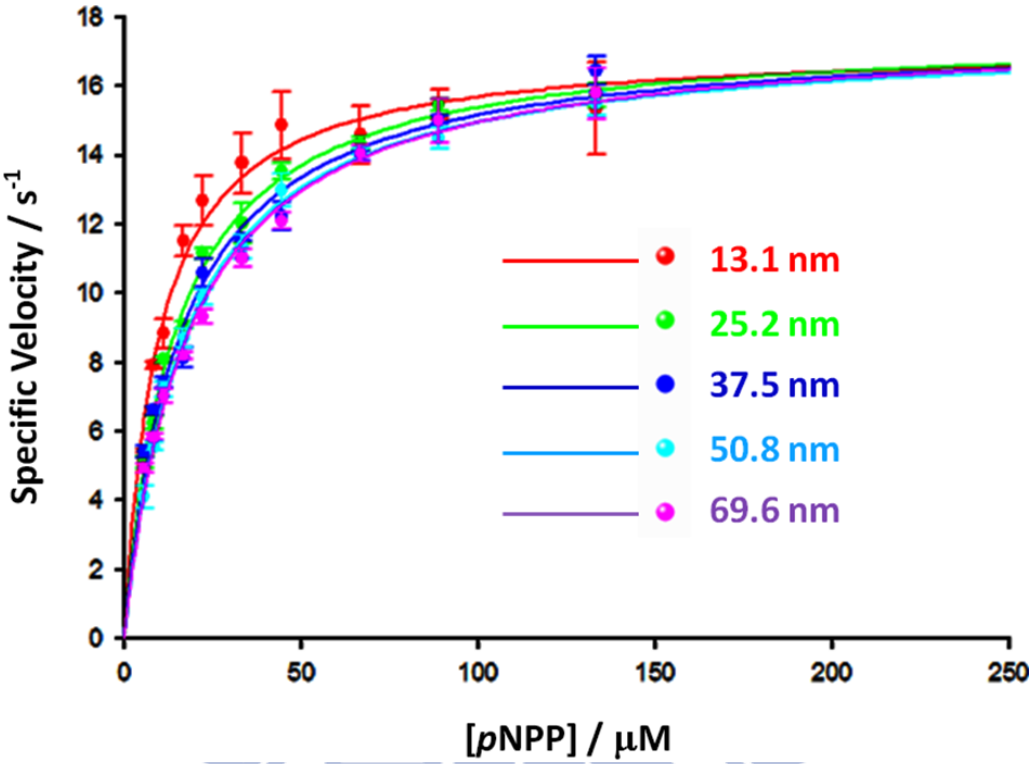

Figure 5.12 Michaelis–Menten plots for *p*NPP hydrolysis catalyzed by CRL–AuNP conjugates featuring AuNP sizes varying from 13.1 to 69.6 nm. Lines of best fit were obtained from the data using Enzyme Kinetics Module software.

Table 5.4 Experiment-determined catalytic parameters of turnover numbers (k_{cat}), Michaelis constants (K_m), and specificity constants (k_{cat}/K_m) for the free CRL, the CRL–AuNP conjugates and planar surface–immobilized CRL systems

AuNP Size (nm)	k_{cat} (s^{-1})	K_m (μM)	k_{cat}/K_m ($\mu M^{-1} s^{-1}$)
free enzyme	19.4 ± 0.89	23.3 ± 2.90	0.83 ± 0.14
13.1	18.0 ± 0.56	9.5 ± 1.02	1.89 ± 0.26
25.2	18.3 ± 0.26	14.1 ± 0.68	1.30 ± 0.08
37.5	19.6 ± 0.43	15.7 ± 1.11	1.25 ± 0.12
50.8	19.1 ± 0.30	17.1 ± 0.84	1.12 ± 0.07
69.6	17.9 ± 0.38	18.1 ± 1.20	0.99 ± 0.09
immibilized on a planar surface (NP size → ∞)	(18.6 ± 0.39)[a]	(22.6 ± 1.41)[b]	0.82 ± 0.07

[a]Average turnover numbers (k_{cat}) for the reaction solutions of various CRL–AuNP conjugate systems.

[b]Data measured using the Lee–Yang approach from reference 117 (See the Appendix I; page 88–100).

The value of K_m in the kinetic studies represents the affinity of the enzyme toward the substrate; the rate-limiting step (k_{cat}) was determined by monitoring the product's release. For the CRL–AuNP conjugates incorporating AuNPs having mean diameters of 13.1, 25.2, 37.5, 50.8, and 69.6 nm, the enzyme concentrations were 104.3, 61.7, 16.5, 11.0, and 6.8 nM, respectively. Figure 5.13a revealed that the value of V_{max} was proportional to the enzyme concentration. Thus, similar values of k_{cat} were obtained for the various functionalized AuNPs ($V_{max} = k_{cat}[E]$). Therefore, the significant increase in the enzymatic activity in the presence of the smaller AuNPs was due to the lower values of K_m (Figure 5.13b).

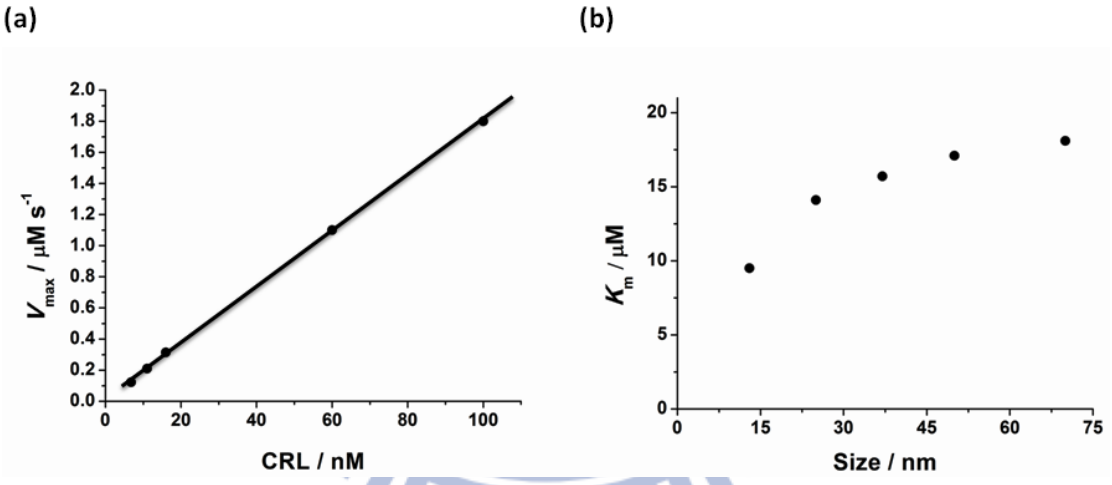

Figure 5.13 Plots of the values of (a) V_{max} with respect to the enzyme concentration in the presence of various CRL–AuNP conjugate systems and (b) K_m with respect to the AuNP size.

In Table 5.4, when varying the AuNPs' dimensions, the values of K_m displays an increasing trend in the presence of larger AuNP size, even under the extreme condition of AuNP size → ∞ (the kinetics of the enzyme immobilized on one side of a planar surface could be effectively modeled and measured;[117] See the Appendix I; page 88–100). In simple terms, the rate constants for the individual steps can be described in equation (eq) 1:

$$E_{NP} + S \underset{k_{-1}}{\overset{k_1}{\rightleftharpoons}} E_{NP}\text{-}S \xrightarrow{k_{cat}} E_{NP} + P \quad (1)$$

An obtained lower value of K_m [$(k_{-1} + k_{cat})/k_1$] represents greater kinetic affinity between the enzyme and the substrate; i.e., the conjugated system with the smaller AuNPs exhibited enhanced kinetic affinity, thereby improving the catalytic efficiency k_{cat}/K_m. This observation suggests the enzyme activity is tunable by suitable immobilization of corresponding size of nanoparticles.

5.2.6 Collision Model with a Shielding Factor

NPs with various dimensions, compositions, and surface modifications have been investigated, through kinetic analyses, for their interactions with enzymes.[41,51,71–74,123] The hydrophobic and surface interactions have been attributed as the major drivers behind enzyme–NP association. In contrast, far fewer efforts have been made to model the "*exterior*" behavior of such conjugates—in particular, their interactions with other biomolecules. Our research, concerning the steric hindrance of a shielding factor, emphasizes the importance of such "*exterior*" interactions on the catalytic behavior.

To further correlate the NP dimensions (size effects) to the catalytic efficiency (k_{cat}/K_m) of the conjugated enzyme, we developed a shielding model based on diffusion–collision theory. We made the following assumptions: (i) the NPs, enzymes, and substrate molecules behaved as "rigid balls" (See Figure 5.14); (ii) the immobilization of enzyme–NP conjugates was monolayer coverage; (iii) the intrinsic properties of the enzymes conjugated onto the differently sized NPs were similar; and (iv) the orientation of the active site of the enzyme–NP conjugates was random.[129,130] Considering a catalytic reaction between an enzyme E_{NP}, bearing a spherical NP of size comparable to that of the enzyme (Figure 5.14b), and a corresponding substrate *S*

as a bimolecular reaction, the two molecules must first collide and then a product P is released, as indicated in eq 2. Here, the subscript "NP" designates the enzyme–NP conjugate. The reaction rate ν (μM s^{-1}) can be expressed as the product of the bimolecular rate constant k^{coll} (μM^{-1} s^{-1}) and the concentrations of the enzyme (C_E) and substrate (C_S), as indicated in eq 3.

$$E_{NP} + S \rightarrow E_{NP} + P \quad (2)$$

$$\nu = k^{coll} C_E C_S \quad (3)$$

The constant k^{coll} can be expressed as:

$$k^{coll} = Z \cdot p \cdot e^{(-\frac{E\,act}{RT})} \quad (4)$$

where Z (μM^{-1} s^{-1}) is the frequency of collisions; p is the fraction of substrates that have the correct orientation; E_{act} is the activation energy; R is the gas constant; and T is the absolute temperature. Unlike free enzymes in solution, the enzyme–NP conjugates impart extra steric hindrance of interest. We define a shielding factor η as the solid-angle fraction of the enzyme surface open to the substrate; the open solid-angle fraction Ω is depicted in Figure 5.14c. The eq 4 can be rewritten in the following form:

$$k_{E-NP}^{coll} = Z \cdot p \cdot \eta \cdot e^{(-\frac{E_{act}}{RT})} \quad (5)$$

The shielding region on the enzyme surface was defined as the region inside the cone having a solid angle of 4π-Ω, the surface of which was tangential to the NP surface and passed through the center of the enzyme. The shielding factor η in eq 5 was the ratio of the open solid angle Ω, outside the cone, to the total solid angle (4π) of an enzyme immobilized on the surface of a NP. Based on the diffusion–collision model derived in the following Section, the shielding effect described herein clearly involved hindrance in the diffusion direction on the long-range scale rather than in the collision direction on the short-range scale (mean-free-path level); the latter effect

should belong to p in eq 5. The open solid angle Ω can be represented in integral form as follows (See Figure 5.14d):

$$\Omega = \frac{\int_{\theta}^{\pi} 2\pi r_{\mathrm{E}}^2 \sin\theta \, \mathrm{d}\theta}{r_{\mathrm{E}}^2} = 2\pi(1 + \cos\theta) \tag{6}$$

Using Pythagoras' theorem, the expression for Ω can be further rearranged into:

$$\Omega = 2\pi\left[1 + \frac{\sqrt{r_{\mathrm{E}}(2r_{\mathrm{NP}} + r_{\mathrm{E}})}}{r_{\mathrm{NP}} + r_{\mathrm{E}}}\right] \tag{7}$$

where r_{NP}, r_{E} (= 5.17 nm), and r_{S} (= 0.5788 nm) are the radii of the NP, enzyme, and substrate, respectively (See the Appendix II and III).

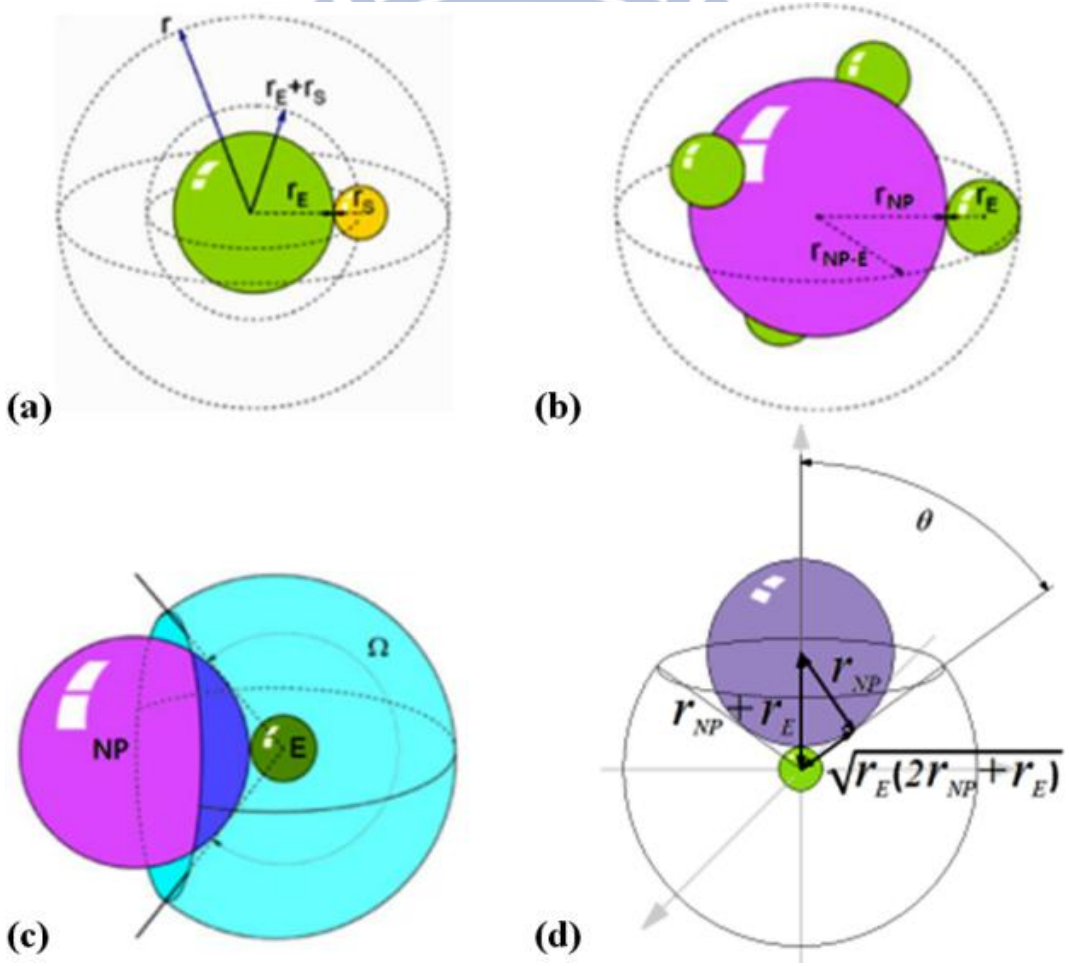

Figure 5.14 Geometric relationships between the substrate *S*, the enzyme *E* and the nanoparticle *NP*. (a) If the distance between the *S* and *E* was less than the sum of the radii of two bounding spheres, $r_{\mathrm{E}} + r_{\mathrm{S}}$, then a collision event occurred. (b) Concerning diffusion effects in a fluid, the effective radius of the enzyme–NP conjugate should increase to $r_{\mathrm{NP}} + 2r_{\mathrm{E}}$. (c) The solid-angle fraction Ω exposed for collisions between the substrate and the enzyme. (d) Geometric relationships of the respective radii.

5.2.7 Diffusion–Collision Theory for Enzyme–NP Conjugates

Assuming that the enzyme molecules were immobilized onto the NP supports in no preferred orientation, if the enzymes were stationary in the diffusion-controlled reaction, the flux of substrates to a single enzyme, $J_{S\to E}$, could be determined by integrating the number of substrates entering a sphere centered at the enzyme molecule, as indicated in Figure 5.14a. We integrate from contact (at $r_E + r_S$) to infinity.

$$J_{S\to E} = 4\pi r^2 D_S \frac{dN_S}{dr} \tag{8}$$

$$J_{S\to E} \int_{r_E+r_S}^{\infty} \frac{dr}{r^2} = 4\pi D_S \int_0^{N_S} dN_S \tag{9}$$

Thus,

$$J_{S\to E} = 4\pi D_S (r_E + r_S) N_S \tag{10}$$

where D_E and D_S, N_E and N_S represent the diffusion coefficients, and number concentrations (in molecules cm^{-3}), respectively, each for the enzyme and the substrate, respectively. Based on a steady-state process, the flux $J_{S\to E}$ will be equal to the number of effective collisions per enzyme per second; this physical meaning of $J_{S\to E}$ is quite similar to that of the turnover number k_{cat} for enzymes in enzymology. Because the enzymes immobilized onto the NPs were not stationary, we must use the relative diffusion coefficient, $D_E + D_S$, instead of D_S in eq 10. The total rate of effective collision per cubic centimeter per second is, thus,

$$Z' = 4\pi (D_E + D_S)(r_E + r_S) N_E N_S \tag{11}$$

and the reaction rate can be re-expressed (in M s^{-1}) as

$$\nu' = \frac{1000\,Z'}{N_{\mathrm{Avo}}} = \frac{4000\pi(D_{\mathrm{E}} + D_{\mathrm{S}})(r_{\mathrm{E}} + r_{\mathrm{S}})N_{\mathrm{E}}N_{\mathrm{S}}}{N_{\mathrm{Avo}}} \tag{12}$$

Here, N_{Avo} is Avogadro's constant. Clearly, there is an assumption in eq 12 based on diffusion-controlled process: that the substrate concentration at the enzyme surface is zero; therefore, the reaction rate ν' in eq 12 is the diffusion-limited maximum rate for enzyme catalysis in the limiting case of eq 5 (i.e., $\eta \rightarrow 1$ and $E_{\mathrm{act}} = 0$); thus, we note that $C_{\mathrm{E}} = 1000N_{\mathrm{E}}/N_{\mathrm{Avo}}$, and eq 3 can be represented for this maximum rate as eq 13.

$$\nu' = Z\,p\,C_{\mathrm{E}}\,C_{\mathrm{S}} = Z\,p\left(\frac{1000\,N_{\mathrm{E}}}{N_{\mathrm{Avo}}}\right)\left(\frac{1000\,N_{\mathrm{S}}}{N_{\mathrm{Avo}}}\right) \tag{13}$$

Combining eqs 12 and 13, we can eliminate ν' to obtain the maximum frequency of effective collisions, Zp (in $\mathrm{M^{-1}\,s^{-1}}$):

$$Z\,p = \frac{\pi\,N_{\mathrm{Avo}}(D_{\mathrm{E}} + D_{\mathrm{S}})(r_{\mathrm{E}} + r_{\mathrm{S}})}{250} \tag{14}$$

Using the Stokes–Einstein equation, eq 15, the diffusion coefficients of the substrate and the enzyme in eq 14 can be related to their respective radii.

$$D = \frac{k_{\mathrm{B}}\,T}{6\pi\,\mu r} \tag{15}$$

where k_{B} is the Boltzmann constant and μ is the solution viscosity. Furthermore, because the attachment of the enzymes to the NPs must significantly affect their diffusion rate, the effective radius of the enzyme must be increased to $r_{\mathrm{E-NP}} = r_{\mathrm{NP}} + 2r_{\mathrm{E}}$ from r_{E}, i.e., the radius of the enzyme–NP conjugate presented in Figure 5.14b. Substituting eq. 15 into eq. 14, we then obtain

$$Zp = \frac{RT}{1500\,\mu}\left(\frac{1}{r_{\mathrm{E-NP}}} + \frac{1}{r_{\mathrm{s}}}\right)(r_{\mathrm{E}} + r_{\mathrm{S}}) \tag{16}$$

Finally, concerning the shielding effect, we modified both the bimolecular collision model and the diffusion–collision model as above to describe the effect of the NP size on the catalysis of the enzyme–NP conjugate. For clarity, we define the group *Zp* as $k^{\text{eff}}_{\text{max}}$ (the maximum frequency of effective collisions for the enzyme–NP conjugate system) to obtain as following summarizing set of equations:

$$k_{\text{E-NP}}^{\text{coll}} = Z \cdot p \cdot \eta \cdot \text{e}^{(-\frac{E_{\text{act}}}{RT})} = k_{\text{max}}^{\text{eff}} \cdot \eta \cdot \text{e}^{(-\frac{E_{\text{act}}}{RT})} \tag{17}$$

$$k_{\text{max}}^{\text{eff}} = \frac{RT}{1500\mu}\left(\frac{1}{r_{\text{NP}} + 2r_{\text{E}}} + \frac{1}{r_{\text{S}}}\right)(r_{\text{E}} + r_{\text{S}}) \tag{18}$$

$$\eta = \frac{\Omega}{4\pi} = \frac{1}{2}\left[1 + \frac{\sqrt{r_{\text{E}}(2r_{\text{NP}} + r_{\text{E}})}}{r_{\text{NP}} + r_{\text{E}}}\right] \tag{19}$$

5.2.8 Effect of Nanoparticle Size on the Catalytic Activity: Theoretical Approach

Substituting the viscosity, absolute temperature, and radii (r_{E} = 5.17 nm; r_{S} = 0.58 nm; evaluated in the Appendix II and III, respectively) into equations 17–19 gave the bimolecular rate constants $k_{\text{E-NP}}^{\text{coll}}$ listed in Table 5.5. For the AuNPs having average diameters in the range 13.1–69.6 nm, the theoretical rate constants $k_{\text{E-NP}}^{\text{coll}}$ and the experiment-determined catalytic efficiencies (or specificity constant) $k_{\text{cat}}/K_{\text{m}}$ followed identical trends. In this model, when considering the extreme condition of $r_{\text{NP}} \rightarrow \infty$, the theoretical rate constant becomes 39.3% (0.48/1.22) of that for the system having a mean AuNP size of 13.1 nm; this limit represents CRL molecules immobilized onto a planar surface. Compare to the measured catalytic efficiency in Table 5.4, the enzyme immobilized onto a planar surface is 43.4% (0.82/1.89) of that of the system featuring AuNPs having a mean size of 13.1 nm. This percentage change is fairly

consistent with the theoretical prediction. The enhanced activity by size-effect would theoretically converge to a finite maximum value when the AuNP size approaches zero. There are two factors that affect the rate constant in this size-effect model: the major one is shielding hindrance effect; the minor one is the change in diffusion coefficient. Within the model of classical enzymatic kinetics, the shielding factor mainly affects the rate constant k_1, not k_{-1} or k_{cat} in eq 1; that is, the steric hindrance affects only the binding path of the substrates, and not the desorption of the complex E_{NP}·S. The experiment of kinetic analysis reveals that the values of k_{cat} were almost independent of the AuNP size, whereas the values of K_m correlated strongly with it. Thus, this size-effect model has physical meaning and reasonably explains the kinetic response of this enzyme–NP conjugate system.

Table 5.5 Theoretical parameters[a] for the CRL–AuNP conjugates and planar surface–immobilized CRL systems

AuNP Size (nm)	μ (cP)	k^{eff}_{max} ($\mu M^{-1} s^{-1}$)	η	exp($-E_{act}/RT$) at 303 K	k^{coll}_{E-NP} ($\mu M^{-1} s^{-1}$)
NP size → 0	(1.13 ± 0.017)[b]	15.56	1.00		1.37
13.1	1.14 ± 0.016	15.11	0.91		1.22
25.2	1.14 ± 0.012	14.97	0.85	0.0880	1.12
37.5	1.14 ± 0.016	14.90	0.81	± 0.0058	1.06
50.8	1.12 ± 0.016	15.11	0.78		1.03
69.6	1.13 ± 0.025	14.92	0.75		0.98
immibilized on a planar surface (NP size → ∞)	1.52 ± 0.021	10.95	0.50		0.48

[a]The maximum frequency of effective collisions (k^{eff}_{max}), shielding factor (η), and bimolecular rate constant (k^{coll}_{E-NP}) were calculated in equations 17–19.

[b]Average viscosity (μ) for the reaction solutions of various CRL–AuNP conjugate systems.

5.3 Conclusions

In summary, we have performed a series of experiments to systematically analyze the modulated NP size–dependent enzymatic activities of CRL–AuNP conjugates, and have developed a shielding model to explain the correlation between the size effects and the kinetic responses. A simple and efficient method for the preparation of this functional conjugates, with colloidal stability, under retention of enzymatic activity has been reported. The association of CRL with the AuNPs did not influence the values of k_{cat}, but the smaller AuNPs did promote the catalytic efficiency of CRL by increasing its kinetic affinity (i.e., lower K_m values) toward the substrate *p*NPP. From a quantitative investigation of the enzymatic kinetics of CRL bound to AuNPs of well-defined sizes, we found that the sizes of these conjugates acted as a controllable and efficient factor for modulating the activity of the enzyme. We believe that as the integrative field of nanobiotechnology evolves, such studies of the fundamental interactions of nanostructures with biological systems will become, by necessity, more common.

Appendix

I. A Surface Limited Model for the Evaluation of Immobilized Enzyme on Planar Surface

In our previous study (C.-C. Lee, H.-P. Chiang, K.-L. Li, F.-H. Ko, C.-Y. Su, Y.-S. Yang, *Anal. Chem.* **2009**, *81*, 2737–2744),[117] we found that the kinetics of the enzyme immobilized on the planar surface could be effectively modeled and measured. In this work, we followed the experimental process and theoretical model to calculate the kinetic values at this extreme condition. We provide the experimental details of the assay for the measurement of the kinetic parameters of immobilized enzyme on planar surface in this section.

Experimental Section

Cleaning and Silanization of Silicon Wafer. P-type Si(100) wafers (14–21 Ω-cm, MEMC, MO, USA) with 15 cm diameter, on which 100 nm oxide layers were grown using wet oxidation with a gas mixture of hydrogen (8000 cm^3/min) and oxygen (5000 cm^3/min) at 978^oC, were cut into 4×8 cm^2 pieces of samples to serve as a supporting material for enzyme immobilization. Prior to immobilization, the piece of oxidized silicon wafer was carefully cleaned in the SPM (sulfuric–peroxide mixture), H_2SO_4 and H_2O_2 (volume ratio is 3:1), twice, each time at above 85^oC for 30 min. It should be noted that the cleaning solution is very corrosive and dangerous. After rinsing with pure water and drying, the sample was immersed in the (3-aminopropyl)triethoxysilane (APTES, Sigma–Aldrich, MO, USA) solution to proceed the silanization reaction for 30 min at room temperature to create an amine-functional surface. The APTES solution was prepared by the following

procedures: (1) mixing pure water with acetone (volume ratio is 5:1), (2) adjusting the pH value of the above solvent to 3.5 by 1 M HCl, and (3) preparing the 5% APTES solution by diluting with above solvent. Following the APTES treatment, the silicon wafer was rinsed with pure water thoroughly. Ultrapure water (>18 MΩ cm at 25^{o}C) was used throughout the experiments. Then, the treated silicon wafer was baked at 120^{o}C for 30 min to complete the Si–O bond formation.

Reactor System and Enzyme Immobilization. The corresponding process flow for enzyme CRL is briefly illustrated in Figure A1a. The reactor composed two plates; the bottom plate was a silicon wafer on glass support, and the top plate, made of quartz, contained a tortuous fluidic guide on its surface. The fluidic channel used was 72.6 cm long (L), 0.194 cm width (W), and 167 μm depth (H).

Reactions involved in the surface modification and the immobilization of CRL are shown in Figure A1b. Prior to immobilization, the AuNPs were prepared in aqueous solution using the chemical reduction method. Aqueous solution of 10 mL 1 mM $HAuCl_4$ ($HAuCl_4 \cdot 3H_2O$, Sigma–Aldrich) and 1 mL 38.8 mM trisodium citrate dehydrate (Showa Chemical Co., Japan) were mixed, and then heated under reflux for 15 min with vigorous stirring. The color of the solution gradually changed from yellow to purplish-red. After cooling to room temperature, colloidal AuNPs were formed in the solution, and then this AuNPs solution was used to rinse the modified surface of the sample for 15 min at room temperature. The surface was extensively rinsed with water immediately after removing from AuNPs colloid suspension, and dried with nitrogen gas. The enzyme (CRL; EC 3.1.1.3, Sigma–Aldrich; 1.5 μM) solution prepared was dipped onto the AuNPs modified surface of the sample, and incubated for 10 min. Finally, the surface was immersed in water for 5 min and dried with nitrogen gas, and then the CRL-immobilized samples were stored at 4^{o}C until enzyme activity assay.

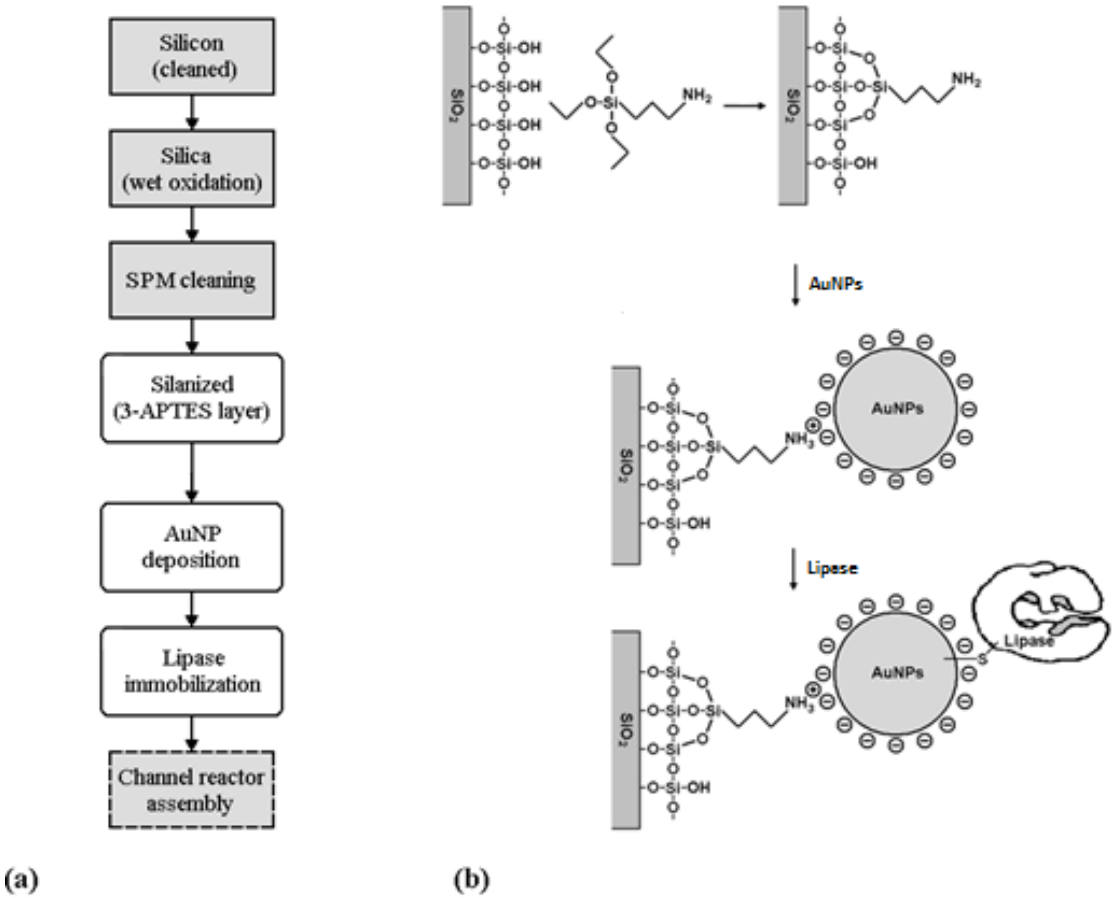

Figure A1 Step-by-step and chemical procedures of enzyme immobilization. (a) Process flow showing the samples used and their preparation technique and (b) schematic diagram of the chemical linking method of enzymes CRL binding to the silica substrate.

CRL Activity Assay. To create relative high and first-ordered substrate conditions, two different concentrations of substrate *p*-nitrophenyl palmitate (*p*NPP), 80 μM and 4 μM, were used, respectively, for the immobilized CRL-catalyzed reaction; these conditions responded to 3.35 and 0.17 times the K_m value of free CRL in homogeneous catalytic reaction, respectively. The assays were performed for immobilized CRL in mixtures as following volume ratio: 1.3 mL phosphate-buffered saline (PBS) buffer solution (tablets, 140 mM NaCl, 2.7 mM KCl, 10 mM Na_2HPO_4, 1.8 mM KH_2PO_4, pH 7.4, Sigma–Aldrich); 0.5 mL propan-2-ol (IPA) containing *p*NPP at 1.2 mM and 0.06 mM for the relative high and first-ordered substrate conditions, respectively; and 0.1 mL DI water.

Detection Methods—Flow Rates and Absorption Measurements. Injection of the reaction mixtures into the reactor was controlled by automatic pumping system (KD Scientific, KDS260P) throughout the experiments and operated at desired flow rate; for CRL assay, the two sets were 0.5, 1, 2 min and 1, 2, 4 min for 80 μM and 4 μM *p*NPP substrate conditions, respectively. Prior to each set of injection, we used buffer to flush the reactor with space time $\tau = 0.25$ min for 3.5 min in CRL assay. The output solution was directed into a quartz flow cell mounted in the UV–Vis spectrophotometer (Hitachi UV–Vis-3310, Tokyo, Japan) for *p*NP detection at 410 nm. The essential components of microfluidic-reactor instrument for kinetics analysis are shown as Figure A2. The molar extinction coefficients of *p*NP absorbance was 14,100 M^{-1} cm^{-1} and 15,000 M^{-1} cm^{-1} for CRL assays at 80 μM and 4 μM *p*NPP, respectively.

(a)

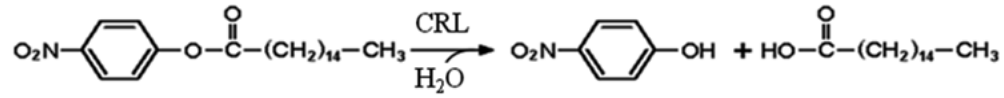

p-Nitrophenyl palmitate (*p*NPP) *p*-Nitrophenol (*p*NP) Palmitic acid

(b)

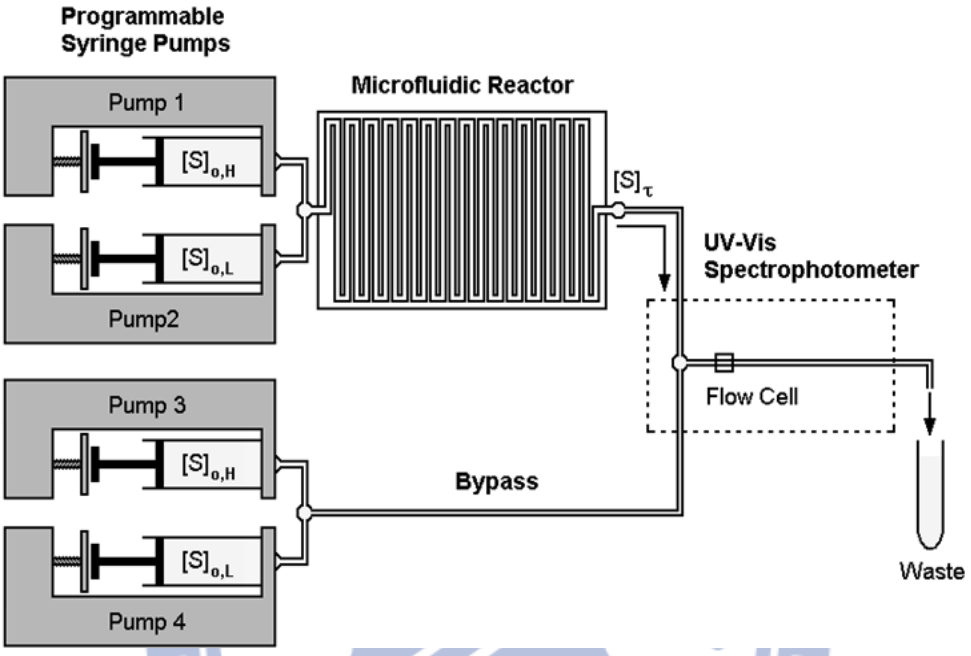

Figure A2 CRL-catalyzed hydrolysis reaction and the associated setups of assay systems. (a) *p*NPP was used as substrate for CRL. The common product, *p*NP, which gives strong absorption at 410 nm in neutral or alkaline, served as the reporter molecule for the progress of the enzyme-catalyzed reaction. Schematic diagram of a typical microfluidic-reactor instrument for (b) the CRL assay system with enzyme-free (*via* bypass) as base line; the substrate *S* is *p*NPP, $[S]_{o,H}$ = 80 μM, $[S]_{o,L}$ = 4 μM.

Theoretical Considerations

For the evaluation of immobilized enzyme on planar surface, it has been shown a microfluidic system—a channel reactor, which combined plug flow approximation, Michaelis–Menten equation, and surface reaction limited condition, to model the kinetics of immobilized enzyme on one-side planar surface as eq (1).

$$\tau = \frac{-K_m^*}{V_{\max}^*/H} Ln(1-\alpha_\tau) + \frac{[S]_o}{V_{\max}^*/H}\alpha_\tau \qquad (1)$$

where space time τ is the time required to process the volume of reaction mixture in reactor, K^*_m is the Michaelis–Menten constant (μmol dm^{-3}) for immobilized enzymes on the planar surface, V^*_{max} is maximum reaction rate per unit surface area of catalyst (μmol dm^{-2} min^{-1}), H is the height of rectangular channel reactor, α_τ is reaction conversion fraction at outlet of the channel, and $[S]_o$ is the substrate concentration at inlet of the channel; the subscript o and τ refer to at the reaction times of an element of fluid in the channel $t = 0$ (at the inlet) and $t = \tau$ (at the outlet), respectively; the superscript * corresponds to the apparent values for immobilized enzyme. Surface reaction limited condition means that diffusion is fast compared to surface reaction. To meet this requirement, the ratio of the reaction volume to the catalytic planar surface must be reduced. According to eq (1), theoretically, there should be several sets among these variants, τ, $[S]_o$, α_τ and H, chosen to design an assay to extract the kinetic constants K^*_m and V^*_{max}.

By using a series of variant flow rates (or space time τs), eq (1) could allow us to precisely predict the kinetics of immobilized enzyme at two different inlet concentrations of substrate. If the reaction conversion fraction, α_τ, is smaller than 9.4%, and $[S]_o$ is higher than about $19K_m$, (here K_m refers to the value of homogeneous enzymatic reaction because K^*_m evaluation has not yet been calculated,) i.e., the assay

condition refers to the pseudo-zero-ordered region of substrate dependency (or the saturating assay condition,) then eq (1) can be degenerated as follows:

$$\alpha_\tau \approx < \frac{V^*_{max}}{H} >_0 \left(\frac{\tau}{[S]_{o,H}}\right) \qquad (for\ [S]_{o,H} \geq 19K_m) \tag{2}$$

where the subscript H of $[S]_{o,H}$ refers to high substrate concentration; the subscript 0 of $< \frac{V^*_{max}}{H} >_0$ refers to initial approximation without regard to K^*_m factor. Equation (2) provides us to determine the average $< \frac{V^*_{max}}{H} >_0$ at a certain time using linear regression of the data sets α_τ *versus* $\left(\frac{\tau}{[S]_{o,H}}\right)$, and the discrete determined values of $< \frac{V^*_{max}}{H} >_0$ at different times in experiment progress could be used to fit a decay curve concerning the issue of deactivation of immobilized enzyme; therefore the any simultaneous value of $< \frac{V^*_{max}}{H} >_0$ can be determined in whole experiment progress.

Following $\frac{V^*_{max}}{H}$ determined as above, to increase the accuracy of K^*_m evaluation, eq (1) obviously also indicates that we should set up the testing condition with lower $[S]_o$ concentrations smaller than or equal to the K_m value (determined in homogeneous catalytic reaction before K^*_m evaluation has not yet been calculated,) and higher conversion fractions α_τs, as long as the output concentration of reporter is not beyond the limit of detection. Eq (1) can be arranged into the following eq (3):

$$< \frac{V^*_{max}}{H} >_0 \tau - [S]_{o,L} \alpha_\tau = - < K^*_m >_0 Ln(1-\alpha_\tau) \tag{3}$$

where the subscript L of $[S]_{o,L}$ refers to low substrate concentration, the subscript 0 of $< K^*_m >_0$ refers to an initial approximation. Applying linear regression of a set of space time τs *versus* the corresponding measured data of conversion fraction α_τs in eq

(3), the estimated value of $< K_m^* >_0$ is the slope of this regression line. If the high substrate concentration used $[S]_{o,H} > 19 < K_m^* >_0$ can still be satisfied, i.e., it is kept under saturating substrate conditions in the whole channel reactor, then $< \frac{V_{\max}^*}{H} >_0$ and $< K_m^* >_0$ determined by eq (2) and eq (3) respectively, will be good enough approximations. (The theoretical error will be smaller than 5.5%.)

Nevertheless, the saturating substrate condition can't always be achieved in some practical assays because of limit of substrate solubility, high-substrate inhibition, or cost concern. With the widespread availability of curve-fitting calculations from experiment data, if the highest available concentration of substrate is at least larger than $3K_m$ (determined in homogeneous catalytic reaction,) which is located at the center of the transition region (r = $3/4V_{max}$) between the pseudo-first-ordered (r ≤ $1/2V_{max}$) and the pseudo-zero-ordered (r ≈ V_{max}) in Michaelis–Menten plot, then accurate estimates of kinetics for immobilized enzymes can still be achieved. For this case, considering an iterative scheme, we can rearrange eq (1) as eq (4) and eq (5), and combine them to set up the following set of equations.

$$\begin{cases} < \frac{V_{\max}^*}{H} >_{\mathrm{r}} = \frac{1}{\tau}\{- < K_m^* >_{\mathrm{r-1}} Ln(1-\alpha_\tau) + [S]_{o,H}\,\alpha_\tau\} & (4) \\ < \frac{V_{\max}^*}{H} >_{\mathrm{r}}\ \tau - [S]_{o,L}\,\alpha_\tau = - < K_m^* >_{\mathrm{r}} Ln(1-\alpha_\tau) & (5) \end{cases}$$

where r = 1, 2, 3, …, and $< K_m^* >_0$ obtained by eq (3) as the initial approximation for eq (4). For optimum estimations of $\frac{V_{\max}^*}{H}$ and K_m^*, the detected values of α_τs in eq (4) and eq (5) are based on two measurement conditions—high inlet concentration of substrate, $[S]_{o,H}$, and low inlet concentration of substrate, $[S]_{o,L}$, respectively. In

brief, eq (4) is used to determine $\frac{V^*_{max}}{H}$ values concerning K^*_m effect, which is approximated in eq (5) for r ≥ 1; eq (5) is then used to calculate K^*_m approximates using $\frac{V^*_{max}}{H}$ values determined in eq (4). After successively finite computing, we will get converged values with required certain decimal places for $< \frac{V^*_{max}}{H} >_r$ and $< K^*_m >_r$, and these values are then the correct answer to satisfy eq (4) and eq (5).

As mentioned above, this method will fail or gain a large deviation from true value of kinetics when the highest available concentration of substrate is far lower than saturation (i.e., ≤ $3K_m$). This constraint is similar to the limitations of Michaelis–Menten plot to estimate the kinetic value of homogeneous catalytic reaction. The strategy of measurement and calculation is briefly outlined as Scheme A1, and has been used to analyze the kinetics of immobilized CRL-catalyzed reactions.

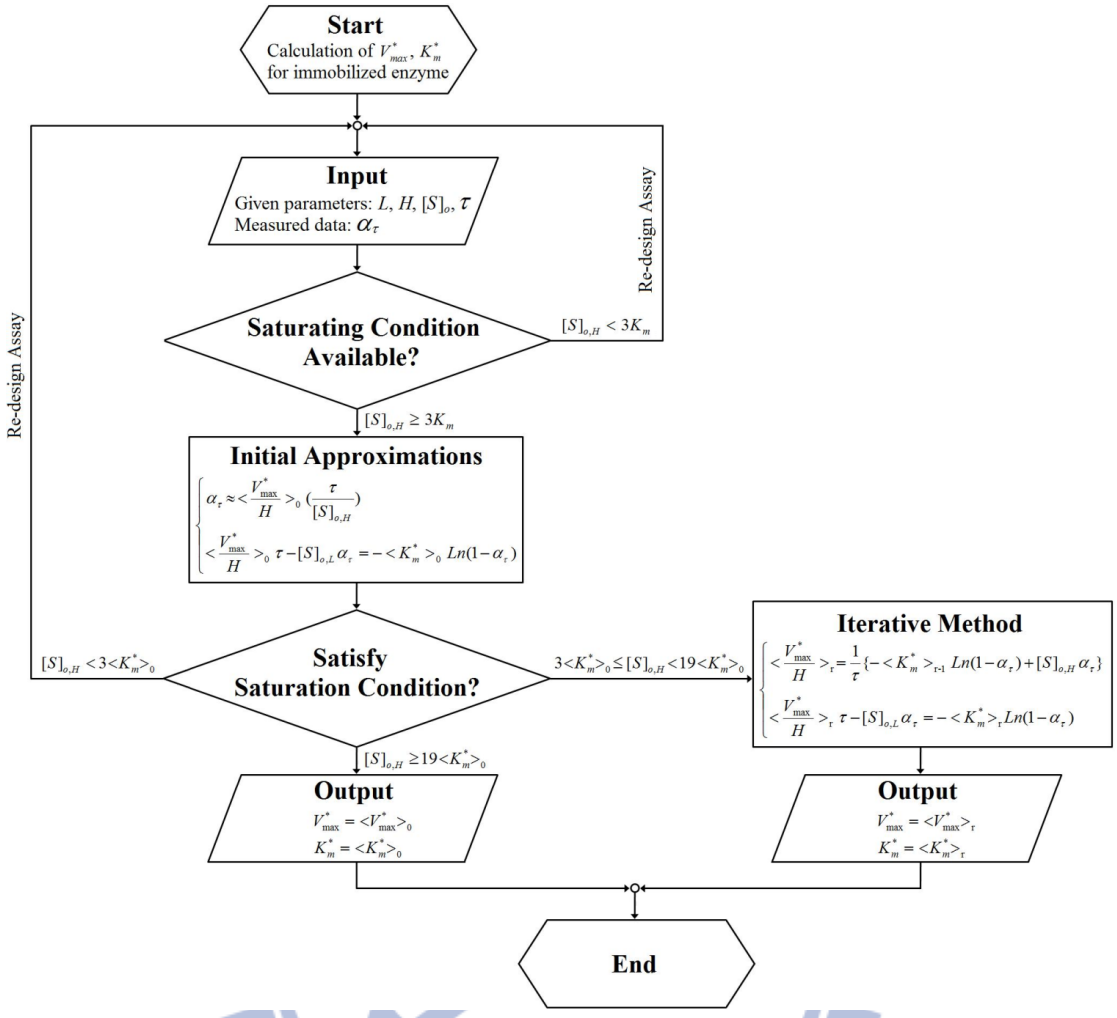

Scheme A1 Flow chart of data processing. It demonstrates the scheme for solving eq (1) to determine the apparent kinetics of immobilized enzyme.

Results and Discussion

Enzymatic Activities of Surface-Immobilized CRL Measured by Corresponding Controls. Figure A3 shows the typical time course plots of the *p*NP absorbance at the reactor outlet, after subtracting blank controls, responses to high/low feed concentration of substrate with a series of space times τs at 410 nm in CRL assays. The assay system, illustrated in Figure A2b, was set up with the respective blank controls (enzyme-free for CRL); the latter used a bypass stream to skip the reactor and go directly to the UV–Vis spectrophotometer. Because the absorbance of product *p*NP at high concentration of substrate *p*NPP (near the solubility limit) significantly

differed from that at low *p*NPP concentration, the bypass was an essential strategy to continuous-flow assay of surface-immobilized CRL in order to subtract accurate blank controls. We found the average background absorbance of 80 μM *p*NPP at 410 nm was 0.1033 larger than that of 4 μM *p*NPP.

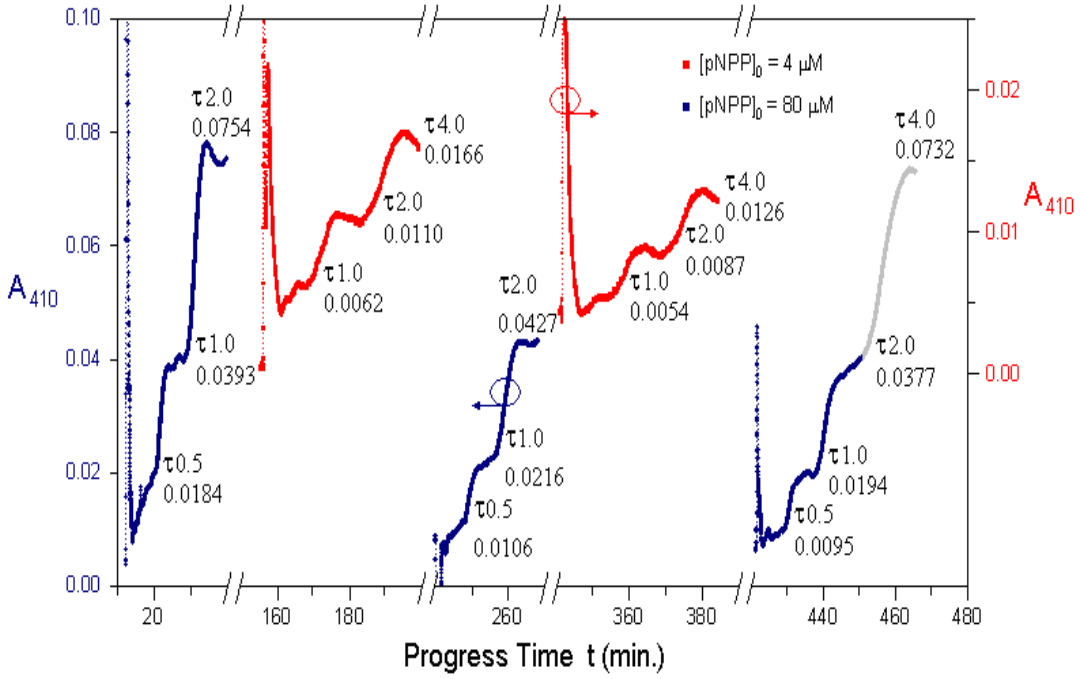

Figure A3 The typical progress curves of enzymatic assays for immobilized CRL. The absorbance of time courses was obtained after setting zero with no enzyme *via* a bypass in the CRL assay. The breaks in x-axis, progress time t, were due to bypass steps.

Immobilized CRL Kinetics: Iterating Scheme to Determine V^*_{max}/H, Corresponding Deactivation Curve, and K^*_m. Due to solubility limit of substrate *p*NPP in the immobilized CRL assay, 80 μM *p*NPP (about only 3.35 times the K_m of free CRL) was used as the inlet condition of high substrate concentration $[p\text{NPP}]_{o,H}$ to obtain the initial approximations of $< V^*_{max}/H >_0$, and the fitting curve of deactivation could be determined (as $< V^*_{max}/H >_0 = 1.236 + 1.758e^{-0.00717t}$ in Figure A4a) by eq (2). The $< V^*_{max}/H >_0$ values at any time t determined by this decay curve, space time τs = 1, 2, 4 min, and 4 μM *p*NPP as the inlet condition of low substrate concentration

$[p\text{NPP}]_{o,L}$ were then used to obtain the initial approximation of $< K^*_m >_0$ (= 16.21 μM in Figure A4b) from eq (3). Because the $[p\text{NPP}]_{o,H}$ used was only about 4.9 times the $< K^*_m >_0$, and apparently far from the criterion of pseudo-saturating condition (at least 19 times the $< K^*_m >_0$); it must further apply the route of iterative method, as shown in Scheme A1, to get more accurate approximations for V^*_{max}/H and K^*_m. Substituting the initial estimations (r = 0) into the set of iterating eqs (4) and (5), the converged results of immobilized CRL were calculated, through five successive approximations shown in Figure A4a and A4b, as follows: the deactivation curve $\frac{V^*_{\max}}{H} = 1.603 + 2.226e^{-0.007047t}$ with R^2 = 0.9854, the original V^*_{max}/H = 3.83 μM/min (or $V^*_{max} = 6.41\times10^3$ s^{-1} μm^{-2}), and average K^*_m = 22.60 ± 1.41 μM in Figure A4c.

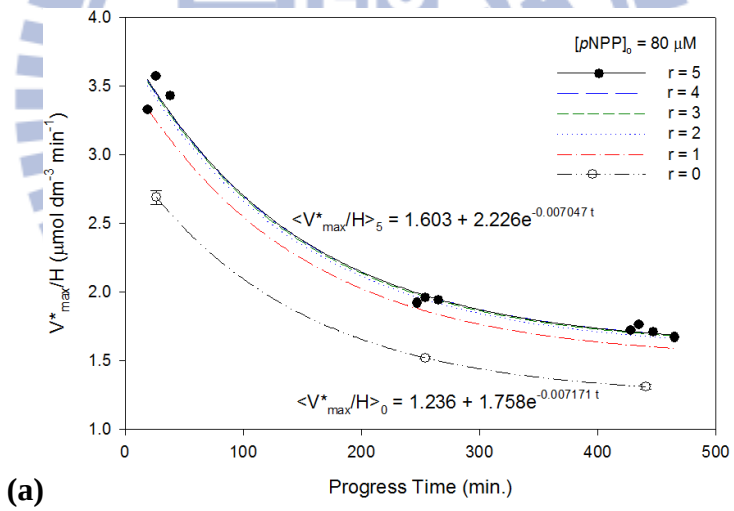

(a)

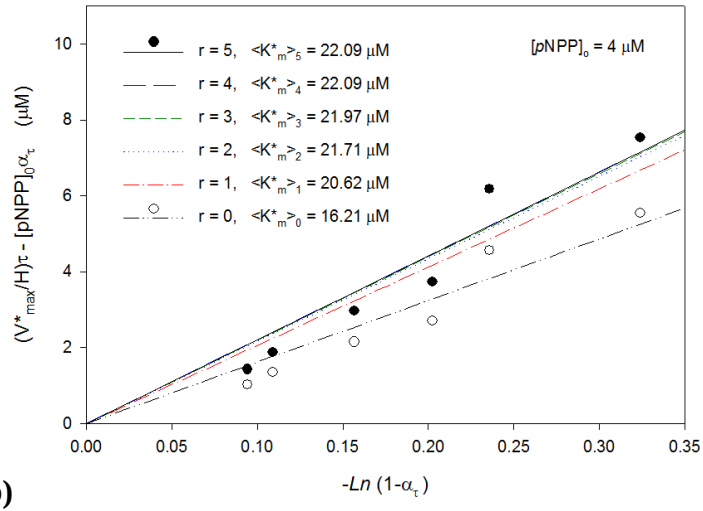

(b)

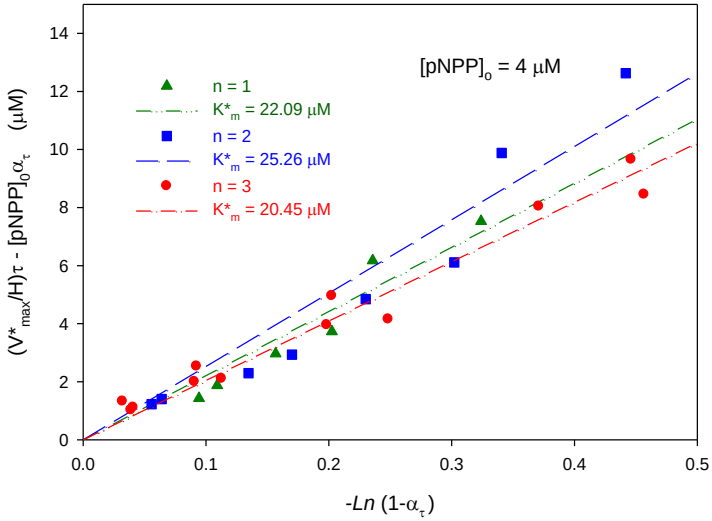

(c)

Figure A4 Plots of surface-immobilized CRL kinetic data. The typical plots (a) and (b) show the iterative fitting process operated by the set of eqs (4) and (5), respectively. (a) For the solubility limit of substrate *p*NPP in the CRL assay, the initial approximation $<V^*_{max}/H>_0$ (open symbol) were still obtained from eq (2) by linear regression using $[p\text{NPP}]_{o,H}$ = 80 μM, and fitted to the exponential decay curve (dash-dot-dot). Fitting curves r = 1–5 were corresponding to the five successive approximations of eq (4); the solid symbol means the converged value of V^*_{max}/H with four significant figures. In fact, the fitting curves r = 1 and r = 5 converged to one curve. (b) The open symbol and solid symbol represent the initial and the fifth approximations of eqs (3) and (5) by linear regression, respectively. The value of K^*_m of immobilized CRL has converged to 22.09 μM with four significant figures after five successive approximation (r = 1–5). (c) The predicted K^*_m values, the slopes of regression lines fitting lines in eq (5), of immobilized CRL are the result of three set of independent experiment data (n = 1–3).

II. Dimension of the Enzyme CRL

According to the Protein Data Base, the unit cell of crystallized *Candida rugosa* lipase, CRL (ID:1GZ7),[136,137] has the following parameters: a = 6.115 nm, b = 9.114 nm, c = 10.846 nm; $\alpha = 90.78^{o}$, $\beta = 106.31^{o}$, $\gamma = 86.91^{o}$ for chains: 4. One can roughly estimate the mean diameter D of the unit CRL (D_{CRL}) as:

$$\frac{\pi}{6}D^3 \leq (\text{Volume}) = (a\sin\alpha \times b\sin\beta \times c\sin\gamma)$$

Therefore, we obtained:

$$D_{CRL} \leq \left[\frac{6}{\pi}(\text{Volume})\right]^{1/3} = \left[\frac{6}{\pi}(a\sin\alpha \times b\sin\beta \times c\sin\gamma)\right]^{1/3}$$

then $D_{CRL} \leq 10.34$ nm or $r_{CRL} \leq 5.17$ nm

III. Dimension of the Substrate *p*NPP

V_A is the molal volume of solute at normal boiling point, in cm^3/g. Table A1 lists the contributions for each of the constituent atoms; these values can be added together, with deducted specific ring corrections as per solute molecular formulae, to predict V_A.

Table A1 Atomic and structural diffusion volume increments[138,139]

Element		Atomic volume, in cm^3/mol	Element		Atomic volume, in cm^3/mol
Antimony (Sb)		24.2	Oxygen (O)	double-bonded	7.4
Arsenic (As)		30.5		coupled to two other elements:	
Bismuth (Bi)		48.0		in aldehydes and ketones	7.4
Bromine (Br)		27.0		in methyl esters	9.1
Carbon (C)		14.8		in ethyl esters	9.9
Chlorine (Cl)	terminal, as in R-Cl	21.6		in higher esters and ethers	11.0
	medial, as in R-CHCl-R'	24.6		in acids	12.0
Chromium (Cr)		27.4		in union with S, P, N	8.3
Fluorine (F)		8.7	Phosphorus (P)		27.0
Germanium (Ge)		34.5	Silicon (Si)		32.0
Hydrogen (H)		3.7	Sulfur (S)		25.6
Iodine (I)		37.0	Tin (Sn)		42.3
Nitrogen (N)	double-bonded R-N=R'	15.6	Titanium (Ti)		35.7
	in primary amines R-NH_2	10.5	Vanadium (V)		32.0
	in secondary amines R-NH-R'	12.0	Zinc (Zn)		20.4

For a three-membered ring, as in ethylene oxide	deduct	6.0
For a four-membered ring, as in cyclobutane	deduct	8.5
For a five-membered ring, as in furane	deduct	11.5
For a six-membered ring, as in benzene, pyridine	deduct	15.0
For an anthracene ring formation	deduct	47.5
For a naphthalene ring formation	deduct	30.0

The molecular volume of *p*NPP may be evaluated by using values from Table A1 as follows:

$$V_{pNPP}$$

$$= 22V_C + 35V_H + 1V_N + 4V_O - (\text{Ring Factor})$$

$$= 22 \times (14.8) + 35 \times (3.7) + 1 \times (15.6) + (3 \times 7.4 + 11) - (15.0)$$

$$= 488.9\ cm^3/mol$$

$$= 0.8121\ nm^3/molecule$$

Therefore, we can calculate the diameter D of the substrate *p*NPP (D_{pNPP}) as:

$$\frac{\pi}{6}D^3 \approx (\text{Volume})$$

$$D_{pNPP} \approx \left[\frac{6}{\pi}(\text{Volume})\right]^{1/3} = 1.158\ nm \text{ or } r_{pNPP} = 0.5788\ nm$$

Curriculum Vitae

C H U N G - S H U W U

Department of Materials Science and Engineering, National Chiao Tung University,

1001 University Road, Hsinchu, Taiwan 300, ROC

Phone +886-3-571-2121#55809

E-mail dreaminblue.nano95g@nctu.edu.tw

I. EDUCATION

Ph.D., National Chiao Tung University, Hsinchu, Taiwan,
2008–2011 (Department of Materials Science and Engineering)

M.S., National Chiao Tung University, Hsinchu, Taiwan,
2006–2008 (Institute of Nanotechnology)

B.S., National Sun Yat-sen University, Kaohsiung, Taiwan,
2002–2006 (Department of Biological Science)

II. SKILLS

Nanoparticles Science, Nanobiotechnology

III. PUBLICATION LIST

1. Chung-Shu Wu, Cheng-Che Lee, Chia-Tien Wu, Yuh-Shyong Yang, Fu-Hsiang Ko, Size-Modulated Catalytic Activity of Enzyme–Nanoparticle Conjugates: A Combined Kinetic and Theoretical Study. *Chemical Communications* **2011**, *47*, 7446–7448. (The first author) (IF: 5.787) (Collection Listing on ***Global Medical Discovery Website*** at Jun. 25, 2011)

2. Jagan Singh Meena, Min-Ching Chu, Chung-Shu Wu, Feng-Chih Chang, Fu-Hsiang Ko, Highly Reliable Si_3N_4-HfO_2 Stacked Heterostructure to Fully Flexible Poly-(3-hexylthiophene) Thin-Film Transistor. *Organic Electronics* **2011**, *12*, 1414–1421. (The third author) (IF: 3.998)

3. Jagan Singh Meena, Min-Ching Chu, Chung-Shu Wu, Srikanth Ravipati, Fu-Hsiang Ko, Environmentally Stable Flexible Metal–Insulator–Metal Capacitors Using Zirconium-Silicate and Hafnium-Silicate Thin Film Composite Materials as Gate Dielectrics. *Journal of Nanoscience and Nanotechnology* **2011**, *11*, XX–XX. (The third author) (IF: 1.351) (Manuscript Accepted)

4. Chung-Shu Wu, Fu-Ken Liu, Fu-Hsiang Ko, Potential Role of Gold Nanoparticles for Improved Analytical Methods: An Introduction to Characterizations and Applications. *Analytical and Bioanalytical Chemistry* **2011**, *399*, 103–118. (The first author) (IF: 3.841)

5. Chia-Tien Wu, Chun-Hung Lin, Chieh Cheng, Chung-Shu Wu, Huai-Chen Ting, Feng-Chih Chang, Fu-Hsiang Ko, Design of Artificial Hollow Moth-Eye Structures Using Anodic Nanocones for High-Performance Optics. *Chemistry of Materials* **2010**, *22*, 6583–6589. (The fourth author) (IF: 6.397)

6. Jitendra N. Tiwari, Jagan Singh Meena, Chung-Shu Wu, Rajanish N. Tiwari, Min-Ching Chu, Feng-Chih Chang, Fu-Hsiang Ko, Thin-Film Composite Materials as a Dielectric Layer for Flexible Metal–Insulator–Metal Capacitors. *ChemSusChem* **2010**, *3*, 1051–1056. (The third author) (IF: 6.325)

7. Chie-Chieh Lin, Fu-Hsiang Ko, Chun-Chi Chen, Yuh-Shyong Yang, Feng-Chi Chang, Chung-Shu Wu, Miniaturized Metal Semiconductor Metal Photocurrent System for Biomolecular Sensing *via* Chemiluminescence. *Electrophoresis* **2009**, *30*, 3189–3197. (The sixth author) (IF: 3.569)

8. Chung-Shu Wu, Chia-Tien Wu, Yuh-Shyong Yang, Fu-Hsiang Ko, An Enzymatic Kinetics Investigation into the Significantly Enhanced Activity of Functionalized Gold Nanoparticles. *Chemical Communications* **2008**, 5327–5329. (The first author) (IF: 5.787)

統計類別（年度）	**2008**		**2009**		**2010**		**2011**	
	篇數	IF 總合	篇數	IF 總合	篇數	IF 總合	篇數	IF 總合
所有 SCI 論文（含共同作者）	**1**	**5.787**	**1**	**3.569**	**2**	**12.722**	**4**	**14.977**
SCI 論文（限第一作者）	**1**	**5.787**	**0**	**0**	**0**	**0**	**2**	**9.628**

IV. CONFERENCES

International:

1. Fu-Hsiang Ko, Chung-Shu Wu, Chi-Chang Wu, Nanostructural Devices for Biomolecule Detection. Villa Conference on Interactions Among Nanostructures (VCIAN), Las Vegas, Nevada, USA, Apr. 21–25, **2011**. (The second author) (Oral)

2. Chung-Shu Wu, Chia-Tien Wu, Chieh Chen, Chung-Chih Huang, Yu-Lin Yeh, Yuh-Shyong Yang, Fu-Hsiang Ko, Catalytic Behaviors in Modulating Enzymatic Activity through Different-Sized Gold Nanoparticles. IEEE International NanoElectronics Conference (INEC), Hong Kong, Jan. 3–8, **2010**. (The first author) (Oral)

3. Chieh Chen, Chia-Tien Wu, Yi-Sheng Wei, Chung-Shu Wu, Fu-Hsiang Ko, Honeycombed Indium Oxide Nanostructure for Gas Sensing by Sol–Gel Process. Micro & Nano Engineering (MNE), Greece, Sep. 15–18, **2008**. (The fourth author) (Poster)

4. Chung-Shu Wu, Chia-Tien Wu, Chieh Chen, Yuh-Shyong Yang, Fu-Hsiang Ko, An Enzymatic Kinetics Investigation into the Significantly Enhanced Activity of Functionalized Gold Nanoparticles. Micro & Nano Engineering (MNE), Greece, Sep. 15–18, **2008**. (The first author) (Poster)

Domestic:

1. Yu-Ling Yeh, Chung-Shu Wu, Chung-Chih Huang, Fu-Hsiang Ko, A Rapid and Cost-Effective Sensor-Based Lateral Flow Assay Method for the Detection of Mercury Ion using DNA Modified Gold Nanoparticle. 17th Analytical Chemistry Conference, NCHU (Taichung & Nantou), Taiwan, May 14–15, **2011**. (The second author) (Oral)

2. Chung-Shu Wu, Cheng-Che Lee, Chia-Tien Wu, Chung-Chih Huang, Fu-Hsiang Ko, Analysis of Size-Modulated Catalytic Activity of Enzyme–Nanoparticle Conjugates: A Combined Kinetic and Theoretical Study. 17th Analytical Chemistry Conference, NCHU (Taichung & Nantou), Taiwan, May 14–15, **2011**. (The first author) (Oral)

3. Chung-Shu Wu, Chung-Chih Huang, Chia-Tien Wu, Yu-Lin Yeh, Fu-Hsiang Ko, A Rapid and Portable Sensor Based on Protein Protected Gold Nanoparticle Probe and Lateral Flow Assay for Naked Eye Detection of Mercury Ion. Research Week-International Symposium 2011 of COM, TMU (Taipei), Taiwan, Mar. 26–27, **2011**. (The first author) (Poster)

4. Chung-Shu Wu, Chia-Tien Wu, Chieh Chen, Chung-Chih Huang, Yuh-Shyong Yang, Fu-Hsiang Ko, Analysis of Enzymatic Activity and Kinetics through the Linker-Free Gold Nanoparticle Pathway. 15th Analytical Chemistry Conference, NCCU (Chiayi), Taiwan, May 16, **2009**. (The first author) (Oral)

5. Chung-Shu Wu, Chia-Tien Wu, Chieh Chen, Yuh-Shyong Yang, Fu-Hsiang Ko, An Enzymatic Kinetics Investigation into the Significantly Enhanced Activity of Functionalized Gold Nanoparticles. Annual Chinese Chemical Society, NCUE (Changhua), Taiwan, Dec. 05–07, **2008**. (The first author) (Award) (Oral)

6. Chung-Shu Wu, Chia-Tien Wu, Chieh Chen, Yuh-Shyong Yang, Fu-Hsiang Ko, Analysis of Enzymatic Activity and Kinetics through the Linker-Free Gold Nanoparticle Pathway. International Chemical Conference Taipei (ICCT), NSYSU (Kaohsiung), Taiwan, Oct. 03–05, **2008**. (The first author) (Oral)

About Global Medical Discovery

Global Medical Discovery service (http://globalmedicaldiscovery.com/) alerts the scientific community to breaking journal articles considered to be of importance to the medical discovery process. Global Medical Discovery is viewed almost 80,000 times each month by their audience of academic and industrial R&D personnel and it is featured on the intranets of a growing number of the top 20 pharmaceutical companies and major academic institutions. Publications featured by Global Medical Discovery gain extensive exposure that helps advance medical discovery and optimize drug development. This exposure also has the added benefit of encouraging industrial funding and licensing.

Global Medical Discovery Objectives:

The objectives of Global Medical Discovery are:

1. To offer readers the depth and breadth of breaking news about the latest scientific discoveries.

2. To provide a medium through which ideas and conventions get challenged regularly, where innovative ideas and new ways of thinking emerge, helping to create a highly competent and attractive world-class work force in academia and pharmaceutical industry.

3. To promote the status of talented scientists and industry experts in the International academic and pharmaceutical industry scene.

4. To provide a forum for free and open exchanges of ideas, information, and experiences concerning scientific matters. To meet these objectives, the activities of Global Medical Discovery include publishing subjects of interest with special focus on Key published scientific articles, Key patents and licensing opportunities, top events and conferences in science and medicine and other technology issues.

– Our recent work (*Chem. Commun.* **2011**, *47*, 7446–7448) was selected to list on ***Global Medical Discovery Website*** at Jun. 25, 2011.

References and Bibliography

[1] Rosi, N. L., and Mirkin, C. A. Nanostructures in biodiagnostics. *Chem. Rev.* **2005**, *105*, 1547–1562.

[2] Eustis, S., and El-Sayed, M. A. Why gold nanoparticles are more precious than pretty gold: Noble metal surface plasmon resonance and its enhancement of the radiative and nonradiative properties of nanocrystals of different shapes. *Chem. Soc. Rev.* **2006**, *35*, 209–217.

[3] Shipway, A. N., Katz, E., and Willner, I. Nanoparticle arrays on surfaces for electronic, optical, and sensor applications. *ChemPhysChem* **2000**, *1*, 18–52.

[4] Willard, D. M. Nanoparticles in bioanalytics. *Anal. Bioanal. Chem.* **2003**, *376*, 284–286.

[5] Boisselier, E., and Astruc, D. Gold nanoparticles in nanomedicine: Preparations, imaging, diagnostics, therapies and toxicity. *Chem. Soc. Rev.* **2009**, *38*, 1759–1782.

[6] Niemeyer, C. M. Nanoparticles, proteins, and nucleic acids: Biotechnology meets materials science. *Angew. Chem. Int. Ed.* **2001**, *40*, 4128–4158.

[7] Whitesides, G. M., Mathias, J. P., and Seto, C. T. Molecular self-assembly and nanochemistry: A chemical strategy for the synthesis of nanostructures. *Science* **1991**, *254*, 1312–1319.

[8] Maxwell, D. J., Taylor, J. R., and Nie, S. M. Self-assembled nanoparticle probes for recognition and detection of biomolecules. *J. Am. Chem. Soc.* **2002**, *124*, 9606–9612.

[9] Xu, X. X., Liu, S. Q., and Ju, H. X. A novel hydrogen peroxide sensor *via* the direct electrochemistry of horseradish peroxidase immobilized on colloidal gold modified screen-printed electrode. *Sensors* **2003**, *3*, 350–360.

[10] Park, S. J., Taton, T. A., and Mirkin, C. A. Array-based electrical detection of DNA with nanoparticle probes. *Science* **2002**, *295*, 1503–1506.

[11] Bhattacharya, R., Mukherjee, P., Xiong, Z., Atala, A., Soker, S., and Mukhopadhyay, D. Gold nanoparticles inhibit VEGF165-induced proliferation of HUVEC cells. *Nano Lett.* **2004**, *4*, 2479–2481.

[12] Elghanian, R., Storhoff, J. J., Mucic, R. C., Letsinger, R. L., and Mirkin, C. A. Selective colorimetric detection of polynucleotides based on the distance-dependent optical properties of gold nanoparticles. *Science* **1997**, *277*, 1078–1081.

[13] Kanaras, A. G., Wang, Z. X., Bates, A. D., Cosstick, R., and Brust, M. Towards multistep nanostructure synthesis: Programmed enzymatic self-assembly of DNA/gold systems. *Angew. Chem. Int. Edit.* **2003**, *42*, 191–194.

[14] Kanaras, A. G., Wang, Z. X., Brust, M., Cosstick, R., and Bates, A. D. Enzymatic disassembly of DNA–gold nanostructures. *Small* **2007**, *3*, 590–594.

[15] Alivisatos, P. The use of nanocrystals in biological detection. *Nat. Biotechnol.* **2004**, *22*, 47–52.

[16] Ginger, D. S., Zhang, H., and Mirkin, C. A. The evolution of dip-pen nanolithography. *Angew. Chem. Int. Ed.* **2004**, *43*, 30–45.

[17] Liu, M. Z., Amro, N. A., Chow, C. S., and Liu, G. Y. Production of nanostructures of DNA on surfaces. *Nano Lett.* **2002**, *2*, 863–867.

[18] Kenseth, J. R., Harnisch, J. A., Jones, V. W., and Porter, M. D. Investigation of approaches for the fabrication of protein patterns by scanning probe lithography. *Langmuir* **2001**, *17*, 4105–4112.

[19] Alivisatos, A. P., Johnsson, K. P., Peng, X. G., Wilson, T. E., Loweth, C. J., Bruchez, M. P., and Schultz, P. G. Organization of 'nanocrystal molecules' using DNA. *Nature* **1996**, *382*, 609–611.

[20] Liu, G. L., Yin, Y. D., Kunchakarra, S., Mukherjee, B., Gerion, D., Jett, S. D., Bear, D. G., Gray, J. W., Alivisatos, A. P., Lee, L. P., and Chen, F. Q. F. A nanoplasmonic molecular ruler for measuring nuclease activity and DNA footprinting. *Nat. Nanotechnol.* **2006**, *1*, 47–52.

[21] Welch, C. W., and Compton, R. G. The use of nanoparticles in electroanalysis: A review. *Anal. Bioanal. Chem.* **2006**, *384*, 601–619.

[22] Daniel, M. C., and Astruc, D. Gold nanoparticles: Assembly, supramolecular chemistry, quantum-size-related properties, and applications toward biology, catalysis, and nanotechnology. *Chem. Rev.* **2004**, *104*, 293–346.

[23] Gao, X. H., Cui, Y. Y., Levenson, R. M., Chung, L. W. K., and Nie, S. M. In vivo cancer targeting and imaging with semiconductor quantum dots. *Nat. Biotechnol.* **2004**, *22*, 969–976.

[24] Katz, E., and Willner, I. Integrated nanoparticle–biomolecule hybrid systems: Synthesis, properties, and applications. *Angew. Chem. Int. Ed.* **2004**, *43*, 6042–6108.

[25] Baron, R., Willner, B., and Willner, I. Biomolecule–nanoparticle hybrids as functional units for nanobiotechnology. *Chem. Commun.* **2007**, 323–332.

[26] De, M., Ghosh, P. S., and Rotello, V. M. Applications of nanoparticles in biology. *Adv. Mater.* **2008**, *20*, 4225–4241.

[27] Bunz, U. H. F., and Rotello, V. M. Gold nanoparticle–fluorophore complexes: Sensitive and discerning "noses" for biosystems sensing. *Angew. Chem. Int. Ed.* **2010**, *49*, 3268–3279.

[28] Ferrari, M. Cancer nanotechnology: Opportunities and challenges. *Nat. Rev. Cancer* **2005**, *5*, 161–171.

[29] Jonkheijm, P., Weinrich, D., Schroder, H., Niemeyer, C. M., and Waldmann, H. Chemical strategies for generating protein biochips. *Angew. Chem. Int. Ed.* **2008**, *47*, 9618–9647.

[30] Parak, W. J., Gerion, D., Pellegrino, T., Zanchet, D., Micheel, C., Williams, S. C., Boudreau, R., Le Gros, M. A., Larabell, C. A., and Alivisatos, A. P. Biological applications of colloidal nanocrystals. *Nanotechnology* **2003**, *14*, R15–R27.

[31] Chen, T., Shukoor, M. I., Chen, Y., Yuan, Q. A., Zhu, Z., Zhao, Z. L., Gulbakan, B., and Tan, W. H. Aptamer-conjugated nanomaterials for bioanalysis and biotechnology applications. *Nanoscale* **2011**, *3*, 546–556.

[32] Tsai, C. Y., Chang, T. L., Uppala, R., Chen, C. C., Ko, F. H., and Chen, P. H. Electrical detection of protein using gold nanoparticles and nanogap electrodes. *Jpn. J. Appl. Phys.* **2005**, *44*, 5711–5716.

[33] Tsai, C. Y., Chang, T. L., Chen, C. C., Ko, F. H., and Chen, P. H. An ultra sensitive DNA detection by using gold nanoparticle multilayer in nano-gap electrodes. *Microelectron. Eng.* **2005**, *78–79*, 546–555.

[34] Liu, R. R., Liew, R. S., Zhou, H., and Xing, B. G. A simple and specific assay for real-time colorimetric visualization of β-lactamase activity by using gold nanoparticles. *Angew. Chem. Int. Ed.* **2007**, *46*, 8799–8803.

[35] Cui, Y., Wei, Q. Q., Park, H. K., and Lieber, C. M. Nanowire nanosensors for highly sensitive and selective detection of biological and chemical species. *Science* **2001**, *293*, 1289–1292.

[36] Huang, G. S., Chen, Y. S., and Yeh, H. W. Measuring the flexibility of immunoglobulin by gold nanoparticles. *Nano Lett.* **2006**, *6*, 2467–2471.

[37] Bhattacharya, R., Patra, C. R., Verma, R., Kumar, S., Greipp, P. R., and Mukherjee, P. Gold nanoparticles inhibit the proliferation of multiple myeloma cells. *Adv. Mater.* **2007**, *19*, 711–716.

[38] LaVan, D. A., McGuire, T., and Langer, R. Small-scale systems for in vivo drug delivery. *Nat. Biotechnol.* **2003**, *21*, 1184–1191.

[39] Sarikaya, M., Tamerler, C., Jen, A. K. Y., Schulten, K., and Baneyx, F. Molecular biomimetics: Nanotechnology through biology. *Nat. Mater.* **2003**, *2*, 577–585.

[40] Hostetler, M. J., Wingate, J. E., Zhong, C. J., Harris, J. E., Vachet, R. W., Clark, M. R., Londono, J. D., Green, S. J., Stokes, J. J., Wignall, G. D., Glish, G. L., Porter, M. D., Evans, N. D., and Murray, R. W. Alkanethiolate gold cluster molecules with core diameters from 1.5 to 5.2 nm: Core and monolayer

properties as a function of core size. *Langmuir* **1998**, *14*, 17–30.

[41] Verma, A., and Rotello, V. M. Surface recognition of biomacromolecules using nanoparticle receptors. *Chem. Commun.* **2005**, 303–312.

[42] Wilson, R. The use of gold nanoparticles in diagnostics and detection. *Chem. Soc. Rev.* **2008**, *37*, 2028–2045.

[43] Hanefeld, U., Gardossi, L., and Magner, E. Understanding enzyme immobilisation. *Chem. Soc. Rev.* **2009**, *38*, 453–468.

[44] Wu, C. S., Liu, F. K., and Ko, F. H. Potential role of gold nanoparticles for improved analytical methods: An introduction to characterizations and applications. *Anal. Bioanal. Chem.* **2011**, *399*, 103–118.

[45] Katz, E., Sheeney-Haj-Ichia, L., and Willner, I. Electrical contacting of glucose oxidase in a redox-active rotaxane configuration. *Angew. Chem. Int. Ed.* **2004**, *43*, 3292–3300.

[46] Wang, Z. X., and Ma, L. N. Gold nanoparticle probes. *Coord. Chem. Rev.* **2009**, *253*, 1607–1618.

[47] Murphy, C. J., Gole, A. M., Stone, J. W., Sisco, P. N., Alkilany, A. M., Goldsmith, E. C., and Baxter, S. C. Gold nanoparticles in biology: Beyond toxicity to cellular imaging. *Accounts Chem. Res.* **2008**, *41*, 1721–1730.

[48] Cooper, E., and Leggett, G. J. Static secondary ion mass spectrometry studies of self-assembled monolayers: Influence of adsorbate chain length and terminal functional group on rates of photooxidation of alkanethiols on gold. *Langmuir* **1998**, *14*, 4795–4801.

[49] Castner, D. G., Hinds, K., and Grainger, D. W. X-ray photoelectron spectroscopy sulfur 2p study of organic thiol and disulfide binding interactions with gold surfaces. *Langmuir* **1996**, *12*, 5083–5086.

[50] Badwey, J. A., and Karnovsky, M. L. Active oxygen species and the functions of phagocytic leukocytes. *Annu. Rev. Biochem.* **1980**, *49*, 695–726.

[51] Wu, Z. C., Zhang, B., and Yan, B. Regulation of enzyme activity through interactions with nanoparticles. *Int. J. Mol. Sci.* **2009**, *10*, 4198–4209.

[52] Schmid, G. Large clusters and colloids. Metals in the embryonic state. *Chem. Rev.* **1992**, *92*, 1709–1727.

[53] Lewis, L. N. Chemical catalysis by colloids and clusters. *Chem. Rev.* **1993**, *93*, 2693–2730.

[54] Hornyak, G., Kroll, M., Pugin, R., Sawitowski, T., Schmid, G., Bovin, J. O., Karsson, G., Hofmeister, H., and Hopfe, S. Gold clusters and colloids in alumina nanotubes. *Chem.–Eur. J.* **1997**, *3*, 1951–1956.

[55] Xu, X. Y., Han, M. S., and Mirkin, C. A. A gold-nanoparticle-based real-time colorimetric screening method for endonuclease activity and inhibition. *Angew. Chem. Int. Ed.* **2007**, *46*, 3468–3470.

[56] Chen, S. W., Ingram, R. S., Hostetler, M. J., Pietron, J. J., Murray, R. W., Schaaff, T. G., Khoury, J. T., Alvarez, M. M., and Whetten, R. L. Gold nanoelectrodes of varied size: Transition to molecule-like charging. *Science* **1998**, *280*, 2098–2101.

[57] Miles, D. T., and Murray, R. W. Temperature-dependent quantized double layer charging of monolayer-protected gold clusters. *Anal. Chem.* **2003**, *75*, 1251–1257.

[58] Astruc, D., Lu, F., and Aranzaes, J. R. Nanoparticles as recyclable catalysts: The frontier between homogeneous and heterogeneous catalysis. *Angew. Chem. Int. Ed.* **2005**, *44*, 7852–7872.

[59] Guo, S. J., and Wang, E. K. Synthesis and electrochemical applications of gold nanoparticles. *Anal. Chim. Acta* **2007**, *598*, 181–192.

[60] Agasti, S. S., Rana, S., Park, M. H., Kim, C. K., You, C. C., and Rotello, V. M. Nanoparticles for detection and diagnosis. *Adv. Drug Deliv. Rev.* **2010**, *62*, 316–328.

[61] Rosi, N. L., Giljohann, D. A., Thaxton, C. S., Lytton-Jean, A. K. R., Han, M. S., and Mirkin, C. A. Oligonucleotide-modified gold nanoparticles for intracellular gene regulation. *Science* **2006**, *312*, 1027–1030.

[62] Jung, C., Chung, J. W., Kim, U. O., Kim, M. H., and Park, H. G. Real-time colorimetric detection of target DNA using isothermal target and signaling probe amplification and gold nanoparticle cross-linking assay. *Biosens. Bioelectron.* **2011**, *26*, 1953–1958.

[63] Lapienc, V., Kukolka, F., Kiko, K., Arndt, A., and Niemeyer, C. M. Conjugation of fluorescent proteins with DNA oligonucleotides. *Bioconjugate Chem.* **2010**, *21*, 921–927.

[64] Jain, P. K., Lee, K. S., El-Sayed, I. H., and El-Sayed, M. A. Calculated absorption and scattering properties of gold nanoparticles of different size, shape, and composition: Applications in biological imaging and biomedicine. *J. Phys. Chem. B* **2006**, *110*, 7238–7248.

[65] Mirkin, C. A., Letsinger, R. L., Mucic, R. C., and Storhoff, J. J. A DNA-based method for rationally assembling nanoparticles into macroscopic materials. *Nature* **1996**, *382*, 607–609.

[66] Reynolds, R. A., Mirkin, C. A., and Letsinger, R. L. Homogeneous, nanoparticle-based quantitative colorimetric detection of oligonucleotides. *J. Am. Chem. Soc.* **2000**, *122*, 3795–3796.

[67] Jin, R. C., Wu, G. S., Li, Z., Mirkin, C. A., and Schatz, G. C. What controls the melting properties of DNA-linked gold nanoparticle assemblies? *J. Am. Chem. Soc.* **2003**, *125*, 1643–1654.

[68] Lytton-Jean, A. K. R., and Mirkin, C. A. A thermodynamic investigation into the binding properties of DNA functionalized gold nanoparticle probes and molecular fluorophore probes. *J. Am. Chem. Soc.* **2005**, *127*, 12754–12755.

[69] Seferos, D. S., Giljohann, D. A., Hill, H. D., Prigodich, A. E., and Mirkin, C. A. Nano-flares: Probes for transfection and mRNA detection in living cells. *J. Am. Chem. Soc.* **2007**, *129*, 15477–15479.

[70] Zheng, D., Seferos, D. S., Giljohann, D. A., Patel, P. C., and Mirkin, C. A. Aptamer nano-flares for molecular detection in living cells. *Nano Lett.* **2009**, *9*, 3258–3261.

[71] Fischer, N. O., McIntosh, C. M., Simard, J. M., and Rotello, V. M. Inhibition of chymotrypsin through surface binding using nanoparticle-based receptors. *Proc. Natl. Acad. Sci. USA* **2002**, *99*, 5018–5023.

[72] Fischer, N. O., Verma, A., Goodman, C. M., Simard, J. M., and Rotello, V. M. Reversible "irreversible" inhibition of chymotrypsin using nanoparticle receptors. *J. Am. Chem. Soc.* **2003**, *125*, 13387–13391.

[73] You, C. C., Agasti, S. S., De, M., Knapp, M. J., and Rotello, V. M. Modulation of the catalytic behavior of alpha-chymotrypsin at monolayer-protected nanoparticle surfaces. *J. Am. Chem. Soc.* **2006**, *128*, 14612–14618.

[74] Fillon, Y., Verma, A., Ghosh, P., Ernenwein, D., Rotello, V. M., and Chmielewski, J. Peptide ligation catalyzed by functionalized gold nanoparticles. *J. Am. Chem. Soc.* **2007**, *129*, 6676–6677.

[75] Vertegel, A. A., Siegel, R. W., and Dordick, J. S. Silica nanoparticle size influences the structure and enzymatic activity of adsorbed lysozyme. *Langmuir* **2004**, *20*, 6800–6807.

[76] Maiti, S., Das, D., Shome, A., and Das, P. K. Influence of gold nanoparticles of varying size in improving the lipase activity within cationic reverse micelles. *Chem.–Eur. J.* **2010**, *16*, 1941–1950.

[77] Schmid, R. D., and Verger, R. Lipases: Interfacial enzymes with attractive applications. *Angew. Chem. Int. Ed.* **1998**, *37*, 1608–1633.

[78] ApplebaumBowden, D., Kobayashi, J., Kashyap, V. S., Brown, D. R., Berard, A., Meyn, S., Parrott, C., Maeda, N., Shamburek, R., Brewer, H. B., and SantamarinaFojo, S. Hepatic lipase gene therapy in hepatic lipase-deficient mice. Adenovirus-mediated replacement of a lipolytic enzyme to the vascular endothelium. *J. Clin. Invest.* **1996**, *97*, 799–805.

[79] Lalonde, J. J., Govardhan, C., Khalaf, N., Martinez, A. G., Visuri, K., and Margolin, A. L. Cross-linked crystals of *Candida rugosa* lipase: Highly efficient catalysts for the resolution of chiral esters. *J. Am. Chem. Soc.* **1995**, *117*, 6845–6852.

[80] Winkler, F. K., Darcy, A., and Hunziker, W. Structure of human pancreatic lipase. *Nature* **1990**, *343*, 771–774.

[81] Brady, L., Brzozowski, A. M., Derewenda, Z. S., Dodson, E., Dodson, G., Tolley, S., Turkenburg, J. P., Christiansen, L., Hugejensen, B., Norskov, L., Thim, L., and Menge, U. A serine protease triad forms the catalytic center of a triacylglycerol lipase. *Nature* **1990**, *343*, 767–770.

[82] Brzozowski, A. M., Derewenda, U., Derewenda, Z. S., Dodson, G. G., Lawson, D. M., Turkenburg, J. P., Bjorkling, F., Hugejensen, B., Patkar, S. A., and Thim, L. A model for interfacial activation in lipases from the structure of a fungal lipase-inhibitor complex. *Nature* **1991**, *351*, 491–494.

[83] Grochulski, P., Li, Y. G., Schrag, J. D., Bouthillier, F., Smith, P., Harrison, D., Rubin, B., and Cygler, M. Insights into interfacial activation from an open structure of *Candida rugosa* lipase. *J. Biol. Chem.* **1993**, *268*, 12843–12847.

[84] Schrag, J. D., and Cygler, M. 1.8 Å refined structure of the lipase from *Geotrichum candidum*. *J. Mol. Biol.* **1993**, *230*, 575–591.

[85] Derewenda, Z. S., and Derewenda, U. Relationships among serine hydrolases: Evidence for a common structural motif in triacylglyceride lipases and esterases. *Biochem. Cell Biol.* **1991**, *69*, 842–851.

[86] Turkevich, J., Stevenson, P. C., and Hillier, J. A study of the nucleation and growth processes in the synthesis of colloidal gold. *Discuss. Faraday Soc.* **1951**, *11*, 55–57.

[87] Frens, G. Controlled nucleation for the regulation of the particle size in monodispers gold suspensions. *Nature Phys. Sci.* **1973**, *241*, 20–22.

[88] Chen, C. C., Tsai, C. Y., Ko, F. H., Pun, C. C., Chen, H. L., and Chen, P. H. Room temperature operation of a coulomb blockade sensor fabricated by self-assembled gold nanoparticles using deoxyribonucleic acid hybridization. *Jpn. J. Appl. Phys.* **2004**, *43*, 3843–3848.

[89] Brennan, J. L., Hatzakis, N. S., Tshikhudo, T. R., Dirvianskyte, N., Razumas, V., Patkar, S., Vind, J., Svendsen, A., Nolte, R. J. M., Rowan, A. E., and Brust, M. Bionanoconjugation *via* click chemistry: The creation of functional hybrids of lipases and gold nanoparticles. *Bioconjugate Chem*. **2006**, *17*, 1373–1375.

[90] De Simone, G., Mandrich, L., Menchise, V., Giordano, V., Febbraio, F., Rossi, M., Pedone, C., and Manco, G. A substrate-induced switch in the reaction mechanism of a thermophilic esterase: Kinetic evidences and structural basis. *J. Biol. Chem.* **2004**, *279*, 6815–6823.

[91] Chen, W. T., Liu, M. C., and Yang, Y. S. Fluorometric assay for alcohol sulfotransferase. *Anal. Biochem.* **2005**, *339*, 54–60.

[92] You, C. C., Miranda, O. R., Gider, B., Ghosh, P. S., Kim, I. B., Erdogan, B., Krovi, S. A., Bunz, U. H. F., and Rotello, V. M. Detection and identification of proteins using nanoparticle–fluorescent polymer 'chemical nose' sensors. *Nat. Nanotechnol.* **2007**, *2*, 318–323.

[93] Mann, S., Shenton, W., Li, M., Connolly, S., and Fitzmaurice, D. Biologically programmed nanoparticle assembly. *Adv. Mater.* **2000**, *12*, 147–150.

[94] Brust, M., Fink, J., Bethell, D., Schiffrin, D. J., and Kiely, C. Synthesis and reactions of functionalized gold nanoparticles. *J. Chem. Soc. Chem. Commun.* **1995**, 1655–1656.

[95] Drechsler, U., Fischer, N. O., Frankamp, B. L., and Rotello, V. M. Highly efficient biocatalysts *via* covalent immobilization of *Candida rugosa* lipase on ethylene glycol-modified gold-silica nanocomposites. *Adv. Mater.* **2004**, *16*, 271–274.

[96] Gao, Y., Zhao, F., Wang, Q. G., Zhang, Y., and Xu, B. Small peptide nanofibers as the matrices of molecular hydrogels for mimicking enzymes and enhancing the activity of enzymes. *Chem. Soc. Rev.* **2010**, *39*, 3425–3433.

[97] Dyal, A., Loos, K., Noto, M., Chang, S. W., Spagnoli, C., Shafi, K. V. P. M., Ulman, A., Cowman, M., and Gross, R. A. Activity of *Candida rugosa* lipase immobilized on γ-Fe_2O_3 magnetic nanoparticles. *J. Am. Chem. Soc.* **2003**, *125*, 1684–1685.

[98] Manco, G., Mandrich, L., and Rossi, M. Residues at the active site of the esterase 2 from *Alicyclobacillus acidocaldarius* involved in substrate specificity and catalytic activity at high temperature. *J. Biol. Chem.* **2001**, *276*, 37482–37490.

[99] Weiner, H., Hu, J. H. J., and Sanny, C. G. Rate-limiting steps for the esterase and dehydrogenase reaction catalyzed by horse liver aldehyde dehydrogenase. *J. Biol. Chem.* **1976**, *251*, 3853–3855.

[100] Mendes, P. M., Jacke, S., Critchley, K., Plaza, J., Chen, Y., Nikitin, K., Palmer, R. E., Preece, J. A., Evans, S. D., and Fitzmaurice, D. Gold nanoparticle patterning of silicon wafers using chemical e-beam lithography. *Langmuir* **2004**, *20*, 3766–3768.

[101] Chithrani, B. D., Ghazani, A. A., and Chan, W. C. W. Determining the size and shape dependence of gold nanoparticle uptake into mammalian cells. *Nano Lett.* **2006**, *6*, 662–668.

[102] Joshi, H., Shirude, P. S., Bansal, V., Ganesh, K. N., and Sastry, M. Isothermal titration calorimetry studies on the binding of amino acids to gold nanoparticles. *J. Phys. Chem. B* **2004**, *108*, 11535–11540.

[103] Levy, R., Thanh, N. T. K., Doty, R. C., Hussain, I., Nichols, R. J., Schiffrin, D. J., Brust, M., and Fernig, D. G. Rational and combinatorial design of peptide capping ligands for gold nanoparticles. *J. Am. Chem. Soc.* **2004**, *126*, 10076–10084.

[104] Wei, H., Li, B. L., Li, J., Wang, E. K., and Dong, S. J. Simple and sensitive aptamer-based colorimetric sensing of protein using unmodified gold nanoparticle probes. *Chem. Commun.* **2007**, 3735–3737.

[105] Hermanson, G. T. *Bioconjugate Techniques*; Academic Press: New York, 1996; Chapter 14, pp. 594–596.

[106] Krauss, G. *Biochemistry of Signal Transduction and Regulation*; Wiley-VCH: Weinheim, 2001.

[107] Branden, C., and Tooze, J. *Introduction to Protein Structure*, 2nd ed.; Garland Publishing: New York, 1999; Chapter 12.

[108] Price, N. C., and Stevens, L. *Fundamentals of Enzymology: The Cell and Molecular Biology of Catalytic Proteins*, 3rd ed.; Oxford University Press: New York, 1999; pp. 347–355.

[109] Schoemaker, H. E., Mink, D., and Wubbolts, M. G. Dispelling the myths—biocatalysis in industrial synthesis. *Science* **2003**, *299*, 1694–1697.

[110] Cao, L. Q. Immobilised enzymes: Science or art? *Curr. Opin. Chem. Biol.* **2005**, *9*, 217–226.

[111] Wu, C. C., Ko, F. H., Yang, Y. S., Hsia, D. L., Lee, B. S., and Su, T. S. Label-free biosensing of a gene mutation using a silicon nanowire field-effect transistor. *Biosens. Bioelectron.* **2009**, *25*, 820–825.

[112] Kaar, J. L., Jesionowski, A. M., Berberich, J. A., Moulton, R., and Russell, A. J. Impact of ionic liquid physical properties on lipase activity and stability. *J. Am. Chem. Soc.* **2003**, *125*, 4125–4131.

[113] Lim, I. I. S., Mott, D., Engelhard, M. H., Pan, Y., Kamodia, S., Luo, J., Njoki, P. N., Zhou, S. Q., Wang, L. C., and Zhong, C. J. Interparticle chiral recognition of enantiomers: A nanoparticle-based regulation strategy. *Anal. Chem.* **2009**, *81*, 689–698.

[114] Yang, Z. M., Ho, P. L., Liang, G. L., Chow, K. H., Wang, Q. G., Cao, Y., Guo, Z. H., and Xu, B. Using beta-lactamase to trigger supramolecular hydrogelation. *J. Am. Chem. Soc.* **2007**, *129*, 266–267.

[115] Gao, Y., Kuang, Y., Guo, Z. F., Guo, Z. H., Krauss, I. J., and Xu, B. Enzyme-instructed molecular self-assembly confers nanofibers and a supramolecular hydrogel of taxol derivative. *J. Am. Chem. Soc.* **2009**, *131*, 13576–13577.

[116] DeLouise, L. A., and Miller, B. L. Enzyme immobilization in porous silicon: Quantitative analysis of the kinetic parameters for glutathione-*S*-transferases. *Anal. Chem.* **2005**, *77*, 1950–1956.

[117] Lee, C. C., Chiang, H. P., Li, K. L., Ko, F. H., Su, C. Y., and Yang, Y. S. Surface reaction limited model for the evaluation of immobilized enzyme on planar surfaces. *Anal. Chem.* **2009**, *81*, 2737–2744.

[118] Joshi, P. P., Merchant, S. A., Wang, Y. D., and Schmidtke, D. W. Amperometric biosensors based on redox polymer–carbon nanotube–enzyme composites. *Anal. Chem.* **2005**, *77*, 3183–3188.

[119] Zhang, B., Xing, Y. H., Li, Z. W., Zhou, H. Y., Mu, Q. X., and Yan, B. Functionalized carbon nanotubes specifically bind to α-chymotrypsin's catalytic site and regulate its enzymatic function. *Nano Lett.* **2009**, *9*, 2280–2284.

[120] Jia, H. F., Zhu, G. Y., and Wang, P. Catalytic behaviors of enzymes attached to nanoparticles: The effect of particle mobility. *Biotechnol. Bioeng.* **2003**, *84*, 406–414.

[121] Shukoor, M. I., Natalio, F., Therese, H. A., Tahir, M. N., Ksenofontov, V., Panthofer, M., Eberhardt, M., Theato, P., Schroder, H. C., Muller, W. E. G., and Tremel, W. Fabrication of a silica coating on magnetic γ-Fe_2O_3 nanoparticles by an immobilized enzyme. *Chem. Mater.* **2008**, *20*, 3567–3573.

[122] Samanta, B., Yang, X. C., Ofir, Y., Park, M. H., Patra, D., Agasti, S. S., Miranda, O. R., Mo, Z. H., and Rotello, V. M. Catalytic microcapsules assembled from enzyme–nanoparticle conjugates at oil-water interfaces. *Angew. Chem. Int. Ed.* **2009**, *48*, 5341–5344.

[123] You, C. C., Verma, A., and Rotello, V. M. Engineering the nanoparticle–biomacromolecule interface. *Soft Matter* **2006**, *2*, 190–204.

[124] Wang, Z. X., Kanaras, A. G., Bates, A. D., Cosstick, R., and Brust, M. Enzymatic DNA processing on gold nanoparticles. *J. Mater. Chem.* **2004**, *14*, 578–580.

[125] Hong, R., Fischer, N. O., Verma, A., Goodman, C. M., Emrick, T., and Rotello, V. M. Control of protein structure and function through surface recognition by tailored nanoparticle scaffolds. *J. Am. Chem. Soc.* **2004**, *126*, 739–743.

[126] Hong, R., Emrick, T., and Rotello, V. M. Monolayer-controlled substrate selectivity using noncovalent enzyme–nanopartide conjugates. *J. Am. Chem. Soc.* **2004**, *126*, 13572–13573.

[127] Kanaras, A. G., Wang, Z. X., Hussain, I., Brust, M., Cosstick, R., and Bates, A. D. Site-specific ligation of DNA-modified gold nanoparticles activated by the restriction enzyme *Sty*I. *Small* **2007**, *3*, 67–70.

[128] Wu, C. S., Wu, C. T., Yang, Y. S., and Ko, F. H. An enzymatic kinetics investigation into the significantly enhanced activity of functionalized gold nanoparticles. *Chem. Commun.* **2008**, 5327–5329.

[129] Blanch, H. W., and Clark, D. S. *Biochemical Engineering*; Marcel Dekker: New York, 1997.

[130] Fersht, A. *Structure and Mechanism in Protein Science: A Guide to Enzyme Catalysis and Protein Folding;* W. H. Freeman & Co.: New York, 1999.

[131] Xiao, Y., Patolsky, F., Katz, E., Hainfeld, J. F., and Willner, I. "Plugging into enzymes": Nanowiring of redox enzymes by a gold nanoparticle. *Science* **2003**, *299*, 1877–1881.

[132] Ruiz-Hitzky, E., Ariga, K., and Lvov, Y. M. *Bio-inorganic Hybrid Nanomaterials—Strategies, Syntheses, Characterization and Applications*, 1st ed.; Wiley-VCH: Weinheim, 2007.

[133] Lin, C. C., Ko, F. H., Chen, C. C., Yang, Y. S., Chang, F. C., and Wu, C. S. Miniaturized metal semiconductor metal photocurrent system for biomolecular sensing *via* chemiluminescence. *Electrophoresis* **2009**, *30*, 3189–3197.

[134] Hill, H. D., Millstone, J. E., Banholzer, M. J., and Mirkin, C. A. The role radius of curvature plays in thiolated oligonucleotide loading on gold nanoparticles. *ACS Nano* **2009**, *3*, 418–424.

[135] Thaxton, C. S., Daniel, W. L., Giljohann, D. A., Thomas, A. D., and Mirkin, C. A. Templated spherical high density lipoprotein nanoparticles. *J. Am. Chem. Soc.* **2009**, *131*, 1384–1385.

[136] Turner, N. A., Needs, E. C., Khan, J. A., and Vulfson, E. N. Analysis of conformational states of *Candida rugosa* lipase in solution: Implications for mechanism of interfacial activation and separation of open and closed forms. *Biotechnol. Bioeng.* **2001**, *72*, 108–118.

[137] Mancheno, J. M., Pernas, M. A., Martinez, M. J., Ochoa, B., Rua, M. L., and Hermoso, J. A. Structural insights into the lipase/esterase behavior in the *Candida rugosa* lipases family: Crystal structure of the lipase 2 isoenzyme at 1.97 Å resolution. *J. Mol. Biol.* **2003**, *332*, 1059–1069.

[138] Le Bas, G. *The Molecular Volumes of Liquid Chemical Compounds*; Longmans, Green: New York, 1915.

[139] Sherwood, T. K., and Pigford, R. L. *Absorption and Extraction*; McGraw-Hill: New York, 1952.